HORMIGÓN Y ACERO
ISSN: 0439-5689

HORMIGÓN y ACERO

Revista cuatrimestral de ACHE ASOCIACIÓN ESPAÑOLA DE INGENIERÍA ESTRUCTURAL

Diciembre 2018 | volumen 69 - Suplemento 1

Diciembre 2018 | volumen 69 - Suplemento 1

www.elsevierciencia.com/hya

Número especial dedicado a Carmen Andrade

Carmen Andrade

HORMIGÓN y ACERO

Diciembre 2018 | volumen 69 – Suplemento 1

REVISTA CUATRIMESTRAL DE LA ASOCIACIÓN ESPAÑOLA DE INGENIERÍA ESTRUCTURAL (ACHE)

ÍNDICES Y SERVICIOS DE INFORMACIÓN: *Hormigón y Acero* está indexada en las bases de datos siguientes: Emerging Sources Citation Index/ Web of Science (ESCI/WoS) – ScienceDirect - ICYT - Dialnet - Sumaris - Urbadoc - Catálogo Latindex - Pascal

ACHE

Etsi Caminos, Canales y Puertos
Avda. Profesor Aranguren, s/n.
Ciudad Universitaria. 28040 Madrid
Tel.: (+34) 91 067 41 64 - www.e-ache.com

ELSEVIER

Avda. Josep Tarradellas, 20-30, 1.º
08029 Barcelona (España)

Zurbano, 76, 4º Izq.
28010 Madrid (España)

ISSN 0439-5689
Publicación cuatrimestral (3 números al año)
www.elsevierciencia.com/hya

Miembro de la Asociación de Prensa Profesional.

Protección de datos: Elsevier España, S.L.U. declara cumplir lo dispuesto por la Ley orgánica 15/1999, de 13 de diciembre, de Protección de Datos de Carácter Personal.

Suscripciones y atención al cliente
Elsevier España, S.L.U. Travesera de Gracia, 17-21, 08021 Barcelona (España)
Teléfono: 902888740
Correo electrónico: suscripciones@elsevier.com

Impresa en España

Esta publicación se imprime en papel no ácido.

This publication is printed in acid-free paper

Depósito legal: B-8709-2014

ACHE
www.e-ache.com

Disponible en
ScienceDirect
www.sciencedirect.com

HORMIGÓN y ACERO
www.elsevierciencia.com/hya

Diciembre 2018 | volumen 69 - Suplemento 1
December 2018 | volume 69 - Supplement 1

SUMARIO | CONTENTS

Revista cuatrimestral de la ASOCIACIÓN ESPAÑOLA DE INGENIERÍA ESTRUCTURAL (ACHE)
E.T.S.I. de Caminos, Canales y Puertos. Laboratorio de Estructuras. Avda. del Profesor Aranguren, s/n. 28040 Madrid.
Tel.: (+34) 91 067 41 64 - www.e-ache.com

MIEMBROS PATROCINADORES DE LA ASOCIACIÓN ESPAÑOLA DE INGENIERÍA ESTRUCTURAL (ACHE)

Según los Estatutos de la Asociación existen dos tipos de miembros, uno para personas jurídicas y otro para personas físicas. De entre los primeros, y por la importancia que tienen para la Asociación por su contribución económica, destacan los miembros Patrocinadores y los Protectores. Hasta la fecha de cierre del presente número de la Revista, figuran inscritos como **Miembros Patrocinadores** los que a continuación se indican, citados por orden alfabético:

ACCIONA INFRAESTRUCTURAS
Avda. de Europa, 18
28108 ALCOBENDAS (MADRID)

ALE HEAVYLIFT IBÉRICA, S.A
P.I. Los Frailes. Ctra Alcalá de Henares a Daganzo,
km 9. P 101-106, 28814 DAGANZO (MADRID)

ARENAS & ASOCIADOS, INGENIERÍA DE DISEÑO, S.L.P.
C/ Marqués de la Ensenada, 11 - 3º
39009 SANTANDER

C/ Jordi Girona 31 - 2º, Edifici Til·lers
08034 - BARCELONA

CALIDAD SIDERÚRGICA
C/ Orense, 58 - 10º
28006 MADRID

CARLOS FERNÁNDEZ CASADO, S.L.
C/ Orense, 10
28020 MADRID

CEDEX (Laboratorio Central)
C/ Alfonso XII, 3
28014 MADRID

CONSEJO GENERAL COLEGIOS ARQUITECTOS TÉCNICOS
Paseo de la Castellana, 155 - 1º
28046 MADRID

CYPE INGENIEROS, S.A.
Avda. Eusebio Sempere, 5 - Bajo
03003 ALICANTE

DRAGADOS, S.A.
Avda. Camino de Santiago, 50
28050 MADRID

EDARTEC CONSULTORES
C/ Manufactura, 4 - Planta 2 - Mod. 3
41297 MAIRENA DE ALJARAFE (SEVILLA)

E.T.S. INGENIEROS DE CAMINOS - DPTO. MECÁNICA
Ciudad Universitaria, s/n
28040 MADRID

EUROCONSULT
Avda. Camino de lo Cortao, 17 - Zona Industrial Sur
28703 SAN SEBASTIÁN DE LOS REYES (MADRID)

FCC CONSTRUCCIÓN, S.A.
Avda. Camino de Santiago 40
28050 MADRID

FLORENTINO REGALADO & ASOCIADOS
C/ Granja de Rocamora, 18
03015 ALICANTE

GRUPO MECÁNICA ESTRUCTURAL S.L
C/ Amílcar González Díaz, 18
38550 ARAFO (SANTA CRUZ DE TENERIFE)

HILTI ESPAÑOLA, S.A.
Avda. Fuente de la Mora, 2 - Edificio I
28050 MADRID

INSTITUTO EDUARDO TORROJA
C/ Serrano Galvache, 4
28033 MADRID

IECA
C/ José Abascal, 53 - 2º
28003 MADRID

OVE ARUP & PARTNERS, S.A.
C/ Alfonso XI, 12
28014 Madrid

PUENTES Y CALZADAS, GRUPO DE EMPRESAS, S.A.
Ctra. de la Estación, s/n
15888 SIGÜEIRO-OROSO (A CORUÑA)

RÚBRICA INGENIERÍA Y ARQUITECTURA, S.L.
Avda. Hermanos Bou, 246
12003 CASTELLÓN

TECNALIA
Parque Tecnológico de Bizkaia - C/ Geldo - Edificio 700
48160 DERIO (VIZCAYA)

MIEMBROS PROTECTORES DE LA ASOCIACIÓN ESPAÑOLA DE INGENIERÍA ESTRUCTURAL (ACHE)

Según los Estatutos de la Asociación existen dos tipos de miembros, uno para personas jurídicas y otro para personas físicas. De entre los primeros, y por la importancia que tienen para la Asociación por su contribución económica, destacan los miembros Patrocinadores y los Protectores. Hasta la fecha de cierre del presente número de la Revista, figuran inscritos como **Miembros Protectores** los que a continuación se indican, citados por orden alfabético:

ACHE
www.e-ache.com

Disponible en
ScienceDirect
www.sciencedirect.com

Hormigón y Acero 2019; 69(S1):1–2

HORMIGÓN y ACERO
www.elsevierciencia.com/hya

Carta del Director

Es para mí un placer presentar este número especial de *Hormigón y Acero* dedicado a Carmen Andrade con ocasión de su setenta cumpleaños. La revista se une así a una tradición común a otras publicaciones científicas, por la cual los autores dedican sus trabajos a una personalidad relevante de su área de conocimiento con ocasión de alguna efeméride profesional o personal. Es el primer número de este tipo, pero tenemos otro, dedicado a Javier Manterola, que está bastante avanzado y se publicará en el 2019. Asimismo, hay una serie de artículos en cartera que formarán un número dedicado a la trayectoria de Julio Martínez Calzón.

Carmen Andrade ha contribuído a la ciencia y tecnología del hormigón como muy pocos investigadores y sigue trabajando, con una actividad desbordante, como Profesora Invitada en el CIMNE. Javier Sánchez, miembro destacado de su grupo de investigación que ha actuado como Editor Asociado en este número —haciendo un excelente trabajo—, resume abajo sus abundantes méritos, entre los que también está la medalla de ACHE. Quiero destacar que Carmen Andrade es conocida y respetada en todo el mundo como una autoridad en los campos de la corrosión del acero de refuerzo y la durabilidad del hormigón. Es también muy destacable su trabajo como formadora de científicos y tecnólogos, así como la ayuda que ha prestado a muchos otros a tener presencia en las comunidades científicas internacionales.

Todos los artículos de este número se han solicitado ex profeso para contribuir al homenaje a Carmen Andrade. No son sobre ella ni sobre su trabajo, sino que están dedicados a ella. Contamos con la firma de autores tan destacados como Zdeněk P. Bažant, Hans Reinhardt, Giuseppe Mancini, Andrés Torres Acosta, Pedro Castro Borges, Miguel A. Climent, Pedro Garcés o Eugenio Oñate, lo cual es otra muestra del enorme impacto de la trayectoria de nuestra homenajeada. A todos ellos les agradezco su artículo, ya que nos ayudan a honrar a Carmen Andrade y, al mismo tiempo, ayudan a que *Hormigón y Acero* se lea en todo el mundo. Espero que ello contribuya a atraer citas y a que otros autores puedan considerar la revista como posible vehículo para publicar sus trabajos.

Este número especial se presentará públicamente en la Sala Verde de la Escuela de Caminos de la UPM el próximo jueves 14 de marzo a las 16:30 h. Desde aquí invito a los autores y lectores de *Hormigón y Acero* a que hagan un hueco en sus agendas y asistan al acto.

Gonzalo Ruiz
Director de Hormigón y Acero
Correo electrónico: Gonzalo.Ruiz@uclm.es

Carta del Editor Asociado

Carmen Andrade Perdrix ha realizado su carrera investigadora en el Instituto de Ciencias de la Construcción Eduardo Torroja (IETcc-CSIC) al que se incorporó como Científica Titular en 1979, fue directora del mismo en los periodos 1985-1988 y 1993-2000, siendo Profesora de Investigación desde 1987. Actualmente es Profesora Invitada en el *Centre Internacional de Mètodes Numèrics a l'Enginyeria* (CIMNE-UPC), desde marzo 2017.

A nivel internacional ha sido presidenta de diversos organismos internacionales, como UEAtc, RILEM, WFTAO. Desde 2006 a 2008 fue Directora General de Política Tecnológica del Ministerio de Educación y Ciencia y, posteriormente hasta 2012, asesora del Secretario de Estado de Universidades y del Secretario de Estado de Investigación.

Ha recibido varios premios nacionales e internacionales, entre los que destaca el R. N. Whitney Prize 2013 de la NACE, "*Fellow*" de la RILEM y "Miembro Honoraria" de LAT-RILEM en 2014. Es Doctora *Honoris Causa* por la Universidad de Trondheim y por la Universidad de Alicante.

Ha dedicado toda su vida profesional al estudio de la durabilidad de las estructuras de hormigón armado con un prolífico trabajo: autora de más de 220 artículos SCI, 107 capítulos de libros, más de 600 comunicaciones en congresos y tiene concedidas varias patentes nacionales e internacionales. Ha dirigido 28 tesis doctorales y ha sido la responsable o participado en diversos Comités de Normativa de AENOR, CEN, JCSS o RILEM.

Carmen Andrade siempre ha trasmitido a su Grupo de Investigación la filosofía de Eduardo Torroja que se resume de forma

https://doi.org/10.1016/j.hya.2018.12.001

muy plástica en la frase *technicae plures opera unica*, siendo consciente de la necesidad de un enfoque multidisciplinar para poder avanzar en el conocimiento de las estructuras y los procesos que tienen lugar en ellas. Así desde un primer momento, puso de manifiesto la necesidad de establecer colaboraciones tanto en el ámbito nacional como internacional, escuchando y abordando los problemas del sector de la construcción, a la vez que llevaba a cabo avances en la investigación básica.

Como Editor Asociado en este número especial de la revista *Hormigón y Acero* en honor a Carmen Andrade, quería agradecer a todos los autores que han participado en el mismo su predisposición y el nivel científico-técnico de las publicaciones presentadas, que hacen que sea el mejor homenaje posible. La variedad de temas que aparecen en este número es reflejo de los campos en los que ha trabajado Carmen Andrade, desde el estudio de degradación árido-álcali, propiedades mecánicas, simulación multifísica, extracción de cloruros, protección catódica o el uso de nuevos materiales, como el acero inoxidable.

Javier Sánchez
Editor Asociado
Correo electrónico: javier.sanchez@csic.es

Available online at
ScienceDirect
www.sciencedirect.com
Hormigón y Acero 2019; 69(S1):3–14
www.e-ache.com
www.elsevierciencia.com/hya

Importance of creep and ASR gel diffusion in predicting ASR induced expansion☆

Importancia de la deformación por fluencia lenta y la difusión en gel de la reacción de álcali-sílice (RAS) en la predicción de la expansión provocada por la RAS

Saeed Rahimi-Aghdam[a], Zdeněk P. Bažant[b,*]

[a] *Ph.D. candidate, Department of Civil and Environmental Engineering, Northwestern University, 2145 Sheridan Road, CEE/A135, Evanston, IL 60208, USA*
[b] *Distinguished McCormick Institute Professor and W.P. Murphy Professor, Departments of Civil, Mechanical and Materials Science Engineering, Northwestern University, 2145 Sheridan Road, CEE/A135, Evanston, IL 60208, USA*

Received 27 November 2017; accepted 23 May 2018
Available online 30 July 2018

Abstract

The paper reviews development of a diffusion-based and creep-based model for calculating the evolution of expansion and damage induced by alkali-silica reaction (ASR). First, the model of Bažant and Steffens (2000) is adopted to calculate the rate of production of the ASR gel within the aggregate. Next, a non-linear diffusion according to Rahimi-Aghdam and Bažant (2017) is presented to model the penetration of ASR gel into the micropores, nanopores and microcracks. The gel diffusion into pores of the aggregate causes expansion and damage to the surrounding concrete, and is found to be an important modeling aspect. The damage is assessed by microplane model M7, into which the creep is incorporated. The creep is found to have a significant influence on the long-term evolution of ASR-induced damage. The predictions are in good agreements with the laboratory experiments and the model appears to be ready to predict the ASR effects in real structures.

Keywords: Alkali-silica reaction; Swelling; Damage; Microplane model; Finite element

Resumen

El artículo analiza el desarrollo de un modelo basado en la difusión y en la deformación por fluencia lenta para calcular la evolución de la expansión y el daño provocado por la reacción de álcali-sílice (RAS). Primero, se adopta el modelo de Bažant y Steffens (2000) para calcular la tasa de producción de gel para la RAS dentro del conglomerado. A continuación, se presenta una difusión no lineal según Rahimi-Aghdam y Bažant (2017) para modelar la penetración del gel para la RAS en los microporos, nanoporos y microfisuras. La difusión del gel en los poros del conglomerado provoca expansión y daño al hormigón cercano, y se encuentra que es un aspecto importante de modelado. El daño se valora mediante el modelo de microplanos M7, al cual se incorpora la deformación por fluencia lenta. Se cree que esta tiene una influencia considerable sobre la evolución a largo plazo del daño provocado por la RAS. Las predicciones son coherentes con los ensayos de laboratorio y parece que el modelo está preparado para predecir los efectos de la RAS en estructuras reales.

Palabras clave: Reacción de álcali-sílice; Hinchamiento; Daño; Modelo de microplanos; Elemento finito

☆ Written in honor of Dr. Carmen Andrade, retiring Director of CSIC, Toroja Institute, and Past President, RILEM.

* Corresponding author.
E-mail address: z-bazant@northwestern.edu (Z.P. Bažant).

https://doi.org/10.1016/j.hya.2018.05.006

1. Introduction

The alkali-silica reaction (ASR; aka alkali-aggregate reaction, AAR) attacks mineral aggregates in concrete when they contain imperfectly crystalline silica. The reaction produces a gel that can imbibe enormous amount of water and cause swelling. The induced swelling, progressing for many months, years or even decades, often causes significant strength degradation and damage in concrete structures. Because drying diminishes the rate of ASR, the worst damage usually occurs in massive structures such as large bridges and dams, and nuclear power plant structures in which the cross-section core remains undried for years, even decades. As a result, preventing the ASR-induced damage is one important goal of sustainable design.

The ASR-induced damage was first identified by Stanton in 1942 [1]. Since that time many researchers have worked on this problem and a vast body of literature has been gathered. A comprehensive literature review has recently been published by Saouma and Xi [2,3].

Although several models have been proposed to predict the ASR-induced damage, they consider a simplistic constitutive law for concrete. An exception is a recent model Alnaggar and Cusatis [4] which uses Cusatis' lattice discrete particle model, and in the particle contacts an excellent material model for concrete. However, all these models do not consider the diffusion of ASR gel into pores and cracks, and all except Alnaggar and Cusatis' neglect the effect of creep. Both phenomena significantly mitigate the ASR-induced damage.

The current models, except [4], assume that the only phenomenon that controls the rate of ASR-induced swelling is the production of ASR gel and its water imbibition. In modeling the diminishing rate and stoppage of ASR-induced swelling, which happen after a few months in accelerated tests, these models consider the ASR gel to reach the maximum capacity of water imbibition relatively fast and water imbibition to stop after that. This assumption contradicts the experimental results showing that the ASR gel can imbibe a vast amount of water, even 100-times its initial volume. The only reasonable justification for the diminishing and stoppage of ASR-induced swelling is the diffusion of ASR gel into the surrounding pores, and also into the microcracks produced by the diffusion in the aggregate pieces and surrounding cement mortar. After significant damage the diffusion rate exceeds the rate of water supply which causes the swelling to slow down and eventually to stop.

This study reviews the recent development of a comprehensive model for ASR [7,31] and provides some improved explanations and justifications of its main features, which include:

1. The delay in ASR due to production of ASR gel and its diffusion into the pores and expanding cracks.
2. Fracturing of the solid framework of concrete as a two-phase medium, caused by diffusion of the ASR into pores and cracks in the aggregates and surrounding mortar.
3. The differences in cracking patterns of the damage induced by the ASR under different confinement conditions, applied stress states and boundary conditions.
4. The effect of creep on mitigating the ASR damage.
5. The effect of alkali content on the ASR-induced damage and swelling.
6. The effect of temperature on ASR-induced damage and swelling.

Analysis of these effects must be coupled with a realistic model for ASR gel production within the reactive aggregate pieces. Such a model was developed by Bažant and Steffens [8] and was also used and improved by Alnaggar and Cusatis [4]. Here this model is coupled with the analysis of the aforementioned phenomena.

Analysis of the ASR gel diffusion is an essential aspect of prediction. A nonlinear diffusion model has been developed and calibrated for this purpose. To predict the ASR-induced damage in larger structures, a macroscopic continuum model, endowed with a localization limiter preventing spurious instability of softening damage, is necessary. The microplane constitutive damage model [5,6] is most realistic for this purpose. It can distinguish different damage patterns under various stress states. Its latest version, M7, is adopted. Since creep of the solid framework significantly mitigates the ASR damage, a concrete creep model is incorporated into M7.

2. Review of simplified model of kinetics of ASR gel production

First, we need to introduce a model for the kinetics of gel production in mineral aggregates. To this end, the simplified model of Bažant and Steffens [7], as improved by Bažant and Rahimi-Aghdam [8,9] and used, in improved form, by Alnaggar and Cusatis [4], is adopted.

Since the shape of aggregate grains is not too important, spherical grains of diameter D are considered (Fig. 1a). The ASR reaction occurs at various randomly located discrete sources inside the grain. Those near the grain surface will be activated first and the time to activate the deeper sources will grow with the depth, z. Thus, as an average behavior of many aggregate grains, we introduce a smeared continuum model in which water diffuses radially into a spherical aggregate grain [8], with a spherical front of radius z at which the ASR reaction takes place. The ASR reaction is assumed to occur instantly at the front of water penetration (Fig. 1a). The reaction is slowed down by the diffusion of water through the aggregate piece, and particularly through the layer of ASR gel already formed.

The coupling with the penetration of ASR gel into the pores of the mortar surrounding the aggregate piece is assumed to be one-way, i.e., the evolution of gel mass $w(t)$ is considered to be independent of pressure $p(t)$ developed in the pores surrounding the aggregate piece. This is, of course, a simplification, although probably not a major one since the pore pressures sustainable by concrete cannot be large enough to slow down the alkali-silica reaction appreciably.

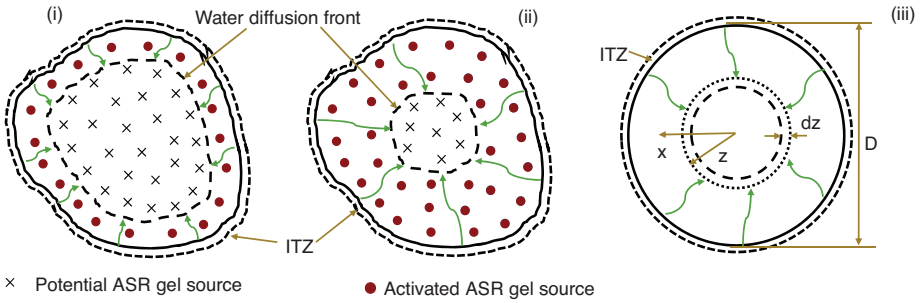

a ASR gel formation due to water diffusion into reactive aggregate: (i) early stage of diffusion; (ii) late stage of diffusion; (iii) idealization with spherical diffusion

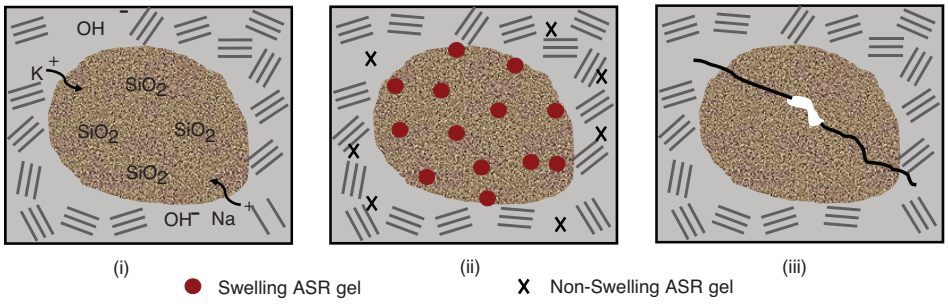

b ASR reaction process and schematic illustration of ASR induced damage: (i) alkali-silica reaction; (ii) formation of swelling and non-swelling ASR gel; (iii) ASR-induced damage and cracking

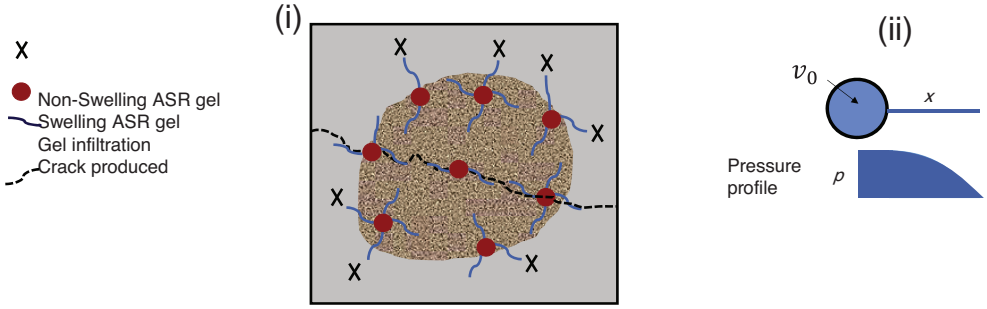

c ASR gel transport: (a) ASR gel infiltration and produced global damage; (b) one ideal gel infiltration path

Figure 1. Formation of the ASR gel and its diffusion.

In this study, the same set of equations as Bažant and Rahimi-Aghdam (2017) is used to calculate $w(t)$ and the mass of imbibed water, $w_i(t)$. It should be noted that we assume the ASR gel to imbibe water for years, and even decades. The main reason for the deceleration of the ASR-induced swelling is the diffusion of ASR gel into the cracks produced by ASR (and, often, diminishing of water supply). Several other studies assumed the ASR gel to imbibe only an assumed limited amount of water for only an assumed limited time, considering these phenomena to diminish and stop according to a chosen schedule. This simplification disagrees with the experimental results, which show ASR gel can imbibe an almost unlimited amount without any particular time limitation. These oversimplifications were necessary because the diffusion of ASR gel into the pores was not considered.

3. Diffusion of ASR Gel into surrounding pores

The penetration of gel from a gel source into adjacent pores and cracks is another mechanism which controls the rate of ASR and prolongs the process enormously (Fig. 1c). This process can be formulated as a diffusion process obeying the Darcy law. The flow velocity is $\dot{z} = d_D \nabla p$ where ∇ denotes the gradient and b_D is the Darcy permeability (dimension $m^3 s/kg$). In detailed analysis, one could consider a differential equation for the diffusion in radial direction z, embedded in

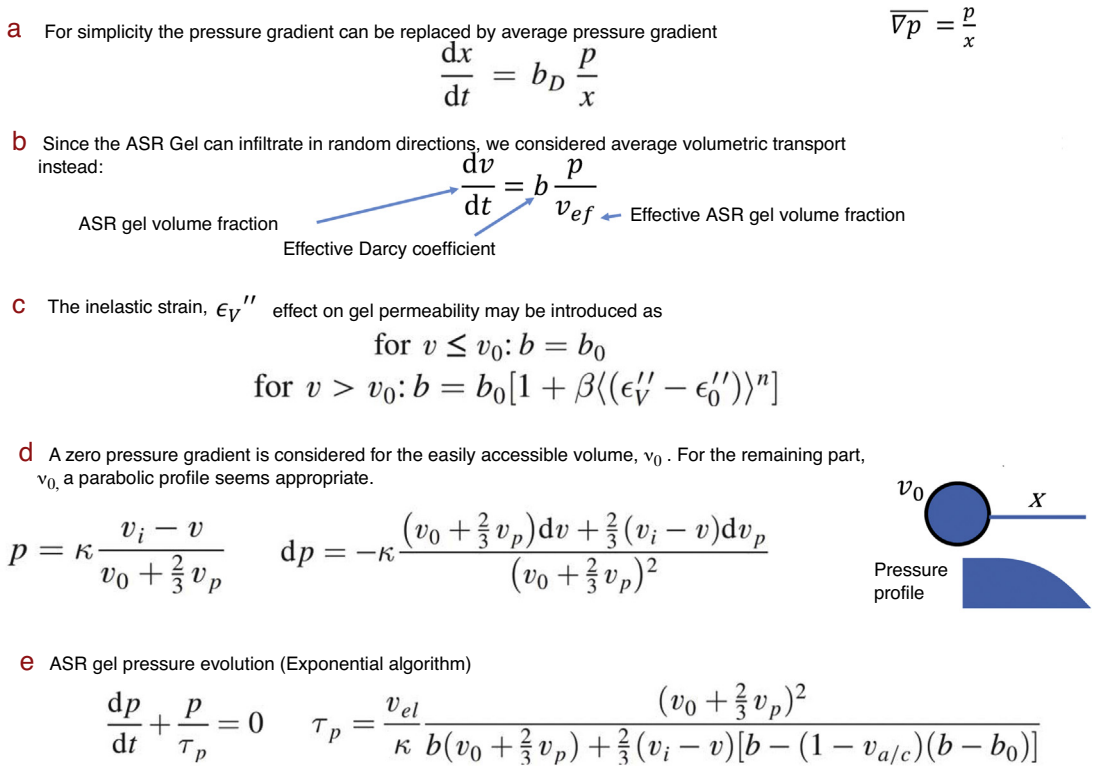

Figure 2. Calculating the diffusion of ASR gel and Induced pressure inside pores.

a continuum point. However, considering all the uncertainties and simplifications, it appears sufficient to replace the flow velocity, $\dot{z}$, with the velocity of the diffusion front, dx/dt, and the pressure gradient with the average pressure gradient $\nabla p = p/x$. Using these reasonable simplifications, we can write the simplified Darcy diffusion equation as given in Fig. 2a.

The ASR gel first penetrates at near-zero pressure p into the empty and easily accessible pores of volume fraction v_o. The easily accessible pores are of three kinds: (1) pores inside the aggregate, the distribution and size of which depends strongly on the type of aggregate; (2) the cement paste pores (since the hardened cement paste always contains empty pores, due to self-desiccation); and (3) the bigger pores in the interface transition zone (ITZ) surrounding the aggregate, more easily fillable due to a lower mass density and higher porosity in that zone.

Note that, in real structures, the filling of empty pores of volume fraction v_o can take many years and decades. This is the reason for the great delay in the initiation of the ASR-induced expansion. Only after the empty pores get filled, further imbibition of water can produce a significant pressure in the gel, produce cracks and penetrate them (Fig. 1b and c).

We assume that one or several basic gel sources form in each reactive aggregate (when it contains reactive silica). From each gel source, the gel diffuses in multiple random directions (Fig. 1a and c) into nearby pores, microcracks and ITZ. Note that the gel that penetrates into cement paste (farther from the aggregate) will calcify and thus no longer imbibe water and swell, thus becoming harmless. The direction of ASR gel diffusion is random and the distances from the different gel sources to the fronts of diffusion paths also vary randomly (Fig. 1c). Therefore, on the continuum scale, it is reasonable to consider a volumetric average diffusion instead of a directional diffusion. The volumetric diffusion equation can be written as shown Fig. 2b, where p is the average gel pressure; b is an effective Darcy permeability (dimension m^2/Ns or ms/kg), which is proportional to the actual Darcy permeability, b_D; and v_{ef} is an effective volume fraction.

It is clear that permeability must increase due to cracking. If we denote the crack opening as δ and use the crack band model as a localization limiter [10,11], then we have $\delta_c \approx l_o \in''$, where l_o is a material characteristic length, and $\in''$ is the inelastic part of average tensile strain across the crack band.

Since the induced cracks can run randomly in any direction, expansion in all directions is expected, i.e., the inelastic strain must be volumetric, $\in_v''$ considered to be a function of the principal inelastic strains. Among them, the increase of permeability can be caused only by those tensile strains that exceed a certain empirical finite threshold, $\in_0''$ (which is here assumed to be 0.001%). Thus, the effect of inelastic strain (damage) on gel permeability may be introduced as seen Fig. 2c.

4. Evolution of ASR gel pressure at constant total gel mass

During the filling of empty, easily accessible, pores, of volume fraction v_o, the pressure is approximately zero. After these pores get filled completely, the pressure in the pores starts to develop. For simplicity, we assume the radial pressure profiles to be similar as the penetration depth grows. The type of profile makes little difference for the results. We assume a uniform

pressure p up to volume v_0. Beyond that, a parabolic pressure drop (as sketched in Fig. 2d) is most realistic.

Now that we have assumed the self-similar profile in the pores, we can use an explicit computational algorithm to calculate the pressure evolution. However, very short time steps would be needed to ensure numerical stability and convergence. This limitation becomes a serious problem in simulating long-term ASR. The same problem was faced in modeling long-term creep of concrete structures. The creep proceeds rapidly at first, which needs time steps in the order of seconds at the beginning. But to run calculations up to, e.g., 50 years, the time steps for creep integration need to be extended to months in duration. The same increase in the time step must possible here since, after several years, the pressure evolution becomes very slow.

Therefore, an analog of the unconditionally stable exponential algorithm for creep [12,13] has been developed for gel diffusion. Similar to piece-wise strain constancy in the unconditionally stable exponential algorithm for creep [12,13], we assume the mass of gel to be held constant during each time step Δt and allow the pressure to relax due to diffusion. At the end of each time step, the pressure and gel mass are corrected by an abrupt change. Fig. 2e describes the relaxation of pressure at the constant gel mass, with t_p playing the role of characteristic time. It should be noted that the pressure relaxation equation is nonlinear since t_p depends on variables such as volume fractions and permeability, which themselves depend on pressure. However, since these variables do not change significantly during the time step, t_p may be considered as a constant during each time step and calculated using the values from previous time step. This allows the pressure relaxation equation to be integrated by separation of variables.

5. Constitutive law for the solid part of concrete and incorporation of creep

Generally in structures undergoing ASR, the concrete experiences complex multiaxial stress states. Thus, anisotropic damage should be expected. The anisotropic damage of concrete can be described effectively by the microplane constitutive model M7 [5,6]. The basic idea of microplane model is to formulate the constitutive law in terms of the vectors of stress and strain acting on a generic plane of any orientation in the material microstructure, called microplane. The use of vectors, instead of tensors, is similar to the Taylor models, used for plasticity of polycrystalline metals, but there are major differences; especially, the static constraint instead of a kinematic one is considered. In this study, the latest version of microplane model, M7, is used. Model M7 has been demonstrated to give rather good predictions of the behavior of quasibrittle materials over a broad range of loading conditions.

The ASR-induced damage in structures evolves over years, even many decades. Therefore, creep and shrinkage play a major role. Creep and shrinkage can even have a significant effect on relatively short laboratory experiments. To determine the creep and shrinkage in undamaged concrete, RILEM model B4 [14] is used in this study. However, the ASR damage in the presence of external loads causes fracturing. Thus, the creep and shrinkage cannot be calculated simply using a plain creep model, such as B4. It needs to be calculated using a combination of the creep model with the microplane model M7.

In undamaged material between the expanding pores and cracks, the creep is aging viscoelastic and linear in stress, while the fracturing damage leading to cracks depends on stress nonlinearly. As a result, the creep strain can be considered to be additive to fracturing strain. Since the ASR-induced pressure and damage evolve in time and influence the constitutive law, the rate-type creep model [15] must be used, rather than hereditary integral-type. The rate type creep model can be structured according to the Kelvin or Maxwell chain. The former is more convenient since model B4 specifies the compliance, rather than relaxation, function (Fig. 3a).

The spring and dashpots moduli of the Kelvin units in the chain can be obtained by discretizing the continuous retardation spectrum [16]. Due to aging, the spectrum is significantly different for every time step and every integration point. The retardation times are selected to make a geometric progression with quotient 10 and must cover the whole time range of interest (Fig. 3a). Time integration allowing an arbitrary increase of the time steps as creep slows down needs to use the exponential algorithm [12], which is unconditionally stable. On the tensorial level, the exponential algorithm leads to the incremental stress-strain relation as shown in Fig. 3b, in which, $\in_{ij}^{cr}$ is the creep strain increment tensor that is calculated from Bazant's exponential algorithm for Kelvin chain model; $\bar{E}$ is the incremental modulus which is obtained from the exponential algorithm; ε^{sh} is the shrinkage strain increment, and $\alpha\Delta T$ is the thermal strain. To combine M7 with creep, all the stress predictions in the microplane model are written in a form analogous to the equation in Fig. 3b.

It should be mentioned that in this study, for simplicity, model B4, which gives average creep for cross section, is used. However, due to damage and non-uniformity of stress it is beneficial to use pointwise creep laws such as XMPS model [17].

6. Two-phase medium for loading of concrete by pressure in pores and cracks

It is standard to model saturated porous solids with fluid in their pores using Biot two-phase medium. For Biot medium, the volumetric equilibrium relation reads $S_v = \sigma_v - \alpha p$, in which S_v is the volumetric stress in the solid phase (dry material).); σ_v is the total volumetric stress in the two-phase medium (solid and fluid), which is used in finite element analysis to determine the nodal forces; and α = Biot coefficient which it related to porosity, but is usually approximated such that $1 - \alpha$ would represent the ratio between the bulk moduli of solid with and without pore fluid [18]. However, concrete is not a standard porous solid and the formulation of Biot medium is not completely applicable for concrete. The main reasons for the inapplicability of Biot relations to concrete are: (1) Concrete in never fully saturated, due to self-desiccation and drying (and the existence of anticlastic capillary menisci), which is why its pores are filled with both vapor and liquid (and adsorbed water); (2) unlike normal saturated two-phase media such as soils, considerable amount

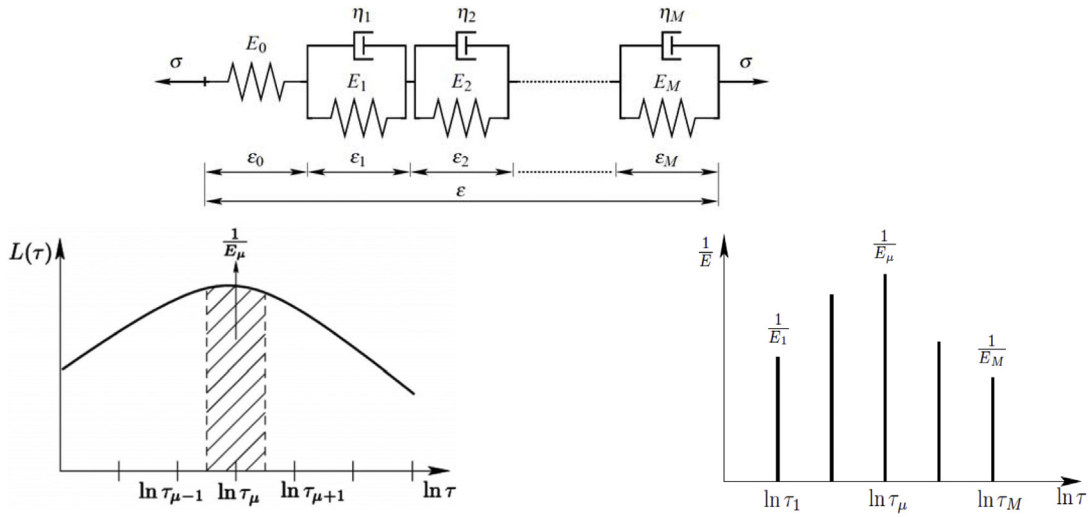

a) Aging creep: (a) Kelvin chain; (b) continuous retardation spectrum; (c) discrete retardation spectrum

b) On the tensorial level, exponential algorithm (Bažant 1971) leads to the incremental stress-strain relation

$$\Delta\sigma_{ij} = \bar{E}(\Delta\epsilon_{ij} - \Delta\epsilon''_{ij}) \qquad \Delta\epsilon''_{ij} = \Delta\epsilon^{cr}_{ij} + \delta_{ij}(\Delta\epsilon^{sh} + \alpha\Delta T)$$

Effective young modulus from exponential algorithm

Creep strain

Shrinkage strain

Temperature strain

c) Two- Phase Medium for loading of concrete by pressure in pores and cracks

$$\begin{cases} \Delta S_V = \Delta((1-\phi)\sigma_V) - \Delta(\phi p) \\ \Delta S_{ij} = \Delta\sigma_{ij} - \delta_{ij}\,\Delta(\phi p) \\ \Delta(\phi p) = \phi\,\Delta p + p\,\Delta\phi \end{cases}$$

S_{ij} : Total stress in the two phase medium
σ_{ij} : stress in solid phase
S_V : Volumetric stress in the two phase medium
σ_V : Volumetric stress in solid phase
ϕ : Effective porosity

d) Considering aggregate size (small and big), mass of imbibed water,wi

$$w_i = w_s w_i(D_s) + w_b w_i(D_b), \qquad w_s + w_b = 1$$

Weights

D_s and D_b= size of small and big aggregate size.
$w_i(D_s)$ and $w_i(D_b)$ ≡ masses of imbibed water for aggregate sizes D_s and D_b

Figure 3. Incorporation of creep and two-phase medium.

of evaporable water is contained in the nanopores (only a few atoms wide). This water behaves partly as a load-bearing solid.

Therefore, the Biot medium relations need to be adapted for concrete. Bažant and Rahimi-Aghdam (2017) modified Biot relations by using effective porosity ϕ instead of Biot coefficient. The same modification is used here. Using effective porosity ϕ instead of Biot coefficient α, the incremental volumetric and tensorial two-phase equilibrium relations can be written as Fig. 3c.

7. Modeling ASR for various aggregate sizes

For simplicity, all the preceding equations in this study are formulated for one equivalent aggregate size. But in reality, the sizes of reactive aggregates are distributed statistically over a broad range.

The kinetics of reaction depends strongly on the aggregate size and small aggregates react much faster than big ones. Therefore, considering one effective aggregate size cannot capture the fast expansion occurring in the small aggregates, and the predicted expansion curves always show an initial delay. In detailed calculations, one should consider the real distribution of aggregate size, but this is computationally complicated and usually the exact distribution of aggregates sizes in not available. A simple way to avoid the unrealistic initial delay is to consider two different aggregate sizes, with different computational weights w_s and w_b for small and big aggregate sizes, D_s and D_b. Thus,

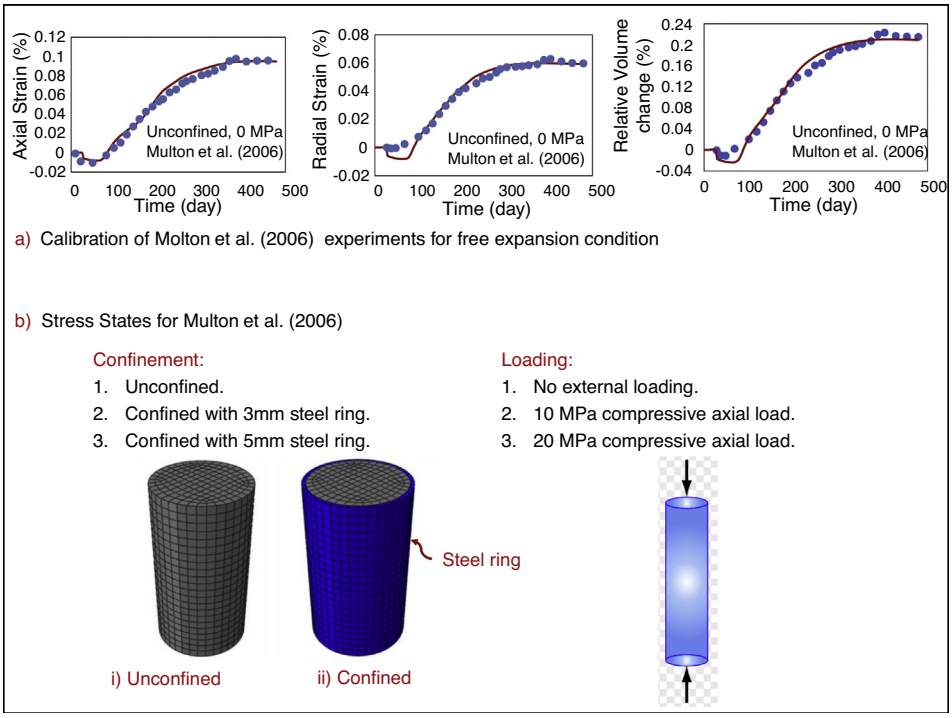

Figure 4. Calibration of Multon et al. experiment and stress states.

the total mass of imbibed water w_i is calculated as shown in Fig. 3d.

8. Effect of various stress states on ASR-induced expansion

Several numerical and experimental studies showed a significant effect of applied stress state and confinement on ASR-induced expansion and damage [4,19–22]. Particularly, experiments showed that the effect of loading on the ASR-induced volume expansion is minimal and usually the applied stress changes only the direction of expansion. For instance, large compressive stress in one direction transfers the expansion to other directions with smaller or no compression. To analyze the ability of the proposed model to predict the ASR-induced expansion and deterioration at different stress states, we consider some published experimental data. First we analyze the accelerated laboratory tests of Multon and Toutlemonde (2006). The duration of these tests was 450 days and the accelerated ASR-induced expansion was comparable to that obtained during 5 to 50 years in actual structures (in which the reaction is not accelerated). In these tests, concrete cylinders of diameter 130 mm and height of 120 mm, with the water-cement ratio of 0.45, was used. To accelerate the rate of ASR, potassium hydroxide was dissolved in the mixing water to increase Na_2O_{eq} to 1.25% of the mass of cement.

The model was first calibrated for the case of free expansion. Two aggregate sizes were considered: $D = 9$ mm for 85% of aggregates, and $D = 4.2$ mm for 15%. Fig. 4a shows the calibrated results for the free expansion case. As the figure shows, considering two aggregate size is enough, and the predicted initial expansion has no delay.

Multon and Toutlemonde (2006) analyzed the effect of various stress states on the ASR-induced expansion. Fig. 4b shows the confinement used and the loading conditions. In total, they tested specimens at nine different stress states. Here we use one of them (the free expansion) to calibrate our model and then analyze the calibrated model ability to predict ASR-induced swelling in other stress states. Fig. 5a shows the plot of predicted vs. experimental results for the axial deformations and Fig. 5b shows the same for the radial deformations. These figures demonstrate that the model is able to predict the ASR-induced expansion in good agreement with the experimental results. In particular, they confirm that the present model can predict the so-called 'expansion transfer', i.e., the load-induced transfer of ASR expansion to another direction.

It should be noted that in the cylinders confined by tubular steel envelopes, the concrete was considered to slide against the steel. For sure this slide was not frictionless and the friction could be significant. However, the friction coefficient was not reported. In simulations, it was assumed to be 0.15.

As a consequence of the loading and confinement conditions, the damage and cracking pattern are also different for various stress states. Fig. 6a shows the predicted cracking pattern for Multon and Toutlemonde (2006) experiments. For the unconfined load-free case, the cracks can propagate randomly in all directions, but as it can be seen, for radial confinement the cracks are mostly radial. Adding a sufficient axial compressive load will prevent the damage bands, or macrocracks, in the loading direction.

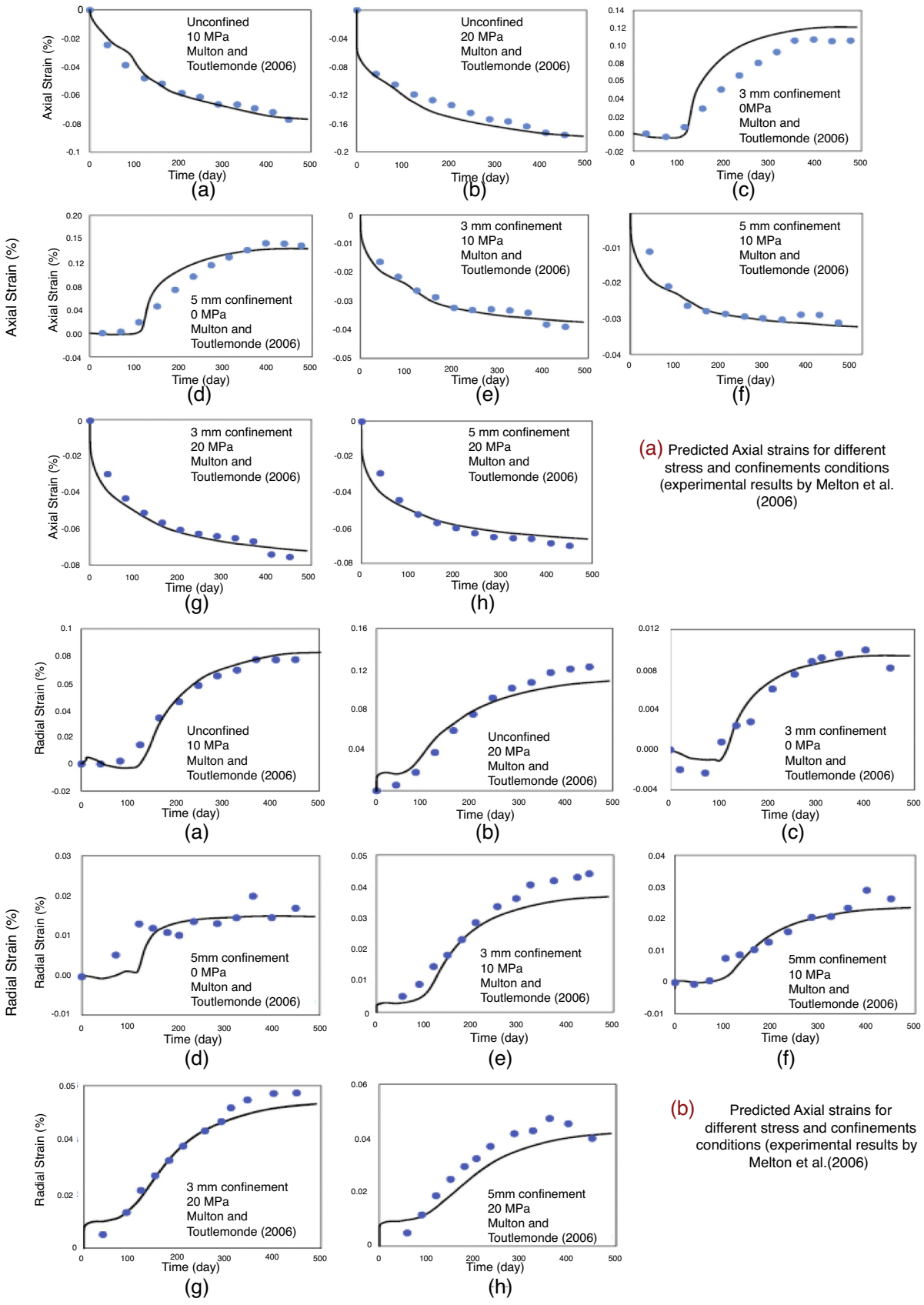

(a) Predicted Axial strains for different stress and confinements conditions (experimental results by Melton et al. (2006)

(b) Predicted Axial strains for different stress and confinements conditions (experimental results by Melton et al.(2006)

Figure 5. Predicted vs. experimnetal results for Multon et al. (2006) experiments.

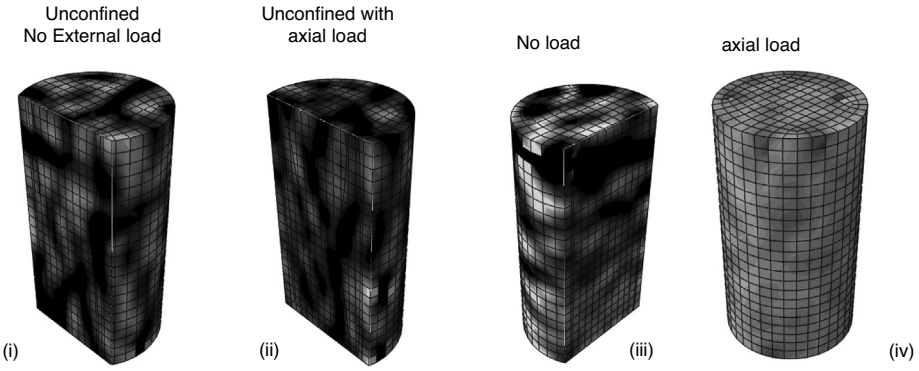

a) Cracking patterns for different stress states: (i) unconfined-unloaded; (ii) radial confined-unloaded; (iii) unconfined axially loaded; (iv) confined axially loaded

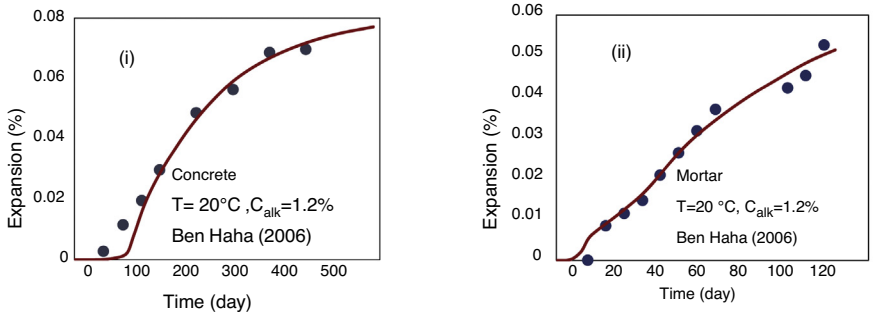

b)

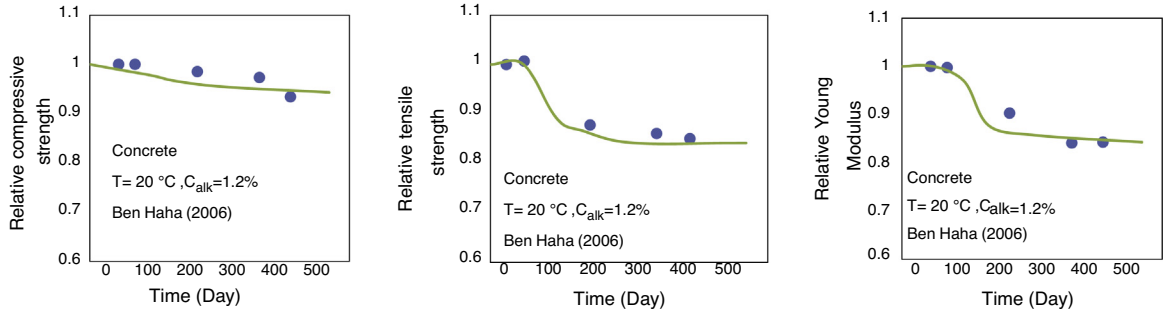

c) Mechanical properties change due to ASR reaction: (a) compressive strength of affected concrete versus unaffected one; (b) tensile strength of affected concrete versus unaffecte done; (c) Young's modulus of affected concrete versus unaffected one

Figure 6. Cracking pattern for ASR-induced damage at different stress states and the degradation of mechanical properties due to ASR-induced damage.

9. The effect of ASR on mechanical properties

As many studies showed, the ASR-induced expansion generates microcracks and cracks that weaken the concrete [23–32]. Here we analyze the influence of ASR on: (1) the compressive strength; (2) the tensile strength; and (3) Young's modulus.

The model predictions are compared with the experimental data of Ben Haha [25,26]. His experiments include accelerated tests of concrete prisms of dimensions 70 × 70 × 280 mm, submerged in water. Since no measurements are reported for autogenous shrinkage and swelling, their effects are neglected, although they might have had considerable effects on the deformations.

First, we calibrate the model to fit Ben Haha's measured ASR-induced expansion. We consider 85% of aggregates to have the size of $D = 10$ mm, and 15% $D = 4.3$ mm. Fig. 6b compares the experimental and calculated ASR induced expansions. Now that the model is calibrated to predict the measured expansion, we can test its power in predicting the effect of ASR on the mechanical properties. In this study, we analyze the effects of an axial load, tensile or compressive, at different stages of the ASR.

Let us begin with the compressive strength. To determine the ASR effect on the compressive strength, a compressive axial

force, increased to reach the strength limit, is applied to the specimen at different reaction times. Although it seems rational that the compressive strength declines due to ASR, because it generates micro- and macro-cracking, there is a disagreement among various experimenters. For instance, Clark and Ono [27,29] found that ASR can decrease the compressive strength significantly (up to 40%), while Monette [28] did not see any significant change. However, in this regard it should be noted that the ASR and the aging due to cement hydration have opposite effects, the former decreasing the strength and the latter increasing it. Another source of increase in compressive strength may be the extra C–S–H that is produced outside the aggregate when the ASR gel gets calcified. These competing effects must be the main reason for this discrepancy.

To isolate the effect of ASR, we consider the relative compressive strengths of specimens with and without the reactive aggregates. For calculating the aging due to hydration, the model by Rahimi-Aghdam et al. [33] is used. Fig. 6c shows the compressive strength ratio for concretes affected or unaffected by ASR, at various reaction times, and shows that the compressive strength decreases by about 5% due to ASR, which is in agreement with the experimental results.

The same procedure is used to determine the effect of ASR on the tensile strength and Young's modulus. As Fig. 6c shows

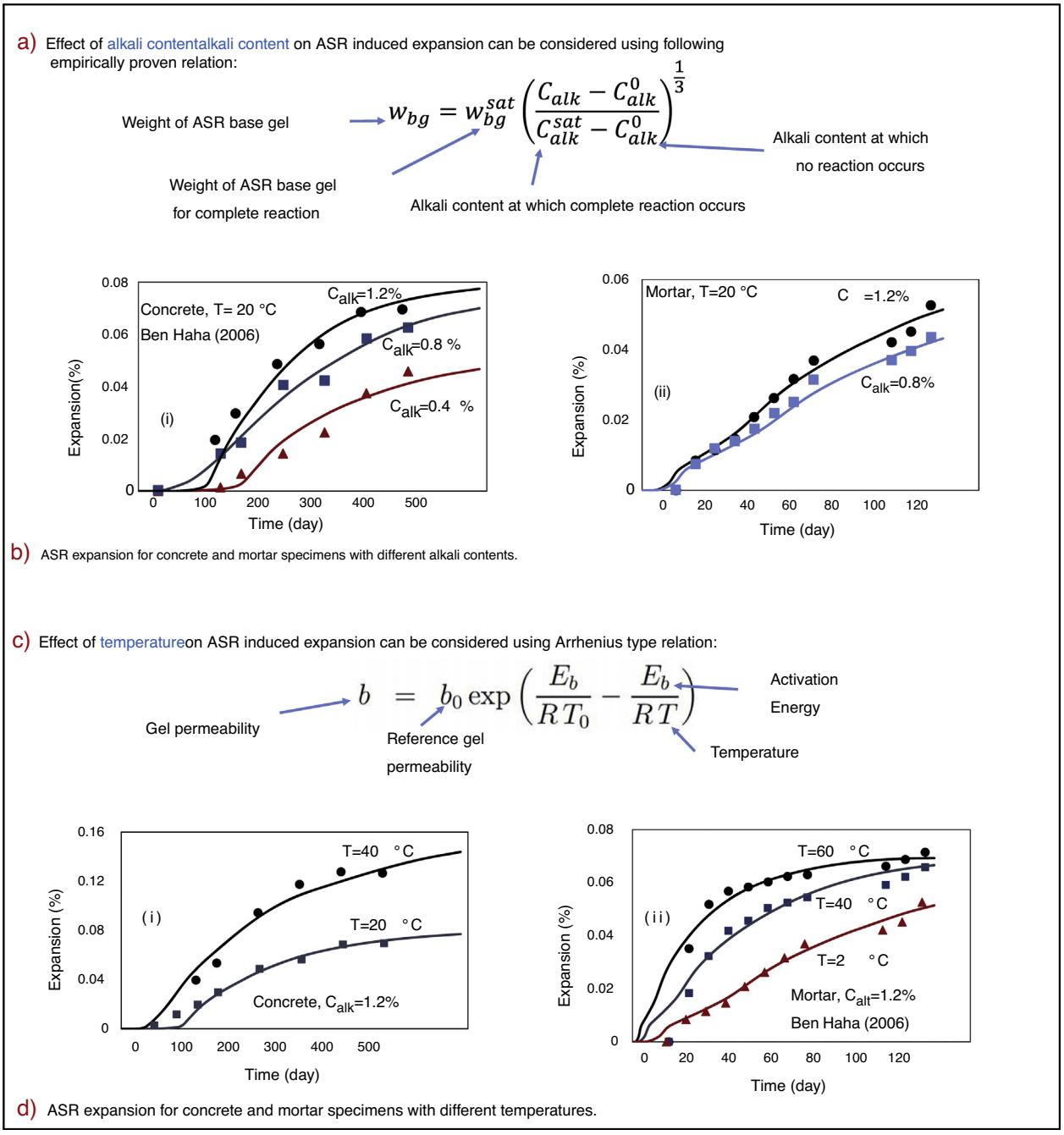

Figure 7. Effect of alkali content and temperature on ASR-induced expansion.

that the effects of ASR on the tensile strength and on Young's modulus are more pronounced. The model is able to predict these effects well. The ASR expansion is here found to decrease the tensile strength and Young's modulus by nearly 15%.

10. Effect of alkali content on ASR induced-expansion

The alkali content can have a considerable influence on the ASR reaction [34,35]. The availability of alkali ions and hydroxyl ions is what controls the ASR kinetics. Often, we should assess the ASR for the concrete in which reactive silica content is insufficient to complete the ASR reaction. To model this, we must relate the amount of the ASR gel produced to the alkali content. Fig. 7a shows the empirical relation that is considered in this study, in which C_{alk} is the alkali content (ratio of the mass of alkali to cement mass), C^0_{alk} is the alkali content at which ASR stops or does not begin, and C^*_{alk} is the alkali content at which alkali ions are adequate for complete reaction. In this study, we assume $C^*_{alk} = 0.1\%$, and C^*_{alk} is set equal to 1.25% for concrete and 1% for mortar. The value of C^*_{alk} is smaller for mortar since c/a is higher in a mortar and we calculate the alkali content as a function of cement (c/a = cement-to-aggregate ratio, by mass). It would be better to find an empirical equation for C^*_{alk} as a function of c/a, but there are not enough experimental data to verify that equation.

We consider two sets of experiments to assess the effect of alkali content. The first is the same as that already considered in analyzing the effect of ASR on the degradation of mechanical properties. The second is Ben Haha's (2006, 2007) set of tests of saturated mortar prisms of size $40 \times 40 \times 160$ mm. The experimental and predicted results for different alkali contents are compared in Fig. 7a. The predictions are in good agreement with the experimental results.

11. Effect of temperature on ASR-induced expansion

Like in all chemical reactions, the temperature change alters the ASR kinetics [31,36–41], and this causes changes in the ASR-induced expansion and damage. The temperature effect is considered to follow the Arrhenius equation (Fig. 7b) for permeability of water through the ASR gel, for initial diffusivity of cement mortar around the aggregate, and for permeability of the ASR gel; here T = current absolute temperature, R = universal gas constant.

For the experimental comparisons and calibration, Ben Haha's tests [25,26] were used again to assess the ability of the model in predicting the effect of temperature. Fig. 7b shows the experimental vs. predicted results for concrete and mortar prisms. The fits are seen to be quite close.

12. Conclusion

The mechanical analysis as well as the attainment of a good agreement of numerical predictions with the experimental observations confirm that both the long-term creep and the long-term diffusion, which causes the ASR gel to penetrate into pores and new cracks in the mineral aggregates and cement mortar near aggregate pieces, are important mechanisms in ASR damage to structures. They mitigate the damage substantially.

Acknowledgment

Partial financial supports from the NEUP Program of the U.S Department of Energy under grant DE-AC07-05/D14517, and from the U.S. National Science Foundation under grant CMMI-1153494, both to Northwestern University, are gratefully acknowledged

References

[1] T.E. Stanton, Expansion of concrete through reaction between cement and aggregate, Trans. Am. Soc. Civil Eng. 107 (1942) 54–84.
[2] V. Saouma, Y. Xi, Literature review of alkali aggregate reactions in concrete dams. Report cu/sa-xi-2004/001, Department of Civil, Environmental, & Architectural Engineering University of Colorado, 2004.
[3] J. Pan, Y. Feng, J. Wang, Q. Sun, C. Zhang, D. Owen, Modeling of alkali-silica reaction in concrete: a review, Front. Struct. Civil Eng. 6 (2012) 1–18.
[4] M. Alnaggar, G. Cusatis, G. Di Luzio, Lattice discrete particle modeling (LDPM) of alkali silica reaction (ASR) deterioration of concrete structures, Cem. Concr. Compos. 41 (2013) 45–59.
[5] F.C. Caner, Z.P. Bažant, Microplane model M7 for plain concrete. I: formulation, J. Eng. Mech. 139 (2013) 1714–1723.
[6] F.C. Caner, Z.P. Bažant, Microplane model M7 for plain concrete. II. Calibration and verification, J. Eng. Mech. 139 (2013) 1724–1735.
[7] Z.P. Bažant, A. Steffens, Mathematical model for kinetics of alkali-silica reaction in concrete, Cem. Concr. Res. 30 (2000) 419–428.
[8] Z.P. Bažant, S. Rahimi-Aghdam, Diffusion-controlled and creep-mitigated ASR damage via microplane model. I: Mass concrete, J. Eng. Mech. 143 (2016) 04016108.
[9] S. Rahimi-Aghdam, Z.P. Bažant, F.C. Caner, Diffusion-controlled and creep-mitigated ASR damage via microplane model. II: material degradation, drying, and verification, J. Eng. Mech. 143 (2016) 04016109.
[10] Z.P. Bažant, B.H. Oh, Crack band theory for fracture of concrete, Matér. Constr. 16 (1983) 155–177.
[11] Z.P. Bažant, J. Planas, Fracture and Size Effect in Concrete and Other Quasibrittle Materials, Vol. 16, CRC press, 1997.
[12] Z.P. Bažant, Numerically stable algorithm with increasing time steps for integral-type aging creep, in: Proc., 1st International Conf. on Structural Mechanics in Reactor Technology, 1971.
[13] M. Jirásek, Z.P. Bažant, Inelastic Analysis of Structures, John Wiley & Sons, 2002.
[14] M.H. Hubler, R. Wendner, Z.P. Bažant, Statistical justification of model B4 for drying and autogenous shrinkage of concrete and comparisons to other models, Mater. Struct. 48 (2015) 797–814.
[15] Z.P. Bažant, Q. Yu, G.-H. Li, Excessive long-time deflections of prestressed box girders. I: record-span bridge in Palau and other paradigms, J. Struct. Eng. 138 (2012) 676–686.
[16] Z.P. Bažant, Y. Xi, Continuous retardation spectrum for solidification theory of concrete creep, J. Eng. Mech. 121 (1995) 281–288.
[17] S. Rahimi-Aghdam, Z.P. Bažant, G. Cusatis, Extended Microprestress-Solidification Theory (XMPS) for Long-Term Creep and Diffusion Size Effect in Concrete at Variable Environment, 2018, ArXiv e-prints, 2018arXiv180505469R.
[18] E. Detournay, H.-D. Cheng, Fundamentals of poroelasticity, in: Analysis and Design Methods: Comprehensive Rock Engineering: Principles, Practice and Projects, 2014, pp. 113.
[19] T. Ahmed, E. Burley, S. Rigden, The effect of alkali-silica reaction on the fatigue behaviour of plain concrete tested in compression, indirect tension and flexure, Mag. Concr. Res. 51 (1999) 375–390.
[20] C. Gravel, G. Ballivy, K. Khayat, M. Quirion, M. Lachemi, Expansion of AAR concrete under triaxial stresses: simulation with instrumented

concrete block, in: Proc. 11th Int. Conf. AAR, Quebec, Canada, 2000, pp. 949–958.
[21] C. Larive, A. Laplaud, M. Joly, Behavior of AAR-affected concrete: experimental data, in: Proc. 10th Int. Conf. AAR, Melbourne Australia, 1996, pp. 670–677.
[22] S. Multon, F. Toutlemonde, Effect of applied stresses on alkali-silica reaction-induced expansions, Cem. Concr. Res. 36 (2006) 912–920.
[23] R. Swamy, M. Al-Asali, Engineering properties of concrete affected by alkali-silica reaction, ACI Mater. J. 85 (1988) 367–374.
[24] Z.P. Bažant, V.T. Chau, S. Rahimi-Aghdam, Three-phase cracked porous medium: shale fracking and ASR damage, in: Poromechanics VI (Sixth Biot Conference on Poromechanics, held in Paris France, July.), 2017, pp. 1–8, ASCE.
[25] M. Ben Haha, Mechanical effects of alkali silica reaction in concrete studied by SEM-image analysis, PhD thesis, 2006.
[26] M. Ben Haha, E. Gallucci, A. Guidoum, K.L. Scrivener, Relation of expansion due to alkali silica reaction to the degree of reaction measured by SEM image analysis, Cem. Concr. Res. 37 (2007) 1206–1214.
[27] L. Clark, Structural aspects of alkali-silica reaction, Struct. Eng. Rev. 2 (1990) 81–87.
[28] L. Monette, J. Gardner, P. Grattan-Bellew, Structural effects of the alkali-silica reaction on non-loaded and loaded reinforced concrete beams, in: Proc., 11th Intern. Conf. on Alkali Aggregate Reaction, 2000, pp. 999–1008.
[29] K. Ono, Strength and stiffness of alkali-silica reaction concrete and concrete members, Struct. Eng. Rev. 2 (1990) 121–125.
[30] T. Siemes, J. Visser, Low tensile strength in older concrete structures with alkali-silica reaction, in: 11th International Conference on Alkali-Aggregate Reaction, Québec, Canada, 2000, pp. 1029–1038.
[31] R. Swamy, M. Al-Asali, Influence of Alkali-Silica Reaction on the Engineering Properties of Concrete in Alkalies in Concrete, ASTM International, 1986.
[32] R.N. Swamy, The Alkali-Silica Reaction in Concrete, CRC Press, 2002.
[33] S. Rahimi-Aghdam, Z.P. Bažant, M.A. Qomi, Cement hydration from hours to centuries controlled by diffusion through barrier shells of CSH, J. Mech. Phys. Solids 99 (2017) 211–224.
[34] J. Guédon-Dubied, G. Cadoret, V. Durieux, F. Martineau, P. Fasseu, V. Van Overbecke, Study on tournai limestone in antoing cimescaut quarry-petrological, chemical and alkali reactivity approach, in: Proceedings of the 11th international conference on AAR in concrete Quebec City, Canada, 2000, pp. 335–344.
[35] R. Sibbick, C. Page, Susceptibility of various UK aggregates to alkali-aggregate reaction, in: The Ninth International Conference on Alkali-Aggregate Reaction in Concrete, July 1992, London, vol. 2, 1992.
[36] A.D. Jensen, S. Chatterji, P. Christensen, N. Thaulow, H. Gudmundsson, Studies of alkali-silica reaction-part I a comparison of two accelerated test methods, Cem. Concr. Res. 12 (1982) 641–647.
[37] T. Jones, New interpretation of alkali-silica reaction and expansion mechanisms in concrete, Chem. Ind. (1988) 40–44.
[38] H. Olafsson, The effect of relative humidity and temperature on alkali expansion of mortar bars, in: Proc., 7th Int. Conf. on Alkali Aggregate Reaction in Concrete, 1986, pp. 461–465.
[39] C. Larive, Apports combinés de l'expérimentation et de la modélisation à la compréhension de l'alcali-réaction et de ses effets mécaniques, PhD thesis, École Nationale des Ponts et Chaussees, Paris, 1997.
[40] M. Salomon, J. Panetier, Quantification du degré d'avancement de l'alcali-réaction dans les bétons et la néofissuration associée, in: Proc. 3rd CANMET/ACI Int. Conf. on Durability of Concrete, Nice, France, 1994, pp. 383–401.
[41] R. Pleau, M. Bérubé, M. Pigeon, B. Fournier, S. Raphaël, Mechanical behaviour of concrete affected by ASR, in: Proc. 8th Int. Conf. on Alkali-Aggregate Reaction, Soc. of Mat. Sci, Kyoto, Japan, 1989, pp. 721–726.

Available online at
ScienceDirect
www.sciencedirect.com
Hormigón y Acero 2019; 69(S1):15–19
www.e-ache.com
www.elsevierciencia.com/hya

Changes in mechanical properties of concrete due to ASR

Cambios en las propiedades mecánicas del hormigón debido a la ASR

Hans W. Reinhardt [a,*], Hasan Özkan [b], Oliver Mielich [c]

[a] *Prof. Dr.-Ing., Department of Construction Materials, University of Stuttgart, Stuttgart, Germany*
[b] *Dipl.-Ing., Materials Testing Institute, University of Stuttgart, Stuttgart, Germany*
[c] *Dr.-Ing., Materials Testing Institute, University of Stuttgart, Stuttgart, Germany*

Received 24 August 2017; accepted 9 February 2018
Available online 25 April 2018

Abstract

Alkali-Silica Reaction (ASR) is one of the most severe damage reactions of concrete. There are at least two different mechanisms of ASR: The most common is the rapid disruption of siliceous aggregates at the surface of the grain, which occurs in flint and opal sandstone, for example: The others are called slow reacting aggregates, and refer, for example, to cracking of the grain of greywacke and quartz porphyry. Both reactions are due to the dissolving of SiO_2 by alkalis. The present paper reports on tests on slow reacting aggregates.

While most studies in the literature concentrate on the expansion behavior of the aggregates, in this article focus is centered on the mechanical properties, such as strength and creep. The aggregates used are greywacke, quartz porphyry, and crushed sediments from the Upper Rhine Valley.

Keywords: Concrete; Alkali-silica reaction (ASR); Expansion; Mechanical properties; Creep modulus

Resumen

La reacción álcali-sílice (ASR) es uno de los deterioros más importantes que se produce en el hormigón. Existen principalmente dos mecanismos de ASR: El más común es la irrupción rápida de los áridos silíceos en la superficie del grano que por ejemplo sucede con el pedernal y la arenisca opal, mientras que los otros mecanismos son los de áridos de reacción lenta y, por ejemplo se refieren al agrietamiento del grano de grauvaca y pórfido de cuarzo. Ambas reacciones se deben a la disolución del SiO_2 por los álcalis. El presente trabajo versa sobre ensayos en áridos de reacción lenta.

Mientras que la mayoría de las investigaciones en la literatura se concentran en el comportamiento de expansión de los áridos, nosotros nos centramos en las propiedades mecánicas tales como resistencia mecánica y fluencia. Los áridos utilizados son grauvaca, pórfido de cuarzo y sedimentos triturados del Valle Alto del Rin.

Palabras clave: Hormigón; Reacción álcali-sílice (ASR); Expansión; Propiedades mecánicas; Módulo de fluencia

1. Introduction

ASR manifests itself mainly by expansion and cracking. The surface of concrete structures shows random cracking or, dependent of the loading direction longitudinal or transverse cracking. It happens very frequently that such structures are abandoned although the loading capacity is still sufficient. This was the starting point of the investigation with several questions: What are the remaining compressive strength and tensile strength, what are the deformations due to expansion of the aggregates, due to shrinkage and creep when ASR happens. It may be more economic to analyze the state of a structure taking account of inherent mechanical properties and monitor the further behav-

* Corresponding author.
E-mail address: reinhardt@iwb.uni-stuttgart.de (H.W. Reinhardt).

https://doi.org/10.1016/j.hya.2018.02.001
0439-5689/

ior instead of demolishing the structure. That means that the mechanical properties have to be known.

In the current investigation, four types of aggregates have been used: a crushed greywacke from the Harz (GW), crushed gravel from the Upper Rhine Valley (OR), quartz porphyry from Halle (QP), and another quartz porphyry from the Black Forrest (QPSW). According to the 40 °C fog-room test [1] the first three aggregates were alkali sensitive while the forth aggregate was insensitive. The first three aggregates belong to the category of slow reacting aggregates i.e. an ASR damage would occur in practice only after about 15 years. However there are many structures mainly in the East part of Germany, which suffer from such signs of deterioration.

2. Concrete composition

A CEM I 32.5 R according to EN 197-1 [2] was used with addition of K_2SO_4 to the mixing water such that the $Na_2O_{equi.}$ amounted to 1.30 M-%. The concrete was made with 400 kg/m^3 cement and a water to cement ratio of 0.45. 30 M-% of the aggregates were inert quartz sand up to 4 mm, 70 M-% were the coarse aggregates up to 16 mm grain size. The grading curve followed almost a Fuller parabola.

3. Testing program

For strength testing, 150 mm cubes and cylinders with 150 mm diameter and 300 mm length were produced. Modulus of elasticity, creep and shrinkage were determined on cylinders, compressive strength on cubes, tensile strength on dog-bone specimens, deformation due to ASR in the 40 °C fog room on cylinders. Testing took place before and directly after installation of the 28 days moist cured specimens in the fog room and after 140, 280 and 560 days storage in the fog room.

For creep testing, cylinders were mounted in the test rig. The compressive force was applied by a hydraulic ram and held constant by Belleville springs. The deformation was measured with dial gauges. The stress was decided to be one third of the characteristic strength of concrete after 28 days standard curing. The specimens were taken out of the fog room after the predetermined time, transported to the creep room with constant climate of 23 °C and 80% RH, mounted in the test rig, and loaded. 80% RH was used because ASR had to continue, from experience it is known that ASR would stop at lower relative humidity [3].

4. Testing results

4.1. Expansion in the fog room

Concrete which is affected by ASR typically exhibits expansion in moist environment. The specimens were stored at 40 °C and almost 100% RH for a certain time. The length change is plotted in Fig. 1. The dots give the experimental results, the lines are generated with the approximation function of Larive [4].

Obviously, the crushed gravel from the Upper Rhine Valley expanded most, the greywacke is second, quartz porphyry from Halle is three, and quartz porphyry from the Black Forest

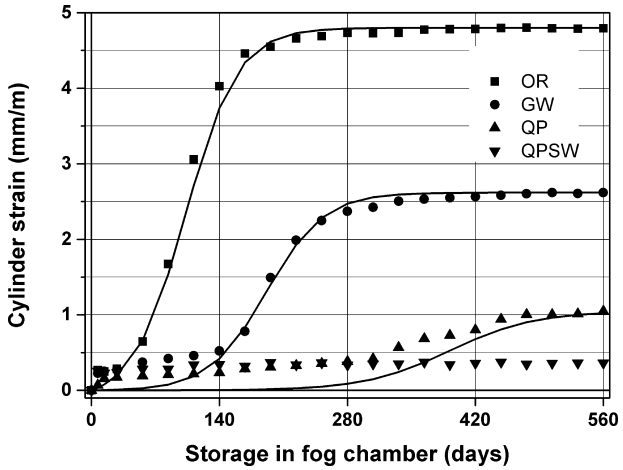

Figure 1. Expansion of specimens in the fog room, function of Larive [4]: $\varepsilon(t) = \varepsilon^{\infty} \frac{1-e^{-\frac{t}{\tau Carac}}}{1+e^{-\frac{(t-\tau Latence)}{\tau Carac}}}$.

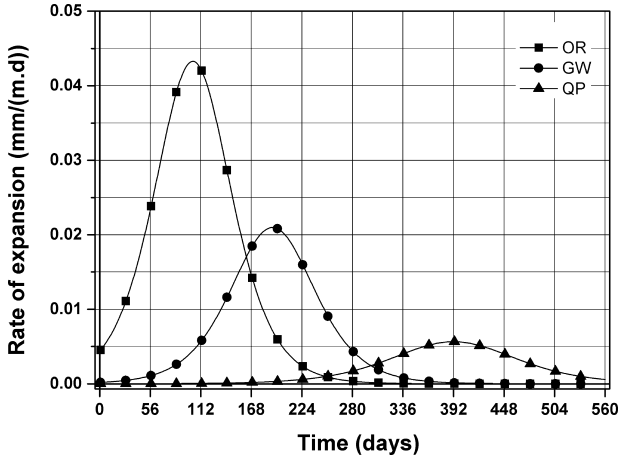

Figure 2. Rate of expansion.

does not expand. The expansion follows always an S-curve as known from Larive [4]. All lines start at a low level, increase then strongly and finally stay with an asymptotic maximum. The time of strong increase depends on the reactivity of the aggregate. The rate of expansion is plotted in Fig. 2, it represents the first derivative of the Larive function.

Three aggregates were suitable for the determination of the expansion rate, crushed gravel from the Upper Rhine Valley (OR), greywacke (GW) and quartz porphyry (QP). OR exhibits the maximum at 130 d while GW shows the maximum at 190 d. QP is less pronounced with a maximum at 392 d. The typical shape of the curve is very important and can later be used for the prediction of expansion in real structures.

4.2. Modulus of elasticity

It has been discussed before [5] that the dynamic modulus of elasticity is not a reliable measure to characterize ASR. The static modulus, however, depends strongly on the degree of ASR [6]. Therefore, the modulus has been determined in static experiments according to [7]. Table 1 shows the results.

Table 1
Static modulus of elasticity of concrete measured after a certain storage time in the fog room in MPa (in brackets: the relative value in %), mean of three specimens.

Type of aggregate	After 28 d curing	Storage time in 40 °C fog room in days		
		140	280	560
OR	37,702 (100)	15,805 (42)	20,750 (55)	28,934 (77)
GW	40,302 (100)	43,391 (108)	16,440 (41)	25,931 (64)
QP	36,031 (100)	41,078 (114)	41,551 (115)	22,342 (62)
QPSW	31,729 (100)	38,682 (122)	39,543 (125)	40,191 (127)

Table 2
Compressive strength of concrete in MPa measured after a certain storage time in the fog room (in brackets: the relative value in %), mean of three specimens.

Type of aggregate	After 28 d curing	Storage time in 40 °C fog room in days		
		140	280	560
OR	52.1 (100)	57.9 (111)	61.5 (118)	65.4 (125)
GW	50.6 (100)	69.2 (137)	71.4 (141)	72.7 (143)
QP	53.4 (100)	69.6 (130)	74.5 (140)	81.5 (153)
QPSW	54.5 (100)	72.5 (133)	74.2 (136)	83.8 (154)

The elastic modulus of crushed gravel of the Upper Rhine valley decreases strongly after 140 d and exhibits only 42% of the original value. Thereafter it increases again. The other aggregates show an opposite behavior. The modulus increases due to good hydration conditions (40 °C and water saturation of the ambient air) firstly and decay only after 280 or 560 days. The insensitive quartz porphyry from the Black Forest increases continuously. Comparing with Fig. 2 shows that the minimum value of the elastic modulus coincides roughly with the maximum reaction rate.

4.3. Compressive strength

Compressive strength has been determined on 150 mm cubes. Table 2 shows the results as mean of three specimens.

All concretes start at about 50 MPa and increase continuously to 65–84 MPa depending on the aggregate. The strength increase is also due to the favorable hydration conditions. Obviously, ASR did not affect the compressive strength which means that the compressive strength cannot be used as indicator of ASR.

4.4. Tensile strength

The investigation of the splitting tensile strength was very limited. The results of aggregate OR and QP are shown in Table 3.

The strength of OR decays after 140 days in the fog room to 1.15 MPa which is only 25% of the original value, it recovers to 31% after 280 days and to 44% after 560 days. Fig. 1 with the expansion of concrete has shown a strong expansion at about 140 days which explains the reduction of the tensile strength. Slow/late aggregate grains exhibit fracture in the grain [8] and, since the grain is responsible for the load transfer one must conclude that ASR has caused the strength loss. With ongoing

Table 3
Tensile strength of concrete in MPa measured after a certain storage time in the fog room (in brackets: the relative value in %), mean of two specimens.

Type of aggregate	After 28 d curing	Storage time in 40 °C fog room in days		
		140	280	560
OR	4.68 (100)	1.15 (25)	1.43 (31)	2.04 (44)
QP	3.99 (100)	3.40 (85)	–	3.19 (80)

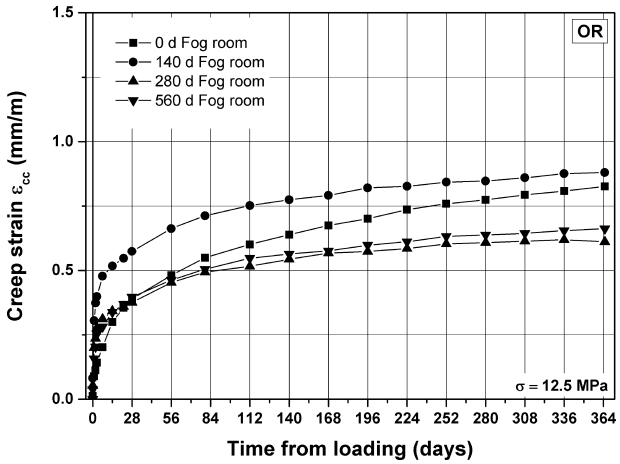

Figure 3. Creep strain of aggregate OR.

hydration strength recovers partly but cannot reach the original value again. QP shows respective values of 117% after 280 days and 80% after 560 days. A look to Fig. 1 reveals that ASR has started only after about 320 days which means that ongoing hydration has caused the strength increase at 280 days. Later strength decreases to 80% due to ASR. Comparing the development of compressive strength with tensile strength, the two properties do not follow the same manner. This has been reported also by other researchers [9]. Thus, the tensile strength is a better indicator for ASR than compressive strength.

4.5. Creep under compressive load

Figs. 3–6 show the development of strain with time as mean of two specimens. The stress is constant during the time under load, however it depends on the aggregate. As said before the stress level has been chosen as one third of the characteristic strength after 28 days standard curing. The diagrams give the information. The legend informs about the pre-storage in the 40 °C fog room. Of course, this situation is artificial, however since the climate in the testing room is taken constant with 80% RH one can assume that ASR is still progressing. (Remark: Although the creep strains are negative (shortening) they are plotted with a plus sign, i.e. as absolute values.)

Fig. 3 refers to the crushed gravel of the Upper Rhine Valley.

The specimens exhibit the typical behavior. Creep is progressing the most in the first 28 days thereafter creep rate diminishes. One must have in mind that the specimens underwent a specific pre-conditioning and that they are of different age. The two aspects may be opposing each other. The amount of creep is

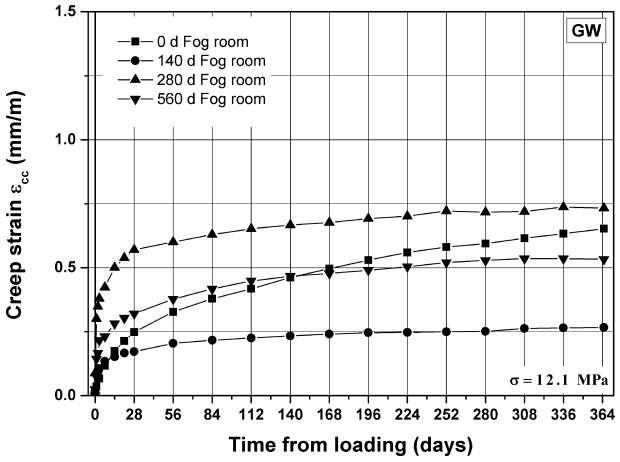

Figure 4. Creep strain of aggregate greywacke.

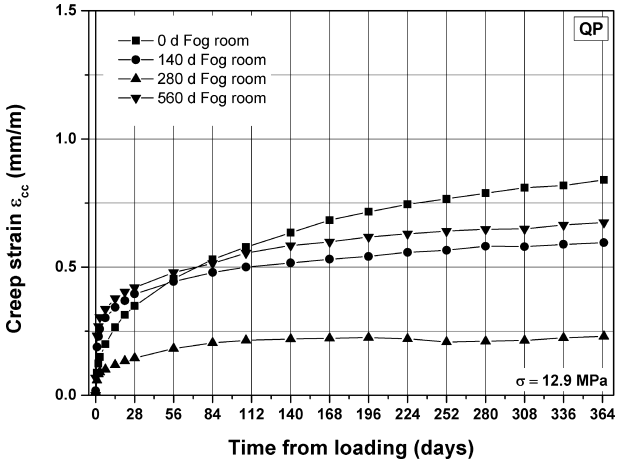

Figure 5. Creep strain of aggregate QP.

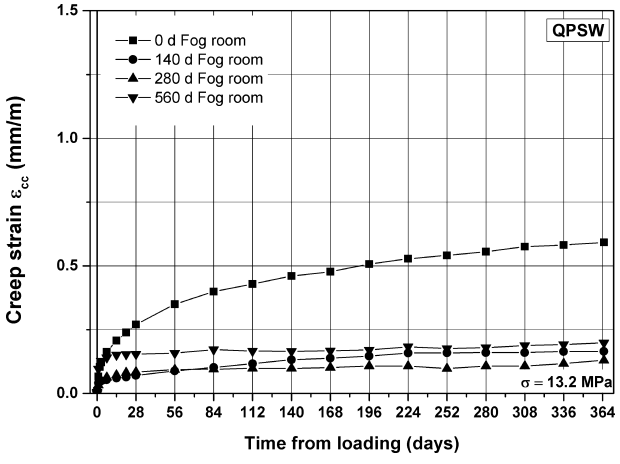

Figure 6. Creep strain of aggregate QPSW.

largest for the specimens which were stored in the fog room for 140 days. Looking to Fig. 2 one can see that this is the time of strongest reaction. The specimens with 280 and 560 days storage show less creep which is a token of greater hydration.

Fig. 4 belongs to the greywacke.

Table 4
Creep modulus of concrete in MPa measured after 365 days loading and after a certain pre-storage time in the fog room, mean of two specimens.

Pre-storage	Type of aggregate			
	OR	GW	QP	QPSW
28 days moist curing	10,520	12,518	10,967	13,214
140 days in fog room	6117	21,393	14,159	25,056
280 days in fog room	11,596	5956	23,195	28,021
560 days in fog room	11,030	10,531	9480	25,154

The curves more spread than it was in the case of OR. The largest creep occurs for concrete which was stored in the fog room for 280 days. This time coincides roughly with the time of greatest ASR reaction. The lower curve for 140 days must be caused by more hydration compared to the curve without storage in the fog room. The 560 days curve must be attributed to the ongoing ASR.

Fig. 5 shows the results of the quartz porphyry from Halle.

The concrete which had no pre-treatment in the fog room shows the largest creep. Compared to the others it is the youngest concrete. The line for the 140 d concrete is lower and the line for the 280 d concrete is even lower. This behavior can be attributed to the ongoing hydration without effect of ASR. The line for the 560 d pre-treatment approaches almost the line of the zero concrete, i.e. ASR influences creep considerably.

Fig. 6 refers to the quartz porphyry from the Black Forrest, the aggregate which is insensitive to ASR.

This figure shows best the influence of progressing hydration. The zero pre-treatment concrete exhibits the largest creep and the other lines lie close together.

Comparing the four foregoing figures, one can see a common feature: The aggregates which are ASR sensitive show a larger creep than the insensitive aggregate QPSW. The aggregates OR and GW which undergo the largest expansion due to ASR show larger creep strain than the lass expanded QP. On the other and, the simultaneous influence of absolute age of concrete became obvious.

5. Creep modulus

If structures have to be analyzed with respect to long-term deformation one can have a look to polymer technology. To this end, their engineers use the so-called creep modulus. The creep modulus E_{cr} is the quotient of stress divided by the load induced strain $E_{cr} = \sigma/(\varepsilon_{el} + \varepsilon_{cr})$ with ε_{el} the elastic strain and ε_{cr} the creep strain. The creep modulus could also be used for concrete structures. Table 4 shows the numbers calculated with the deformation at one year (without shrinkage, of course).

The creep modulus diminishes with loading time because creep increases, that is why the first row shows considerably smaller values than the ones in Table 1 which contains Young's modulus. The pre-storage in the 40 °C fog room affects the creep modulus again. The aggregate OR shows the largest decrease after 140 d, GW has the least value after 280 days, QP follows after 560 days fog-room storage. One depicts here the same tendency as has been discussed with creep. As expected,

QPSW exhibits the largest values. It also reflects the feature of Figs. 1 and 2.

6. Outlook

The aim of the investigations was to increase the knowledge with respect to short-time and long-time mechanical properties of ASR affected concrete. The knowledge is suitable for the analysis of the state structures in the light of loading capacity and deformation. However, there are several disciplines questioned: firstly, the testing results have to be transposed to real life of the structure, secondly, ASR development has to be modeled for the structure in terms of time and space, and thirdly, an ASR affected structure should be monitored continuously. As the first point is concerned there are results of ASR at real exposure which show that the development of ASR takes about ten times more time than in the 40 °C fog room [10]. The second point can be satisfied with the aid of modern finite-element codes which take account of physical aspects (diffusion, permeation, temperature, humidity) and stress [11]. The nowadays monitoring techniques are able to monitor continuously and wireless the crucial spots of structures [12]. In any case there is a strong demand for good knowledge of the material.

7. Final conclusions

The investigations have been performed on concrete with three types of slow reacting alkali sensitive aggregates and one insensitive aggregate. The following conclusions can be drawn.

The expansion due to ASR measured after a certain storage time in the 40 °C fog room follows an S-curve for the three concretes with alkali sensitive aggregate. The time of maximum reaction rate is strongly dependent on the type of aggregate.

The static modulus of elasticity decreases with ASR to a minimum value and increases thereafter again. The time of minimum coincides roughly with the maximum reaction rate.

The compressive strength seems not to be affected by ASR.

The tensile strength decays with time in the fog room. Compressive and tensile strength do not follow the same behavior.

Creep is enlarged by ASR. The largest creep rate goes together with the largest progress of ASR.

As a mean for the analysis of long-term deformation the creep modulus has been calculated which shows a similar tendency as creep.

The outlook provides some ideas how the gained knowledge can be used in the analysis of structures in real environment.

All conclusions are only valid for the material tested. One has to be very cautious in drawing general conclusions because the aggregates are of natural origin and vary from place to place. It can happen that rocks taken from the same quarry differ strongly.

Acknowledgement

The first author has experienced a long lasting friendship with Carmen Andrade. We met at many events of RILEM, at committee meetings, symposia and workshops. Carmen showed always much interest in various fields which have triggered research of common interest. Thank you. Ad multos annos!

The German Research Community has greatly supported the project under RE 691/39-1 which is thankfully acknowledged.

References

[1] Deutscher Ausschuss für Stahlbeton (DAfStb), Vorbeugende Maßnahmen gegen schädigende Alkalireaktion im Beton (Alkali Richtlinie), Beuth Verlag, Berlin, Deutscher Ausschuss für Stahlbeton, Oktober, 2013.

[2] EN 197-1: 2011 Cement. Composition, specifications and conformity criteria for common cements.

[3] D. Stark, The moisture condition of field concrete exhibiting alkali silica reaction, in: Durability of Concrete, 2nd Int. Conf. Montreal Canada, Vol. II ACI, SP 126, Detroit, 1991, pp. 973–987.

[4] C. Larive, Apports combinés de l'expérimentation et de la modélisation à la compréhension de l'alcali-réaction et de ses effets mécaniques, thèse de doctorat, L'École Nationale de Ponts et Chaussées, 1997.

[5] H.W. Reinhardt, O. Mielich, Static vs. dynamic Young's modulus as indicator for ASR degradation, in: C. Leung, K.T. Wan (Eds.), Advances in Construction Materials through Science and Engineering, 2011, RILEM PRO 79, S. 104 (Abstract book) ISBN 978-2-35158-116-2.

[6] P. Helene, M. Carvalho, J. Pachero, Engineering field tests for alkali-aggregate reaction, Struct. Concr. J. Fib. 18 (2017) 349–355.

[7] DIN 1048-5: 1991 Testing methods for concrete; hardened concrete, specially prepared specimens.

[8] H.W. Reinhardt, O. Mielich, Fracture toughness of alkali-sensitive rocks in alkaline solution, Int. J. Rock Mech. Min. Sci. 70 (2014) 552–558.

[9] "Alkali-aggregate reaction concrete" (ICAAR), proceedings volumes since 1974.

[10] E. Siebel, M. Böhm, I. Borchers, C. Müller, J. Bokern, E. Schäfer. AKR-Prüfverfahren – Vergleichbarkeit und Praxis-Relevanz, Betontechnische Berichte 2004–2006, VDZ Düsseldorf.

[11] J. Ožbolt, MASA – MAcroscopic Space Analysis. Bericht zur Beschreibung des FE Programmes MASA, Institut für Werkstoffe im Bauwesen, Universität Stuttgart, Stuttgart, 1998.

[12] C. Maierhofer, H.-W. Reinhardt, G. Dobmann, Non-destructive Evaluation of Reinforced Concrete Structures, vols. 1 and 2, Woodhead Publ, Oxford, 2010.

Las capacidades se demuestran
únicamente cuando se realizan
(Simone Parks)

El mejor homenaje a Carmen Andrade se lo hacen las mujeres con proyectos

Elia María Pérez García
ingeniera de caminos
ingeniera de proyecto

Miriam Alonso Sanz
arquitecta
jefa de proyecto

Raquel Baldellou Aguilar
arquitecta
responsable BIM estructuras

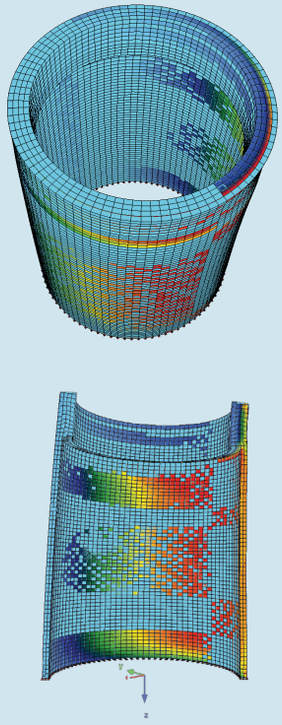

Proyecto y certificación
Torre eólica prefabricada 120 m
Parque Aracatí, Brasil
proyecto de CALTER para
CASSOL PRÉ-FABRICADOS

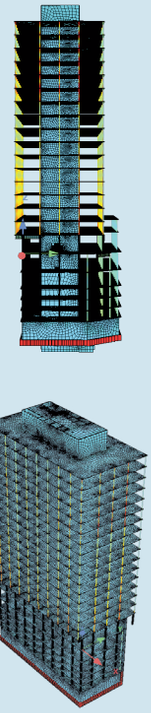

Proyecto de refuerzo
Edificio Castellana 77
Madrid, España
proyecto de CALTER para
LUIS VIDAL + ARCHITECTS

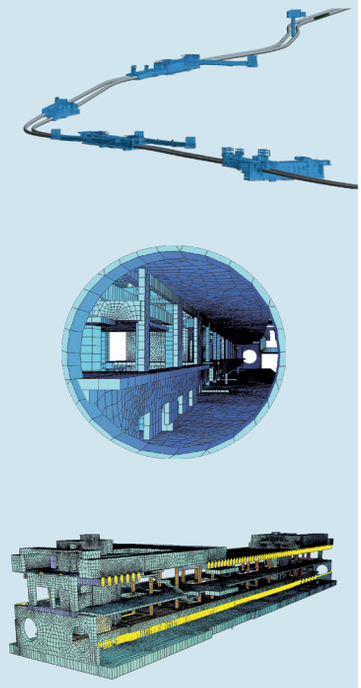

Proyecto de estructuras
Estaciones de metro
Doha, Catar
proyecto de CALTER para
SSF INGENIEURE

calter
ingeniería de estructuras

www.sofistik.es
sofistik@calter.es

Available online at
ScienceDirect
www.sciencedirect.com
Hormigón y Acero 2019; 69(S1):21–28
www.e-ache.com
www.elsevierciencia.com/hya

Original

Some historical notes on the research in corrosion of reinforcement

Apuntes históricos sobre la investigación en corrosión de armaduras

Carmen Andrade

International Center for Numerical Methods in Engineering, CIMNE, UPC, Spain

Received 20 December 2018; accepted 21 December 2018
Available online 22 January 2019

Abstract

A brief exercise is made on reporting some achievements in the history of reinforcement corrosion. It is a difficult task to try to summarize because there are numerous protagonists in the history then choices were made from a personal point of view. In the decade 1960–1970, reinforcement corrosion was a subject only of marginal interest because the number of built environment was limited. The use of electrochemical techniques was a milestone which enabled from the decade of the 1970 to study the effect of each variable with much more rigor. The studies on service life started in the decade of 1980, although they were not of general interest until next decade. From 1990 Rilem Committees and the Iberoamerican Program on Corrosion of CYTED extended the knowledge so widely that in the XXI century the subject attracts much research interest.

Keywords: History; Corrosion; Electrochemistry; Service life; Codes of practice

Resumen

Se realiza un breve ejercicio para comunicar algunos logros en la historia de la corrosión de armaduras. Tratar de resumirlos es una tarea difícil ya que hay numerosos protagonistas en la historia, por lo que las elecciones se han hecho desde un punto de vista personal. En la década 1960-1970, la corrosión de armaduras solo era un tema de interés marginal porque el número de entorno construido era limitado. El uso de técnicas electroquímicas fue un hito que permitió, desde la década de 1970, estudiar el efecto de cada variable con mucho más rigor. Los estudios sobre la vida útil comenzaron en la década de 1980 aunque no fueron de interés general hasta la siguiente década. Desde 1990, los Comités de la RILEM y el Programa Iberoamericano sobre Corrosión de CYTED ampliaron el conocimiento tan ampliamente que en el siglo XXI el tema genera mucho interés en investigación.

Palabras clave: Historia; Corrosión; Electroquímica; Vida útil; Códigos de prácticas

1. Introduction

I had the privilege of making a long journey of investigation on reinforcement corrosion and for that reason, also the responsibility of transmitting data and anecdotes that should be one stone with those of other. History is always polyhedral and has many interpretations. In present work I report some notes from a personal point of view. I am sorry for perhaps not being totally objective and not mentioning all the protagonists and all the important contributions. I will try to extend present notes in the future trying to be more comprehensive. I would like that the present work is taken as a testimony of some visionaries who promoted these studies, supported them, or were outstanding contributors to the science and practice of concrete durability.

Corrosion by itself is a major problem in the industry due to the enormous economic consequences involved. There are constant data on direct costs for material loss, and indirect costs, for stopping and putting out of service industrial components or infrastructure. The economic consequences of corrosion and the

E-mail address: candrade@cimne.upc.edu

https://doi.org/10.1016/j.hya.2018.12.002

need to mobilize the knowledge to avoid them, is one of the first issues that we explain to corrosion specialists and yet we are still not fully aware that it is necessary to intensify more preventive measures than corrective ones. In the field of concrete durability, there have been introduced very well preventive measures against the attack of the concrete itself, but there is still a long way to also efficiently prevent corrosion of the reinforcement.

Due to the numerous aspects that the corrosion of reinforcements involves, to make a summary of the historical evolution of the subject supposes a work of synthesis very remarkable. To try the challenge, it will be divided the history in decades paying much more attention to the initial times, less known at present. At initial times where the Polarization Resistance technique was proved to be a key tool in the study of the corrosion because it quantifies the phenomenon in a non-destructive manner and how this technique helps to predict the residual service life of a corroding structure. I beg the pardon for transmitting some personal anecdotes, that however is the time to report.

2. The beginnings in the 1970s: development of measurement techniques

At present, we are visiting structures that were erected either ignoring the word durability or thinking that concrete was the material that would make steel eternal. It was not until the 70s that some awareness began to grow that the concrete could be porous allowing aggressive substances to penetrate through or could not counter the action of some admixtures currently used at that moment as the $CaCl_2$. I joined the Eduardo Torroja Institute of Construction Sciences (IETcc) in June 1969, under the presentation of Enrique Costa Novella, Professor of Chemical Engineering at the Faculty of Madrid, to Prof José Calleja, the Head of the Department of Chemistry of the Institute. I was one of the selected students by Prof Costa him tutor of my Doctorate.

At that moment Prof. Calleja had already written an article [1] warning of the possible problem about the reinforcement corrosion because accelerator admixtures were a critical issue where still steam curing was not common, and then, calcium chloride was an accelerator of setting, especially interesting for prefabrication. Corrosion cases had started to be detected in some buildings having made use of the $CaCl_2$ and Prof. Calleja offered to me that subject. The alternative subject that Prof. Calleja proposed to me to develop my thesis was the study of the optimal addition of gypsum to regulate the setting of cement. I joined the Institute in June 1969, just after finishing my degree in Chemical Industry but it was not until September that the selection of reinforcement corrosion as subject for my Master was made. The final reason was that I perceived a higher interest of Prof. Calleja on it. From my part, just the chapter of corrosion was the last one of the matter of Metallurgy that was neither reached nor explained during my studies. So I selected the topic that I knew anything about.

Declared to Prof. Calleja my total ignorance on the basis of the subject in the chosen topic, he suggested that I attended at the Faculty the matter of "Corrosion and Protection" that Sebastián Feliu had begun to teach in the specialty of Metallurgy, a specialty that I had not studied. These classes were essential to bring to fruition the work of the Master Thesis presented in June 1970. From the experimental testing works I will mention some anecdotes in order the reader could place the mind on the state of the knowledge at that time. Thus, I remember the emotion of Prof. Calleja when I showed him the bars removed from my first specimens with admixed $CaCl_2$ and calcium formiate (Fig. 1): It is true that chloride corrodes!!! he said with great emphasis. That is to say, in 1970 they were the first results that in our country confirmed that calcium chloride should be banned as a setting accelerator. This corroborated result in the rest of the specimens (I manufactured 500 for the Master thesis) had two consequences:

- The protest and pressure on Prof. Calleja from the manufacturer of calcium chloride (Solvay) that were afraid to lose an application of enormous economic impact for them if $CaCl_2$ was forbidden
- The prohibition appeared in the version of the Spanish "Instruction of Calculation of Reinforced Concrete" of 1973, I deduced that after the proposal of Prof. Calleja. From then in Spain the use of calcium chloride added to the concrete mix proportions was forbidden. The amount in the mixing water should be lower than 0.4% referred to the cement weight.

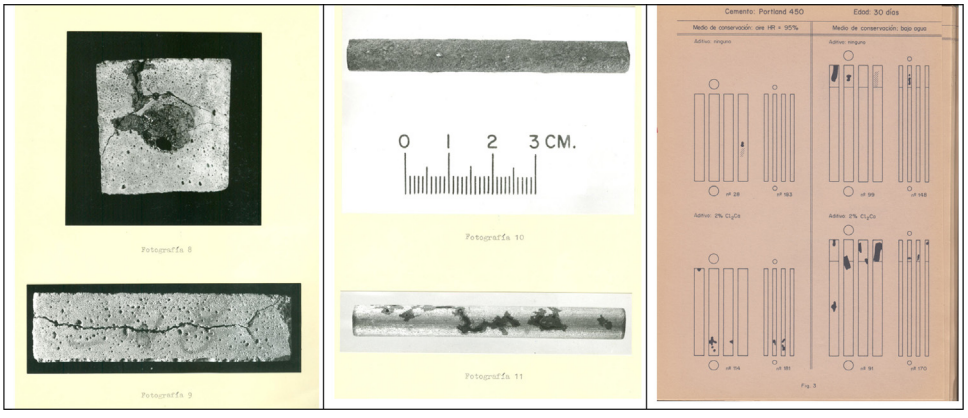

Figure 1. Left: specimens craked due to the corrosion induced by admixing $CaCl_2$ after 3 months in high humidity. Center: aspect of some bars, upper totally corroded and down with localized corrosion, right: drowns of each specimen handmade to reproduce the corrosion pattern.

Figure 2. Left: prestressed beam manufactured for the work of the thesis. Right: set of equipments to measure the electrical resistance due to the concrete itself, multimeter for measuring the corrosion potential and in the right-down corner the galvanostat (white cover in the figure) and the black multimeter to measure the current.

In the Master Thesis [2] the period of testing was only of 3 months. In spite of being short, some specimens cracked as shown in Fig. 1-left. In the right part of this figure is given the handmade drawn that I did for the 500 specimens because of the difficulty to make too many photographs. I had to reproduce by hand the pattern of the corrosion in each steel bar (4 sides of each bar).

I decided to continue with the Doctoral Thesis [3] on the same subject and go on to study inhibitors (nitrites, chromates and phosphates) that could compensate for the corrosive effect of chloride. The plan contemplated working with 12 different cements (those that were available then) and several inhibitors and concentrations. Given that I had manufactured 500 test pieces for the Master thesis, I raised the absolute need to develop a measurement technique that would save me having to break a test piece at each age. Prof. Feliu suggested the use of the Polarization Resistance technique, at that time a total novelty even at international level [4,5]. With the help of Prof. Feliú working not only at the University but also at the CENIM (National Center of Metallurgical Research) as Head of the Corrosion Department, and of José Antonio González researcher at CENIM and of José Fullea, a doctoral student, as me trying to apply the technique to the corrosion of lead in the sulfuric acid of car batteries. In my case it was the first time that that technique also named "Linear Polarization" was applied to concrete and that advance was immediately recognized when publishing in 1978 and 1980 in international journals with evaluators [6,7]. Since I was able to join the staff of the Institute in 1979, when shortly thereafter I requested to participate in a RILEM committee, all were congratulations and facilities, being in 1987 when the RILEM awarded me the Robert L'Hermite Medal to young researchers.

Fig. 2 shows, however, the precarious means that we then had for measuring. It shows a perspective of the beams 2 m long that I fabricated and the arrangement of equipment. The technique of the Polarization Resistance, R_p, consists of applying a small electric current (ΔI) and measuring the change of potential (ΔE) that this disturbance produces in the reinforcement. The following formula had been previously proposed by Stern in 1957 [8] but not proved to be reliable and with several papers doubting

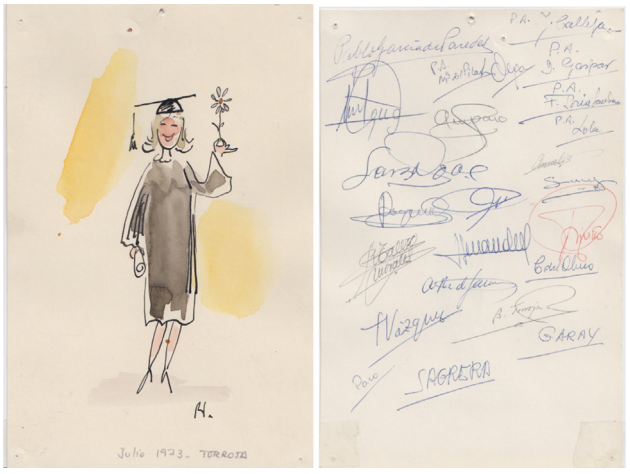

Figure 3. Gift for my doctoral Thesis of my colleagues painted by Bernard Petit.

of its applicability (B is a constant value which varies between 26 and 52 in the case of concrete):

$$I_{corr}(\mu A/cm^2) = \frac{B}{R_p} = \frac{B}{(\Delta E/\Delta I).area}$$

José Maria Tobío, then Head of the Department of Physics of the Institute, made for me a "galvanostat" following the indications of CENIM technicians, inside a wooden box with yellow plastic cover (see Fig. 2). The problem that made me invest a whole year to solve it, was that the internal resistances of this device did not allow to apply a polarization small enough for the small size of my specimens (2 × 2 × 8 cm with exposed surface around of 6 cm^2). I went on to manufacture prestressed beams of 2 m (Fig. 2, left). They were 48 beams and with them I carried out the studies that allowed to establish the conditions to apply this technique to measure the corrosion rate of a steel embedded in concrete. Bases that have been irrefutable and valid until the present, since there is still no better technique than this to quantify the corrosion rate, not only in concrete, but in any metal/electrolyte system. I presented the thesis in July 1973 [3]. In Fig. 3 is given the gift signed by my colleagues of the Department of a drawn from Bernard Petit, then a draftsman at the

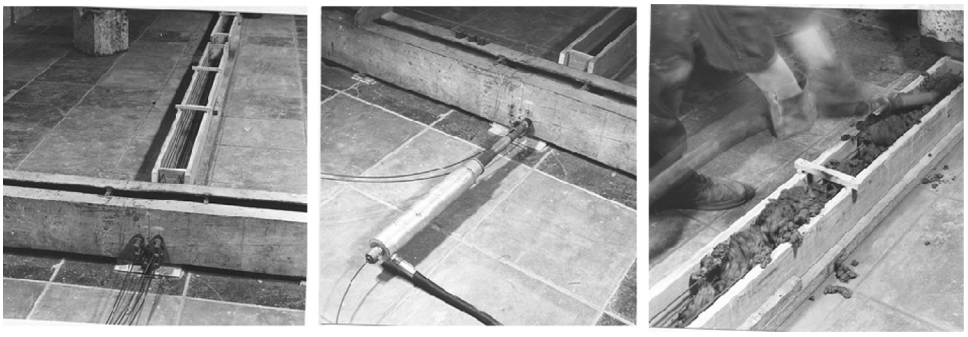

Figure 4. Prestressing arrangement for fabricating the 48 joists used fro the doctoral thesis.

Institute and then a famous painter of paintings with colored mortars.

As anecdotes of that period I find it seems to me interesting to rescue three:

- The first, deals with the fact that I was pregnant at the time of my first child, who was born a year before finishing the Thesis. The baby before and after birth was referred to as "Carmen's little thesis". At that time pregnant women stopped working and of course taking the baby to the nursery (from he was 3 months old during my writing of the thesis document) was greatly commented at work for good and bad.
- The second anecdote, was that the 48 beams first demanded much calculations and work at the structural laboratory for those who calculate and did the prestressing of the wires (never made before at the Institute (Fig. 4). Once fabricated the problem was that either occupy a large area or if stacked together their tremendous weight. Finally the beams were placed in the lab of the institute known as "the dungeons" since its floor was directly in the third basement on the ground and not on a floor. There, I locked myself for 7 h a day to measure with the galvanostat of the yellow plastic cover. Concentration was obligatory because nobody rarely came from those depths. I keep a great memory of that time of what happens to a prestressed beam when an electric current is applied to its wires. The several corrosion conditions of each beam were clearly differentiated through the results of the R_p values. Also during my Thesis studies I visited often the CENIM, where I had a place to work and access to all their equipment, a place I kept for a few years afterwards, in which I was even awarded a scholarship to study the corrosion resistance of galvanized reinforcements, until in 1979 year in which I joined the staff of the Institute of Construction Sciences.
- The third anecdote when I presented my thesis, was that Prof. Arredondo, then Director of the Institute, called me at his office to congratulate me and said solemnly: "You already know everything about corrosion, so you will have to go thinking in which new topic will work" My answer was confuse, something like "I do not think I know enough, I will need a lot of time to know something about this topic". I think today I would continue to answer in the same way.

2.1. Stress corrosion cracking studies in Spain

Simultaneously to the studies at the IETcc, the "Central Laboratory for Materials and Structures" of the Ministry of Public Affairs was also developing corrosion studies coordinated by Manuel Elices. They were made to find a solution for the colapses of prestressed pipes conducting the tap water to Madrid. Also guided by Prof. Calleja, I visited them very early in order to know each other and look for possible collaborations. These collaborations started one decade later when Elices moved to the Faculty of Civil Engineering to be Professor of Physics. More recently the group was one of the partners of the CONSOLIDER project together with CIMNE (Prof. Eugenio Oñate) and the IETcc. In that project was later incorporated the group of Prof. Gonzalo Ruiz of the University of Castilla-La Mancha. This project enabled to consolidate a fruitful collaboration that still remains.

The group of Prof. Elices was almost always working in the area of the effect of tensions in the corrosion and the development of fracture mechanics theories. All the group has made remarkable contributions in the subject of materials science of metallic and non-metallic materials [9–13].

In Fig. 5 is shown one of their contributions in which studied the stress concentration due to the existence of a crack with a semi-elliptic shape. Numerous other aspects have addressed by the group that have had international relevance awarding G. Guinea the RILEM Robert L'Hermite medal in 1994.

2.2. Studies in other countries in the 70s until 1980

Not many studies were active on the subject at the beginning of the 70s. In the Master Thesis I gathered everything I found tracing for hours in the library of the Institute and that of CENIM, and the number of citations that I got did not exceed 25. In the Thesis I found a bit more but not too many. I refer only few of them [14–20] because these remarkable works have already been completely forgotten. Also, I would like to name from those times other that should not be left unread so as not to repeat basic tests or question aspects that have been demonstrated since then [21–31].

Three problems can be identified that were studied at that time: corrosive effect of admixtures (among them calcium chloride), marine environments, and the corrosive effect of stray

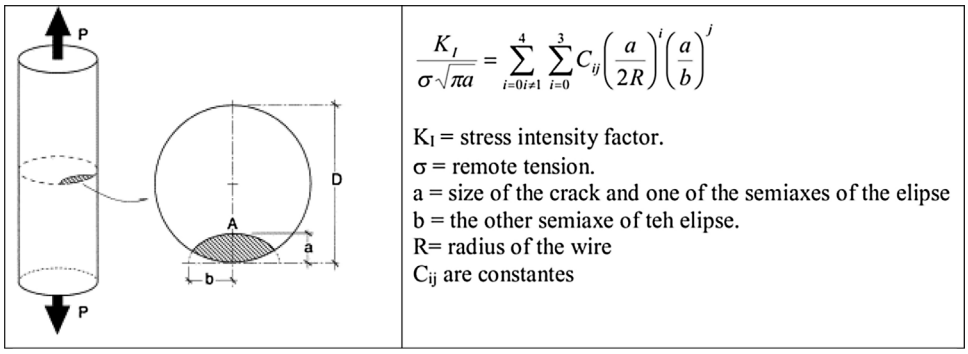

Figure 5. Stress intensity factor of the a semi-elliptic crack by the group of Prof. Elices [9–13].

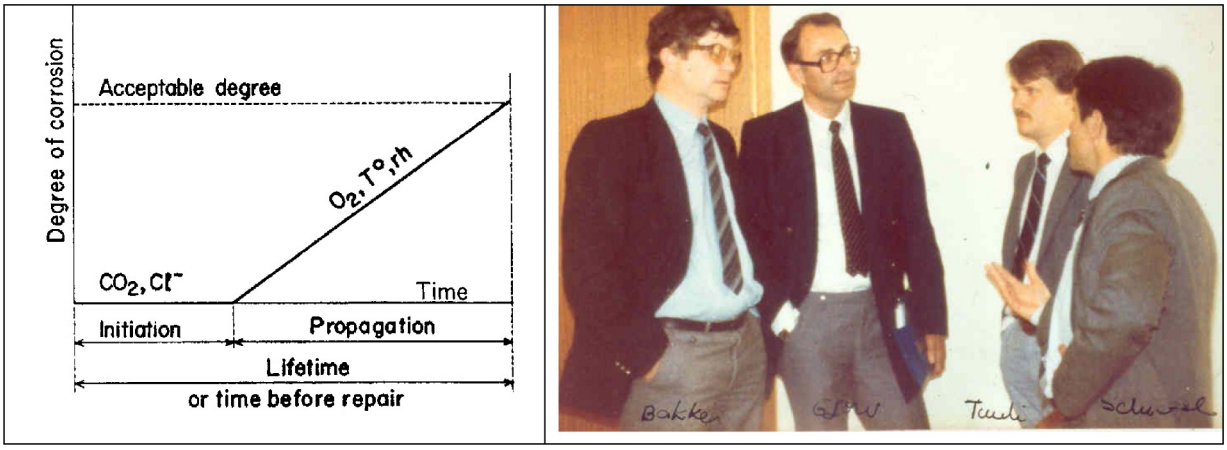

Figure 6. Left: diagram of service life in the thesis if K. Tuutti. Right: from the left to the right Rob Bakker (Holland), O. Gjorv (Norway), K. Tuutti (Sweden) and P. Schiessl (Germany) during a meeting of RILEM TC 60-Corrosion of Steel in concrete.

currents in the railways. The action of chlorides on hydration was studied in relation both to its mitigating effect of the sulfatic reaction in marine environments and its accelerating effect on the setting. It was outstanding the work of Hausmann [20], who establishes the critical relation of chlorides with respect to the pH of concrete at a value of Cl/OH = 0.6, value that has remained valid until today. Also Gouda and Monfore [14] were working in the same subject and in parallel Cigna [21]. The techniques that they applied were of accelerated type, fundamentally curves of polarization and also potentiostatic tests as that proposed by Kaesche and Baümel [16,17] later standardized by DIN and by CEN for the detection of corrosive substances in concrete. The publication of Page and Treadaway in Nature [21] supposed a disclosure of the problem in its basic aspects that contributed notably to the multiplication of congresses and publications.

3. Decades of 1980–2000: service life and corrosion mechanisms

The use of electrochemical techniques was a fundamental milestone that allowed, starting in 1970, to approach the studies with much more rigor on the effect of each variable. This is how the effects of carbonation [32] and the possible methods to avoid corrosion began to be studied, basically hot galvanizing [32], inhibitors [33], epoxy coatings for reinforcements [24] and cathodic protection [28].

It is nevertheless in the decade of 1980 when the calculation of service life was approached, that it was not object of general attention until the decade of 1990. Thus, K. Tuutti introduced the concept when he published his doctoral thesis [34] in 1982 with the diagram that is shown in Fig. 5 and that is extensively referred by all subsequent studies. Fig. 6 also shows K. Tuutti with Rob Bakker, Odd Gjorv and Peter Schiessl during a meeting of the Rilem Committee 60-CSC – "Corrosion of Steel in concrete" [35] chaired by Schiessl. Both this committee and the Workshops organized by Hans Arup of Force Institute in Denmark were important leaders of the work in the subject. For the sake of curiosity in Fig. 7 is given the group attending the first Workshop on Corrosion of Reinforcements in Copenhagen organized by Arup in 1981.

In Latinoamerican countries also the subject started to be studied in the decade of the 80s and the subsequent ones with great success due to the funds provided by the Program CYTED (Spanish Program on Cooperation for the Development) which enabled to establish several active Networks as they were "Durar" chaired by Oladis de Rincon from Venezuela [36], "Rehabilitar" chaired by Paulo Helene [37] from Brasil and "Prevenir" chaired by Pedro Castro [38] from Mexico. All of them with important original contributions in the subject.

In the early 80s it was demonstrated the reliability of the Polarization Technique by calibrating its results with gravimetric tests made on the same bars using Faraday's law for the

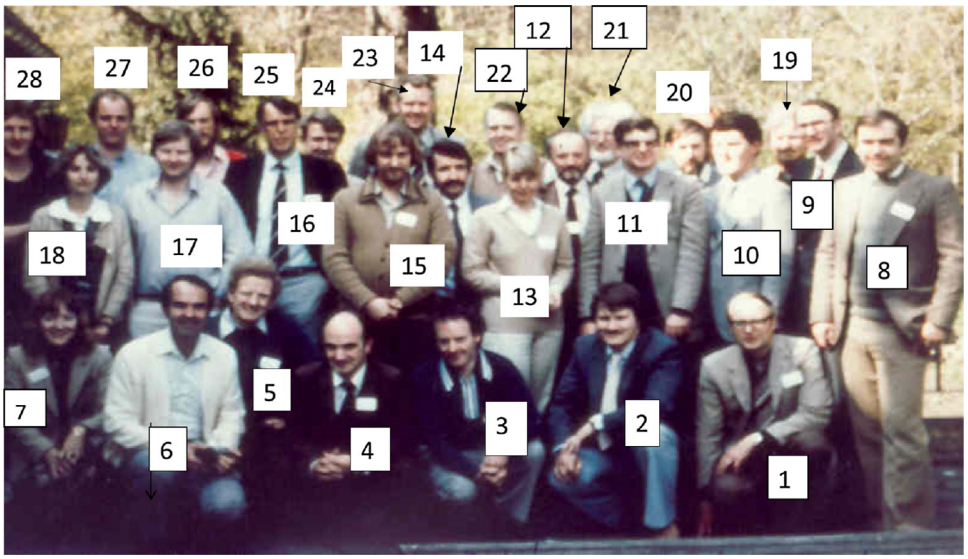

Figure 7. Participants in the workshop entitled 'Corrosion of steel in concrete' organized by Hans Arup at Copenhagen in 1981. In the *first row from right to left*: (2) K. Tuutti, (4) J.A. Gonzalez, (6) C. Locke, (7) C. Hansson, *second row*: (8) O. Vennesland, (9) O. Gjorv, (10) C. Page, (11) R. Bakker, (12) J. Dawson, (13) Byfors, (14) P. Schiessl, (17) G. John, (18) C. Andrade, *third row*: (21) Wilkins, (22) H. Arup.

Figure 8. Left the corrosion rate meter in a column with rough finishing. Right: exposure site and the garden of the IETcc to study the effect of the climate into the corrosion of several concrete elements.

conversion of units. Thus, Fig. 7 shows the agreement of values from the electrochemical results and the gravimetric ones [6]. Only in the passive state when the corrosion is very small, is found a lack of agreement because the weight loss is not so accurate as can be the Linear Polarization technique.

During the 1990s, enormous advances were made in basic knowledge, among which the possibility of in situ measurement of the corrosion rate with the development of a portable corrosion-rate-meter (GECOR) (Fig. 7 right) made possible with the funds of a Eureka project and the company GEOCISA with the collaboration of Feliu and Gonzalez from the CENIM. The device quantifies the corrosion rate of large structures through the confinement of the current that otherwise sprays out of the border of the auxiliary electrode to an unknown distance. If the area polarized by the current is unknown, the corrosion rate cannot be quantified. The corrosion-rate-meter confines the applied current and then the area is that below the probe of the equipment [39], Fig. 8. Figure 9 shows values of the instantaneous corrosion rate (I_{corr}) and its integration as "accumulated corrosion" (P_{corr}).

In those years, RILEM established several committees, both on measurement techniques (TC-154) [40–43], and on models based on the diffusion of chlorides and carbonation (TC-178 and TC-213). In this regard it is worth mentioning the contribution of D. Whiting proposing in the 80s to reduce the duration of the test of resistance to chlorides [25] by applying a potential difference to concrete. These works gave rise to an intense debate [44] that allowed to develop the theoretical basis for the diffusion of chlorides and their migration through electric fields, which have subsequently led to the profusion of numerical models on service life of concrete based in accelerated testing methods.

4. From 2000 to the present: modeling and probabilistic treatment. Prevention and Repair techniques

The matters to remark in these almost two decades have being based in the work carried out in the CONTECVET project [45] in the decade of the 90s in which it is proposed how to calculate the residual structural capacity when the structures are corroded [47]. That is how to link the materials characteristics or models with the structural performance. Also a step forward in the decade of the 2000s has been the work in the European project DURACRETE [46] that has resulted in the incorporation of the Model Code 2010 [48] of fib of the probabilistic treatment of durability, in which the models of service life were fed with assumed values in order to create the framework of limit states theories.

Another area experimenting an important advance has been that related to preventive and repair methods. Researchers, engineers and companies have made a huge effort to give solutions for the growing number of structures that have had to be repaired. The companies have developed ad-hoc materials and techniques and the researchers have focused in giving solutions and standards for the longer durability of concrete in aggressive environments. Particular effort has been made in Latinoamerica with the above mentioned Manuals from the Network DURAR [36], REHABILITAR [37] and PREVENIR [38]. Also in Lati-

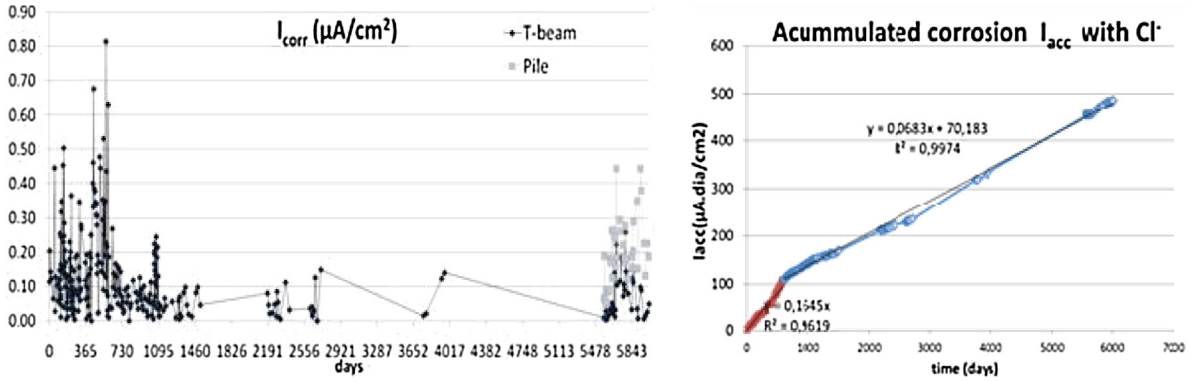

Figure 9. Variation of the corrosion rate of a beam of previous figure. Left instantaneous corrosión rate and right the accumulated corrosion calculated from the integration of the left curve at each time.

noamerica is quite relevant role played by researchers as O. Rincon, P. Helene, P. Castro, E. Pazini, A. Nepumoceno and A. Torres-Acosta and Alberto Sagúes in Tampa-Florida. They have contributed to the understanding of:

- The impact of tropical climate on the reinforcement durability
- The structural consequences of corrosion
- Chlorides models or how epoxi-coated rebars corrode
- The application of cathodic protection
- Repair systems and techniques

In spite of all efforts made until present however, in the 21st century, the corrosion of the reinforcement is still one of the areas that constantly attracts research interest. There are many aspects to be clarified, especially in the effectiveness of repairs and in the calibration of the life models.

Acknowledgements

Numerous colleagues and students have been behind the work here summarized. My thanks to all of them. Particularly inspiring has been the work of members of Rilem committees, Latinoamerican Networks and at present, of fib Committees. Corrosion science progress is mainly based on their work.

References

[1] J. Calleja, Corrosion de armaduras en hormigones armados y pretensados" (Reinforcement corrosión in reinforced and prestressed concretes) – Informes de la Construcción n° 180, May 1966.
[2] C. Andrade, Aportación a la corrosión de armaduras en el hormigón armado (Contribution to the corrosion of reinforcement in reinforced concrete), Master Thesis, University "Complutense" of Madrid, 1970.
[3] C. Andrade, New electrochemical technique for measurement of reinforcement corrosion in reinforced and prestressed concretes. Use of inhibitor admixtures as protection method, Doctoral Thesis, Complutense University of Madrid, June 1973.
[4] F. Mansfeld, K.B. Oldham, Modification of the Stern-Geary linear polarization equation Corrosion Science, vol. 11, Pergamon Press, 1971, pp. 787–796.
[5] M.E. Indig, C. Groot, Some limitationsof the linear polarization techniquesin evaluating corrosión behaviour, Corrosion (1969) 445.
[6] C. Andrade, J.A. Gónzalez, -Quantitative measurements of corrosion rate of reinforcing steels embedded in concrete using polarization resistance measurements-, Werkst. Korros. 29 (1978) 515.
[7] J.A. González, S. Algaba, C. Andrade, Corrosion of reinforcing bars in carbonated concrete, Br. Corros. J. 3 (1980) 135–139.
[8] M. Stern, A method for determining corrosión rates from linear polarization data, Corrosion 14 (1958) 400.
[9] M. Rosello, M. Elices, G.V. Guinea, Fracture of model concrete: 2. Fracture energy and characteristic length, Cem. Concr. Res. 36 (2006) 1345–1353.
[10] A. Valiente, M. Elices, Premature failure of prestressed steel bars Engineering Failure Analysis, vol. 5, no. 3, 1998, pp. 219–227.
[11] M.A. Astiz, An incompatible singular elastic element for two- and three-dimensional crack problems, Int. J. Fract. 31 (1986) 105–124.
[12] M. Elices, L. Caballero, A. Valiente, J. Ruiz, A. Martín, Hydrogen embrittlement of steels for prestressing concrete: the FIP and DIBt tests, Corrosion 64 (2) (2008) 164–174.
[13] M. Elices, A. Valiente, L. Caballero, M. Ioardaneschu, Fullea, J. Sanchez-Montero, V. Lopez, Failure analysis of prestressed anchor bars, Eng. Failure Anal. 24 (2012) 57–66A.
[14] V.K. Gouda, G.E. Monfore, A rapid method for studying corrosion inhibiton of steel in concrete, J. PCA 3 (Septiembre 1965) 24.
[15] R.F. Stratfull, Effect of reinforced concrete in ClNa and SO_4Na_2 environments, Mater. Protect. Dic. (1964) 75.
[16] H. Kaesche, testing corrosion danger of steel reinforcement due to admixtures in concrete, Zement-Kalk-Gips 7 (1959) 289.
[17] A. Baumel, The effect of additives on the corrosion behaviour of steel in concerte, Zement-Kalk-Gips 7 (1959) 294.
[18] R. Cigna, M. Maraghini, G. Schippa, Effeto del contenuto di Ca_2Cl sul cmportamento dei ferri affogati in malte cementizie, L'Industria italiana del Cemento Marzo (1966) 139.
[19] D.A. Hausmann, Electrochemical behaviour of steel in concrete, J. A.C.I. Febr. (1964) 171.
[20] D.A. Hausmann, A probability model for steel corrosion in concrete, Mater. Perform. 37 (10) (1996) 64–68.
[21] C.L. Page, K.W.J. Treadaway, Aspects of the electrochemistry of steel in concrete, Narute 297 (5862) (1982) 109–115.
[22] M. Collepardi, A. Marcialis, R. Turriziani, The Kinects of chloride ion penetration in concrete (in italian), I1 Cemento 67 (1970) 157–164.
[23] O. Gjorv, O. Vennesland, A. El-Susaidy, Mater. Perform. (1986) 39–44.
[24] A.A. Sagüés, R.G. Powers, R. Kessler, Corrosion Performance of Epoxy-Coated Rebar in Florida Keys Bridges, CORROSION/2001, paper no. 01642, NACE International, Houston, TX, 2001.
[25] D. Whiting, "Rapid determination of the chloride permeability of concrete", in: Federal Highway Administration – Report FHWA/RD-81/119, 1981.
[26] N.S. Berke, A review of corrosion inhibitors, in: Environmental Treatment and Control, October, 1989, pp. 41–44.
[27] P. Bamforth, J. Chapman-Andrews, Long term performance of RC elements under U.K. coastal exposure conditions, in: N. Swamy (Ed.), International

Conference on Corrosion and Corrosion Protection of Steel in Concrete, Sheffield Academic Press, 1994, pp. 139–156.
[28] L. Lazzari, P. Pedeferri, Cathodic Protection – Polipress, Politecnico de Milano Publications, 2006.
[29] G.K. Glass, N.R. Buenfeld, The presentation of the chloride threshold level for corrosion of steel in concrete, Corros. Sci. 39 (5) (1997) 1001–1013.
[30] J. Kropp., Relations between transport characteristics and durability, in: J. Kropp, H.K. Hilsdorf (Eds.), Performance Criteria for Concrete Durability, E&FN SPON, 1995, Results of Rilem TC 116.
[31] U. Nurnberger, Analysis and evaluation of failures in prestressed steel, in: Proceedings of the Third FIP Symposium, FIP-Berkeley, Wexham Springs, Slough, UK, 1981.
[32] A. Macías, C. Andrade, Corrosion rate of galvanized steel immersed in saturated solution of $Ca(OH)_2$ in the pH range 12–13·8, Br. Corros. J. (UK) 18 (2) (1983) 82–87.
[33] C. Andrade, C. Alonso, J.A. González, Some laboratory experiments on the inhibitor effect of $NaNO_2$ on reinforcement corrosion – cement, concrete, aggregates, ASTM 8 (2) (1986) 110–116.
[34] K. Tuutti, Corrosion of Steel in Concrete, n° 4-82, Swedish Cement and Concrete Institute (CBI), Stockholm, 1982.
[35] P. Schiessl, Corrosion of steel in concrete, in: Report of RILEM TC 60-CSC, Chapman and Hall, London, 1988.
[36] Manual DURAR Manual de Inspección, Evaluación y Diagnóstico de Corrosión en Estructuras de Hormigón Armado- O. de Rincón Editora. 2002.
[37] Manual REHABILITAR Manual de rehabilitacion de estructuras de hormigon reparacion refuerzo- Helene P. Pereira F. Editores 2003.
[38] Manual PREVENIR. http://www.alconpat.org/contenido/libros.php.
[39] S. Feliú, J.A. González, S. Feliú Jr., C. Andrade, Confinement of the electrical signal or in-situ measurement of Polarization Resistance in Reinforced concrete, ACI Mater. J. 87 (1990) 457.
[40] B. Elsener, C. Andrade, J. Gulikers, R. Polder, M. Raupach, R ILEM TC 154-EMC: Electrochemical Techniques for Measuring Metallic Corrosion Half-Cell Potential Measurements – Potential Mapping on Reinforced Concrete Structures, vol. 36, 2003, pp. 461–471.
[41] R. Polder, C. Andrade, B. Elsener, O. Vennesland, J. Gulikers, R. Weidert, M. Raupach, Test methods for on-site measurement of resistivity of concrete", RILEM TC 154-EMC: electrochemical techniques for measuring metallic corrosion, Mater. Struct. 33 (2000) 603–611.
[42] C. Andrade, C. Alonso, J. Gulikers, R. Polder, R. Cigna, Ø. Vennesland, M. Salta, A. Raharinaivo, B. Elsener, RILEM TC 154-EMC: Electrochemical Techniques for Measuring Metallic Corrosion Recommendations Test methods for on-site corrosion rate measurement of steel reinforcement in concrete by means of the polarization resistance method, Mater. Struct. 37 (273) (2004) 623–643.
[43] Ø. Vennesland, M. Raupach, C. Andrade, Recommendation of Rilem TC 154-EMC: "Electrochemical techniques for measuring corrosion in concrete – measurements with embedded probes, Mater. Struct. 40 (2007) 745–758.
[44] C. Andrade, -Calculation of chloride diffusion-coefficients in concrete from ionic migration measurements, Cem. Concr. Res. 23 (3) (1993) 724–742.
[45] CONTECVET – A Validated User's Manual for Assessing the Residual Life of Concrete Structures, DG Enterprise, CEC, 2001 (The manual can be downloaded from the web site of http://www.ietcc.csic.es/index.php/es/publicaciones-2/manual-contecvet).
[46] DURACRETE. Probabilistic performance based on durability design of concrete structures. EU-Brite EuRam Project BE95-1347. A number of reports available from CUR Centre for Civil Engineering Research and Codes, Gouda, The Netherlands. 1999.
[47] J. Rodriguez, L.M. Ortega, J. Casal, Load carrying capacity of concrete structures with corroded reinforcement, in: M.C. Forde (Ed.), International Conference on Structural Faults & Repairs, London, UK, vol. 2, 1995, pp. 189–198.
[48] Model Code 2010. fib (2012).

Available online at
ScienceDirect
www.sciencedirect.com
Hormigón y Acero 2019; 69(S1):29–34
www.e-ache.com
www.elsevierciencia.com/hya

From experiments to design: A probabilistic definition of design formulations from empirical and semi-empirical resistance models

Desde experimentos hasta diseño: una definición probabilística de formulaciones de diseño a partir de modelos de resistencia empíricos y semiempíricos

Giuseppe Mancini *, Vincenzo Ilario Carbone, Diego Gino

Department of Structural, Geotechnical and Building Engineering (DISEG), Politecnico di Torino, Turin, Italy

Received 30 September 2017; accepted 26 December 2017
Available online 24 March 2018

Abstract

The definition of design equations from empirical or semi-empirical resistance models is a matter of relevance for structural engineering. In common practice, the limit states design approach predicts the direct application of partial safety factors to the resistance of the materials in order to obtain design formulations coherent with a prescribed level of reliability. As empirical or semi-empirical models are calibrated, adjusting empirical coefficients to fit a set of experimental data, the application of partial safety factors to material properties alone is not able to provide a correct estimation of structural reliability.

In the present paper, a methodology based on the Monte Carlo method for probabilistic calibration of empirical and semi-empirical resistance models is proposed. Its application related to the probabilistic calibration of the semi-empirical model proposed by *fib* Model Code 2010 for the estimation of laps and anchorages tensile strength in reinforced concrete structures is reported and discussed.

Keywords: Structural reliability; Empirical and semi-empirical models; Model uncertainties; Probabilistic calibration; Laps and anchorages

Resumen

La definición de las ecuaciones de proyecto a partir de modelos resistencia empírica o semiempírica es una cuestión de importancia para la ingeniería estructural. En la práctica común, el proyecto segun los estados límites prevee la aplicación directa de factores de seguridad parciales a la resistencia de los materiales, con el fin de obtener formulaciones de diseño coherentes con un nivel de fiabilidad prescrito. Como los modelos empíricos o semiempíricos se calibran ajustando los coeficientes empíricos para adaptarse a un conjunto de datos experimentales, la aplicación de factores de seguridad parciales a las propiedades de los materiales por sí sola no permite una estimación correcta de la fiabilidad estructural.

En el presente trabajo se propone una metodología basada en el método de Monte Carlo para la calibración probabilística de modelos de resistencia empírica y semiempírica. Su aplicación relacionada con la calibración probabilística del modelo semiempírico para la estimación de la resistencia a tracción de superposiciones y anclajes en estructuras de hormigón armado es reportada y comentada.

Palabras clave: Fiabilidad estructural; Modelos empíricos y semiempíricos; Incertidumbres del modelo; Calibración probabilística; Vueltas y anclajes

* Corresponding author.
E-mail address: giuseppe.mancini@polito.it (G. Mancini).

https://doi.org/10.1016/j.hya.2017.12.003

1. Introduction

Commonly, in structural engineering design formulations must always comply with a prescribed reliability level. To this end, physical or empirical and semi-empirical resisting models should be properly calibrated by the application of consistent safety formats.

The resisting models based both on physical laws (e.g. equilibrium of forces and kinematic compatibility) and on semi-empirical or empirical formulations (e.g. [1,2]) fitted on experimental results are really frequent in structural engineering.

In the limit states semi-probabilistic design approach [3], the safety requirements are fulfilled applying partial safety factors accounting for material properties and geometry statistical variability and model uncertainties. Concerning the resisting models based on physical assumptions, the direct application of partial factors to materials strength leads to design expressions consistent with a specific reliability level. This does not happen in the case of empirical or semi-empirical resisting models that are based on experimental test set. In such kind of models, all the empirical coefficients embedded in the formulation are calibrated as best fitting on the experimental results and assuming mean values of material properties (i.e. the actual values measured during the experiment execution). In this case, it implies that the direct application of partial safety factors to materials strength does not lead to a proper evaluation of reliability.

In the literature, several methodologies for probabilistic assessment of physical, empirical and semi-empirical models are proposed [4–6]. In order to apply these theoretical procedures consistently, an accurate assessment of model uncertainties is necessary as proposed in [7–11].

However, a general and ease-to-apply procedure able to calibrate empirical or semi-empirical formulation in relation to a specific level of reliability is still not available and defined.

In the present paper a methodology based on the Monte Carlo method [12] for calibration of empirical and semi-empirical resisting models is proposed. This procedure is able to account for both statistical variability of material and geometric properties and the influence of the resisting model uncertainties. After the detailed description of the methodology, its application to the calibration of the semi-empirical model for laps and anchorages tensile strength evaluation suggested by Model Code 2010 [13] is proposed and commented.

2. Methodology for the assessment of design expressions from empirical or semi-empirical resisting models

In this section the methodological approach for probabilistic calibration of empirical and semi-empirical models is described.

The proposed methodology grounds on four main points:

- the individuation of the empirical or semi-empirical resisting model;
- the definition of the probabilistic model;
- the definition and characterization of the resistance random variable;
- the estimation of the fractiles of the resistance random variable and determination of the design expressions.

2.1. Individuation of the empirical or semi-empirical resisting model

In general, an empirical or semi-empirical resting model is calibrated grounding on a set of experimental results and the estimated value of the resistance R_{model} can be expressed in the following form:

$$R_{\text{model}} = C \cdot f(X_{1,m}, X_{2,m}, \ldots, X_{i,m}, \ldots, X_{K,m}) \cdot A, \quad i = 1, 2, \ldots, K \tag{1}$$

where C is best fitting empirical coefficient calibrated on the experimental database; X_i is a set of K random variables which plays a significant role in the resisting model ($i = 1, 2, \ldots, K$); $f(X_{1,m}, X_{2,m}, \ldots, X_{i,m}, \ldots, X_{K,m})$ is a function of the abovementioned random variables assumed with their mean or experimental value; A is a function of all the parameters that can be assumed as deterministic (e.g. geometry).

The value of R_{model} estimated by means of Eq. (1) should be intended as a mean resistance as it is calculated assumed mean or experimental material properties and empirical coefficients fitted on experimental tests. Then, the direct application of Eq. (1) for design purposes it is not correct as it is deprives of any safety assumption.

2.2. Definition of the probabilistic model

Once all the parameters that can influence the resisting model with their statistical variability are selected, the following vector of random variables X can be defined:

$$X = (X_1, X_2, \ldots, X_i, \ldots, X_K, \vartheta), \quad i = 1, 2, \ldots, K \tag{2}$$

The vector of random variables X includes also the model uncertainty random variable ϑ that should be calibrated base on the statistical assessment of the ratio between experimental results and model predictions according to [14]. The vector of random variables X can group both statistically independent and statistically dependent random variables.

All the random variables grouped in X have to be represented by their probabilistic distribution (i.e. PDFs and/or CDFs) which must be able to describe their statistical variability accurately.

Suggestions for the definition of the probabilistic model can be acknowledged by [14].

2.3. Definition of the resistance random variable

The resistance random variable can be evaluated in function of the vector X descending from Eq. (1) as follow:

$$R(X) = \vartheta \cdot C \cdot f(X) \cdot A \tag{3}$$

The expression reported by Eq. (3) is able to represent the random variability of the resistance accounting for material sta-

tistical fluctuations and model uncertainties. However, in order to propose a not case dependent and general procedure, the following ratio has to be addressed:

$$\zeta(X) = \frac{R(X)}{C \cdot f(X_{1,\text{rep}}, X_{2,rep}, \ldots, X_{i,\text{rep}}, \ldots, X_{K,\text{rep}}) \cdot A} \quad i = 1, 2, \ldots, K \tag{4}$$

where $\zeta(X)$ is the resistance ratio random variable and ($X_{1,\text{rep}}$, $X_{2,\text{rep}}$, …, $X_{i,\text{rep}}$, …, $X_{K,\text{rep}}$) are the representative values of the main random variables (e.g. 5% characteristic or nominal value).

The random variable $\zeta(X)$ can be assessed by means of the Monte Carlo method [11] sampling from the probabilistic distributions of the random variables involved by Eq. (4). When a significant number of samples of the population of $\zeta(X)$ is available, the most suitable probabilistic distribution able to describe ζ can be selected.

2.4. Estimation of fractiles of the resistance random variable

In order to define relationships for design purposes, it is convenient to assess particular fractiles from the resistance random variable.

This can be performed defining the following probability:

$$P(\zeta(X) \leq \zeta_p) = p \tag{5}$$

where ζ_p is the fractile related to a certain probability to not be exceeded of the random variable $\zeta(X)$; p represent the probability of not exceedance for the value of ζ_p.

In common engineering practice and according to international codes [15,13], the following fractiles of $\zeta(X)$ are estimated:

- characteristic value ζ_k, setting $p = 0.05$;
- design value ζ_d, setting $p = \Phi(-\alpha_R \cdot \beta)$;

with β reliability index [16], α_R first order reliability method (FORM) correction factor (assumed equal to 0.8 for dominant resistance variables) [13] and $\Phi(\cdot)$ cumulative standard normal distribution.

Once the probabilistic coefficient ζ_p has been estimated, the general formulation for the selected fractile of the resistance random variable R_p can be expressed as follow:

$$R_p = \zeta_p \cdot C \cdot f(X_{1,\text{rep}}, X_{2,rep}, \ldots, X_{i,\text{rep}}, \ldots, X_{K,\text{rep}}) \cdot A \quad i = 1, 2, \ldots, K \tag{6}$$

3. Application example: laps and anchorages tensile strength in *fib* Model Code 2010

In this section, an example of application of the procedure so far described is reported. Usually, in reinforced concrete structures, due to technical and construction reasons, it is required to interrupt the longitudinal tensile steel reinforcements. It is then necessary to provide an adequate length of overlapping or anchorage in order to allow continuity in the transferring of forces within the structure.

In [13,17] the evaluation of the maximum tensile strength of a lapped joint or anchorage can be assessed by means of a semi-empirical formulation. Subsequently, the proposed methodology will be applied for the calibration of the abovementioned resisting model.

3.1. Laps and anchorages tensile strength formulation in Model Code 2010

In the *fib* Model Code 2010 [13] the evaluation of laps and anchorages tensile strength f_{stm} is performed by means of the semi-empirical model proposed in [17], that is a modification of the approach suggested in [18] based on [19,20].

The best-fitting semi-empirical expression for laps and anchorages strength estimation, which is calibrated on a large set experimental results [21], is represented by Eq. (7):

$$f_{stm} = 54 \cdot \left(\frac{f_{cm}}{25}\right)^{0.25} \left(\frac{l_b}{\Phi}\right)^{0.55} \left(\frac{25}{\Phi}\right)^{0.2} \left[\left(\frac{c_{\min}}{\Phi}\right)^{0.25} \left(\frac{c_{\max}}{c_{\min}}\right)^{0.1} + k_m K_{tr}\right] \tag{7}$$

where f_{cm} is the mean concrete compressive strength; l_b is the lap/anchorage length; Φ is the bar diameter; concrete covers $c_{\min}$, $c_{\max}$ and effectiveness coefficient k_m are evaluated according to Fig. 1(a and b).

The coefficient K_{tr} accounts for the effect of confinement provided by shear links/stirrups situated along the lap or anchorage and can be calculated as follow:

$$K_{tr} = \frac{n_l n_g A_{sv}}{(l_b \Phi n_b)} \tag{8}$$

where n_l is the number of legs of a link/stirrup; n_g is the number of groups of links/stirrups; A_{sv} is the transverse area of each leg of a link/stirrup; n_b is the number of individual anchored bars of pairs of lapped bars.

The assessment of Eq. (7) have been performed base on an experimental database counting more than 800 tests on laps and anchorages coming from American (ACI) and European investigations [21]. In the *fib* Bulletin No. 72 [17] are provided the following limits for Eq. (7) as they represent also the limits of the abovementioned database:

- $15\,\text{MPa} \leq f_{cm} \leq 110\,\text{MPa}$;
- $K_{tr} \leq 0.05$;
- $0.5 \leq c_{\min}/\Phi \leq 3.5$ and $c_{\max}/c_{\min} \leq 5$;
- $l_b \geq 10\Phi$;
- $25/\Phi \geq 2$.

3.2. Probabilistic model

As reported in Section 2, a set of relevant random variables have to be defined. These random variables have to

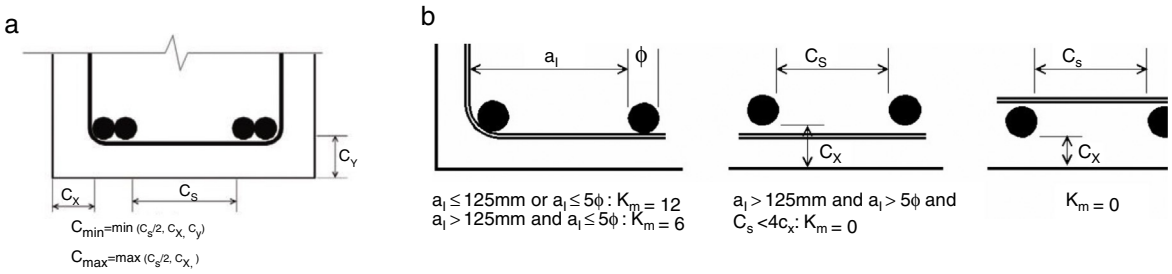

Figure 1. Determination of concrete cover c_{min} and c_{max} in Eq. (1) (a) and assessment of the effectiveness of shear links (b).

Table 1
Statistical parameters and probabilistic distribution for the random variables affecting the resisting model.

	Ref.	Mean value	C.o.V	Type of distribution
Concrete compressive strength, f_c [MPa]	[13]	f_{cm}	0.15	Log-normal
Model uncertainties, ϑ [–]	[22]	0.98	0.13	Log-normal

represent parameters that are explicitly considered into the resisting model.

In this case, may be reasonable consider as random variable only the concrete compressive strength, which strongly affect the resisting mechanism with its statistical variability. At the purpose of this example all the other parameters involved by Eq. (7) can be assumed as deterministic.

However, the resisting models shows an intrinsic uncertainty due to simplified assumptions in their definition and in disregarding parameters that can have some influence on the actual resisting mechanism. This involves that the resisting model uncertainties have to be accurately addressed and included into the probabilistic model.

Therefore, in the present application the following random variables will be considered in the vector X:

$$X = (f_c, \vartheta) \tag{9}$$

where:

- f_c, is the cylinder compressive strength random variable. According to *fib* Model Code 2010 [13] the statistical variability of f_c can be described by means of a log-normal distribution with coefficient of variation V_c equal to 0.15 and mean value equal to f_{cm} depending by the concrete strength class (Table 1).
- ϑ, is the resisting model uncertainty random variable. In compliance with JCSS Probabilistic Model Code [14] the statistical characterization of ϑ can be performed defining the following ratio:

$$\vartheta = \frac{R_{\text{Exp}}}{R_{\text{Model}}} \tag{10}$$

where R_{Exp} is the actual resistance estimated from laboratory tests and R_{Model} is the resistance estimated by the model.

The model uncertainties related to Eq. (7) have been estimated base on the database of experimental results reported in [21]. The mean value μ_ϑ and the coefficient of variation V_ϑ are listed in Table 1 according to the statistical investigation proposed by [22] concerning the case of new structures. According both with [22,14] ϑ can be described by means of a log-normal distribution.

3.3. Resistance random variable

Defining the resistance random variable R as the lap or anchorage tensile strength f_{st}, according with Section 2, Eq. (7) can be rewritten as follow:

$$R(X) = \vartheta \cdot C \cdot f_c^{0.25} \cdot A \tag{11}$$

with:

$$A = \left(\frac{1}{25}\right)^{0.25} \left(\frac{l_b}{\Phi}\right)^{0.55} \left(\frac{25}{\Phi}\right)^{0.2} \left[\left(\frac{c_{\min}}{\Phi}\right)^{0.25} \left(\frac{c_{\max}}{c_{\min}}\right)^{0.1} + k_m K_{tr}\right] \tag{12}$$

and the empirical coefficient C set equal to 54.

Defining as the representative value for concrete compressive strength the characteristic one, the resistance ratio random variable $\zeta(X)$ can be determined as subsequently reported:

$$\zeta(X) = \frac{\vartheta \cdot C \cdot f_c^{0.25} \cdot A}{C \cdot f_{ck}^{0.25} \cdot A} = \frac{\vartheta \cdot f_c^{0.25}}{f_{ck}^{0.25}} \tag{13}$$

where f_{ck} is the 5% characteristic value for cylinder concrete compressive strength.

By means of Monte Carlo technique it is possible to generate a large sample of the population of the random variable $\zeta(X)$.

In the present example a number of samples N equal to 10^4, 10^6 and 10^8 has been generated adopting the direct Monte Carlo sampling from the probabilistic distributions of the basic variables listed in Table 1. The associated relative frequency histogram is reported in Fig. 2.

As $R(X)$ is a function of two log-normally distributed random variables (i.e. f_c and ϑ), it is expected that $\zeta(X)$ is log-normally distributed too [4].

A shown by Fig. 2, the results obtained adopting 10^4, 10^6 and 10^8 samples give not appreciable difference in the estimation of the distribution parameters for the random variable $\zeta(X)$. Being the total number of samples required for the Monte Carlo simulation inversely proportional to the probability of failure to

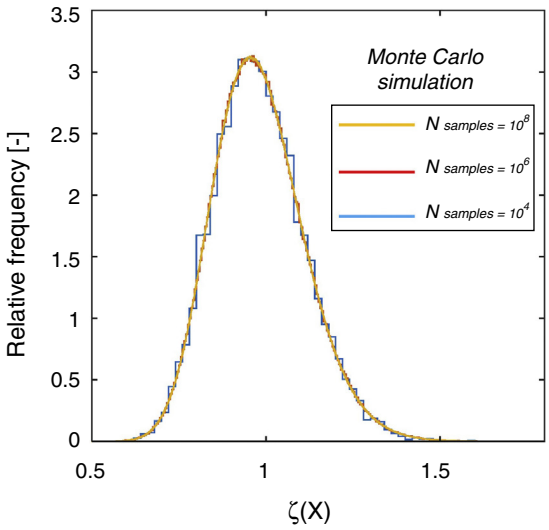

Figure 2. Relative frequency histogram for the Monte Carlo simulation of the random variable $\zeta(X)$ in the hypothesis of 10^4, 10^6 and 10^8 samples.

be estimated, a number of samples set $N = 10^6$ can be considered sufficient for the present investigation (as, in Section 3.4, the minimum estimated probability is around 10^{-3}, which corresponds to the fractile of the distribution of $\zeta(X)$ associated to the value of the product $\alpha_R \cdot \beta$ with $\beta = 3.8$ and $\alpha_R = 0.8$).

However, in the case of the estimation of smaller probability of failure, a larger number of samples is recommended in order to represent, inside the sample, also lower extreme values of the involved random variables.

Finally, concerning the population with 10^6 samples of the random variable $\zeta(X)$, the Chi-square goodness of fit test with 5% level of significance testing the hypothesis of normality of the sample of $\ln(\zeta(X))$ have been performed confirming the hypothesis of log-normality of the variable $\zeta(X)$. Hence, the resistance ratio random variable $\zeta(X)$ can be described by means of a lognormal distribution having mean value equal to 0.98 and coefficient of variation (C.o.V) equal to 0.13 (Fig. 3(a and b)).

Table 2
Comparison between the proposed method based on Monte Carlo simulation with $N = 10^6$ samples and the analytical method proposed by [4].

	Proposed $N = 10^6$	[4,22]
ζ_k [–]	0.78	0.83
ζ_d [–] ($\alpha_R = 0.8$; $\beta = 3.8$)	0.65	0.69

3.4. Derivation of the characteristic and design expressions

Once the probabilistic distribution for the random variable $\zeta(X)$ has been determined and characterized, it is possible to calculate its fractiles as described by Eq. (5). In Table 2 are reported the 5% characteristic value ζ_k and design value ζ_d (assuming the reliability index $\beta = 3.8$ as in the case of ordinary structures with 50 years service life [13,15]. The abovementioned values have been compared in Table 2 with the results coming from the simplified analytical procedure proposed by Taerwe [4] (which was applied in [22] to Eq. (7)) valid in the case of log-normally distributed random variables.

The simplified analytical method [4,22] leads to results close to the ones obtained with the simulation technique. However, the proposed methodology can be easily applied in case of probabilistic distributions for main random variables different from the log-normal one.

As international codes [3,13,23] suggests different levels of reliability distinguishing between new or existing structures in function of the service life of the structure, it is useful to define the trend of variation of the design probabilistic coefficient ζ_d versus the reliability index β. The variation of ζ_d in function of the reliability index β in proposed in Fig. 4. The calibration of the design expressions related to original semi-empirical model (Eq. (7)) can be performed specifically in function of the target reliability level.

Finally, the 5% characteristic $f_{st,k}$ and the reliability-based design $f_{st,d}$ expressions for the semi-empirical model proposed by [17,13] for laps and anchorages tensile strength estimation

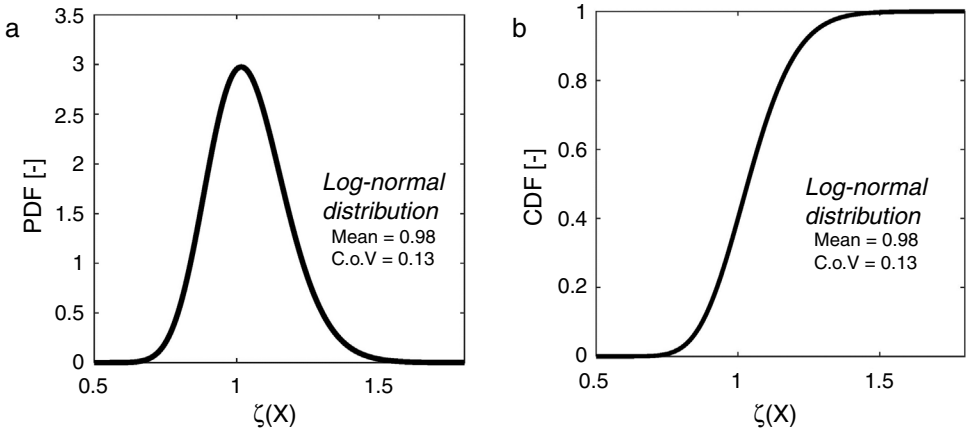

Figure 3. Log-normal distribution (PDF (a) and CDF (b)) for the random variable $\zeta(X)$.

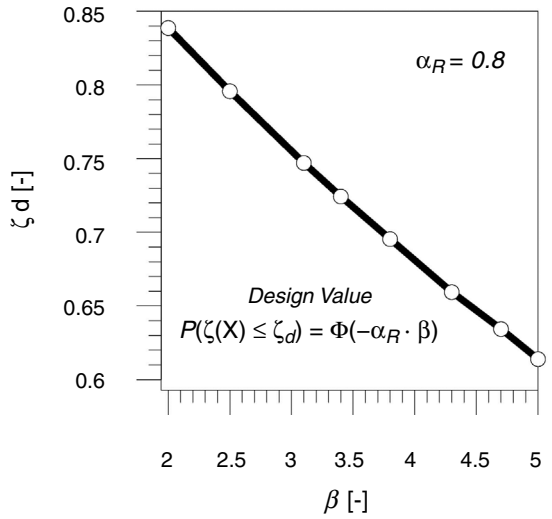

Figure 4. Variation of the design probabilistic coefficient ζ_d in the function of the reliability index β.

can be evaluated as follow according to Eq. (6) and Table 2:

$$f_{st,k} = 42 \cdot \left(\frac{f_{ck}}{25}\right)^{0.25} \left(\frac{l_b}{\Phi}\right)^{0.55} \left(\frac{25}{\Phi}\right)^{0.2} \left[\left(\frac{c_{\min}}{\Phi}\right)^{0.25} \left(\frac{c_{\max}}{c_{\min}}\right)^{0.1} + k_m K_{tr}\right] \quad (14)$$

$$f_{st,d} = 35 \cdot \left(\frac{f_{ck}}{25}\right)^{0.25} \left(\frac{l_b}{\Phi}\right)^{0.55} \left(\frac{25}{\Phi}\right)^{0.2} \left[\left(\frac{c_{\min}}{\Phi}\right)^{0.25} \left(\frac{c_{\max}}{c_{\min}}\right)^{0.1} + k_m K_{tr}\right] \quad \alpha_R = 0.8; \quad \beta = 3.8 \quad (15)$$

4. Conclusions

A probabilistic procedure based on the Monte Carlo method for the derivation of design formulas by empirical or semi-empirical resisting models has been proposed. The procedure allows the correct evaluation of the influence of material and resisting model uncertainties in the reliability-based calibration of the abovementioned kinds of resisting models.

This result can be obtained by means of the definition of multiplicative probabilistic coefficients ζ_p, which are related to a specific probability of not exceedance p. As the probability p is directly related to a certain value of the reliability index β, the final design equations can be derived in function of the level of reliability required by the codes.

The proposed procedure is very general as it is independent from the probabilistic model defined for the main random variables. Furtherly, it is suitable for the calibration of design formulations both in the case of serviceability and ultimate limit states.

Acknowledgements

This work is part of the collaborative activity developed by the authors within the framework of Task Group TG 3.1 of the Fédération Internationale du Béton (*fib*).

References

[1] A. Muttoni, M.F. Ruiz, Shear strength of members without transverse reinforcements as function of critical shear crack width, ACI Struct. J. 219 (2008) 163–172.
[2] G. Bertagnoli, G. Mancini, Failure analysis of hollow core slabs tested in shear, Struct. Concr. 10 (2009) 139–152, N° 3.
[3] EN 1990 Eurocode: Basis of Structural Design, Brussels, 2002.
[4] R.L. Taerwe, Toward a consistent treatment of model uncertainties in reliability formats for concrete structures, CEB Bull. d'Information (1993) 5–34, N° 105-S17.
[5] S. Junho, K. Won-Hee, Probabilistic shear strength models for reinforced concrete beams without shear reinforcements, Struct. Eng. Mech. 34 (1) (2016) 15–38.
[6] R.L. Taerwe, Partial safety factor for high strength concrete under compression, in: Proceedings of High Strength Concrete 1993, 1993, pp. 385–392.
[7] G. Köenig, J. Fischer, Model uncertainties concerning design equations for the shear capacity of concrete members without shear reinforcement, CEB Bull. d'Information (1995) 49–94, N° 224.
[8] C.H. McLeod, C. Viljoen, J.V. Retief, Quantification of model uncertainty of EN1992 crack width prediction model, in: Insights and Innovations in Structural Engineering, Mechanics and Computation, 2016, pp. 1349–1354.
[9] M. Sikora, M. Holicky, M. Prieto, P. Tanner, Uncertainties in resistance models for sound and corrosion-damaged RC structures according to EN 1992-1-1, Mater. Struct. (2014) 3415–3430, N° 48.
[10] D.L. Allaix, V.I. Carbone, G. Mancini, Modelling uncertainties for load-bearing capacity of corroded simply supported RC beams, Struct. Concr. (2015) 333–341, N° 3.
[11] D. Gino, G. Bertagnoli, D. La Mazza, G. Mancini, A quantification of model uncertainties in NLFEA of R.C. shear walls subjected to repeated loading, *Ingegneria sismica*, International Journal of Earthquake Engineering (2017) 79–91, Anno XXXIV, Special issue.
[12] M.H. Kalos, P.A. Whitlock, Monte Carlo Methods, Vol. 1: Basics, John Wiley & Sons, 1986.
[13] *fib*: *fib* Model Code for Concrete Structures 2010, Lausanne, 2013.
[14] JCSS, JCSS Probabilistic Model Code, 2006.
[15] CEN: EN 1992-1-1: Eurocode 2 – Design of Concrete Structures. Part 1-1: General Rules and Rules for Buildings, CEN, Brussels, 2004.
[16] A.M. Hasofer, N.C. Lind, Exact and invariant second moment code format, J. Eng. Mech. Div. ASCE 100 (EM1) (1974) 111–121.
[17] *fib* Bulletin N°72: Bond and Anchorages of Embedded Reinforcements – Background to the *fib* Model Code for Concrete Structures, Lausanne, 2015.
[18] E. Canbay, R.J. Frosch, Bond strength of lap-spliced bars, ACI Struct. J. 102 (4) (2005) 605–614.
[19] S. Lettow, Ein Verbundelement für nichtlineare Finite Element Analysen – Anwendung auf Übergreifungsstöße (Bond Element for Nonlinear Finite Element Analysis – Application to Lapped Splices) (Dissertation), University of Stuttgart, 2006.
[20] C.J. Burkhardt, Zum Tragverhalten von Übergreifungsstößen in hochfestem Beton (Behavior of Lapped Splices in High Strength Concrete) (Dissertation), RWTH, Aachen, 2000.
[21] *fib* TG 4.5 Bond Tests Database, 2005.
[22] G. Mancini, V.I. Carbone, G. Bertagnoli, D. Gino, Reliability-based evaluation of bond strength for tensed lapped joints and anchorages in new and existing reinforced concrete structures, Struct. Concr. (2017) 1–14, http://dx.doi.org/10.1002/suco.201700082.
[23] ISO 2394: General Principles on Reliability for Structures, Genéve, 1998.

Available online at
ScienceDirect
www.sciencedirect.com
Hormigón y Acero 2019; 69(S1):35–41
www.e-ache.com
www.elsevierciencia.com/hya

Progreso's viaduct in Yucatan, Mexico: First durable concrete structure in the world made with stainless steel

El viaducto de Progreso en Yucatán, México: primera estructura de concreto durable en el mundo construida con acero inoxidable

Andrés A. Torres-Acosta [a,*], Miguel Martínez-Madrid [b], Pedro Castro-Borges [c]

[a] *Instituto Mexicano del Transporte, Coordinación de Ingeniería Vehicular e Integridad Estructural, Investigador Titular, SNI II Km 12 Carretera Querétaro-Galindo, Mpio. Pedro Escobedo, Sanfandila, Querétaro, Mexico*
[b] *Instituto Mexicano del Transporte, Coordinación de Ingeniería Vehicular e Integridad Estructural, Coordinador, SNI I Km 12 Carretera Querétaro-Galindo, Mpio. Pedro Escobedo, Sanfandila, Querétaro, Mexico*
[c] *Centro de Investigación y de Estudios Avanzados del IPN Unidad Mérida, Investigador Titular 3D, SNI III, Km 6 Ant Carr, a Progreso, 97310 Mérida, Yucatán, Mexico*

Received 16 October 2017; accepted 25 May 2018
Available online 20 July 2018

Abstract

In 1935, the Danish company Christiani and Nielsen won the bidding for the design and construction of a viaduct/pier at Port Progreso, Mexico. The design is characterized by the use of stainless steel and massive concrete to the sub and superstructure. The project consisted of a series of arches supported on simple concrete pillars. It consists of three parts: 415 m access, 1752 m viaduct, and a 50 × 205 m pier. This engineering work is unique in the world for its technological importance by being the first to be designed and built with durability criteria. After being in service for more than 75 years, structural distresses were observed by surface crack appearance at the pile caps and arches, thus external CFRP strips were used as structural reinforcement to avoid collapse of the viaduct. Still, the structural distress continued, thus a new viaduct parallel to the actual was designed and built using durability criteria. This investigation explains the inspection results, CFRP external reinforcement installation, and the design/construction of the new viaduct using durability criteria.

Keywords: Durability; Stainless steel; Detailed inspection; Carbon fiber-reinforced polymer; Design

Resumen

En 1935, la compañía danesa Christiani & Nielsen ganó el concurso de la obra para el diseño y la construcción de un viaducto/muelle en el puerto de Progreso, México. El diseño se caracterizó por el uso de acero inoxidable y concreto masivo en la sub y superestructura. El proyecto consistió en una serie de arcos apoyados en pilares de concreto simple. Consistió en tres partes: acceso de 415 m, viaducto de 1,725 m y un muelle de 50 × 205 m. Esta obra de ingeniería es única en el mundo por sus avances tecnológicos siendo la primera que se sabe fue diseñada con criterios de durabilidad. Después de estar en servicio por más de 75 años, se han observado algunos problemas estructurales como la aparición de grietas en la superficie de algunos arcos y cabezales, es por ello que se planteó la necesidad de reforzar estos elementos con tiras de compuestos de fibra de carbono (CFRP, por sus siglas en inglés) externo, para evitar el colapso de esta estructura. A pesar de este refuerzo, los daños estructurales continuaron, por lo que se recurrió al diseño y construcción de un nuevo viaducto, que estuviera paralelo al primero. Esta investigación explica los resultados de las inspecciones llevadas al cabo, la instalación del refuerzo a base de CFRP y el diseño/construcción del nuevo viaducto en donde se usaron criterios de durabilidad.

Palabras clave: Durabilidad; Acero inoxidable; Inspección en detalle; Carbon fiber-reinforced polymer; Diseño

* Corresponding author.
E-mail address: atorres@imt.mx (A.A. Torres-Acosta).

https://doi.org/10.1016/j.hya.2018.05.004

1. Introduction

In the last three decades there has been a particular interest in the development of high strength concrete (HSC) materials and more recently in the development of high performance concrete (HPC) structures, which not necessarily implies the use of HSC. Although, in recent years this term has been fashionable, reality indicates that our Mayan, Egyptian, Roman etc., ancestors, understood the importance that the structures have a very long period of service life with no, or low, maintenance actions. In the case of port infrastructure, the enemy to defeat is the corrosion deterioration of the reinforcing (or prestressing) steel. This means that HPC structures in marine environments must tacitly take into account the corrosion factor. In addition to this, there is the economic factor, which requires that a structure has to have a long life performance at a low cost. This is possible in developed countries, but to obtain this in developing countries, it will require a longer timeline.

In the case of Mexico, an example of HPC structure is the Progreso pier, located in the North of the Yucatan Peninsula. This structure was designed and constructed by a Danish contractor named Christiani & Nielsen after winning the Mexican government design and construction bid for a new pier [2]. As part of the specifications, the Mexican government asked for a design that considered zero corrosion maintenance for 50 years and to be in working condition for at least 100 years. Nowadays it is 82 years since the Progreso Pier construction begun, and 77 years of being in service in good condition and without significant corrosion problems. The old Progreso pier consisted of a 1.7 km long viaduct and 205 × 50 m dock platform. The viaduct is formed by 145 concrete arches supported by 145 pier caps. Those pier caps are supported by two massive concrete circular columns each; hence, there are 290 piles in total. This is what is called a girder: two circular piles joined by a pile cap. The dock platform (250 × 50 m) has a similar substructure and structure to the viaduct. It is formed by 250 circular piles, 26 continuous arches and 27 continuous pile caps.

What was the formula to get this long-life structure? Christiani & Nielsen's design proposal minimized the use of steel to reduce the structure maintenance due to corrosion degradation. The Danish contractor presented a project that took into account, not only the environmental loads of the local atmosphere but also the characteristics of the local construction materials (porous coarse aggregate obtained from crushing locally available limestone).

2. Old Progresos' viaduct

2.1. Construction of old viaduct (1936–1941)

The structure was conceived of massive concrete and according to reports of the pier's constructors, it was one of first in which type 304 stainless steel smooth rebar was used apparently as shrinkage reinforcement. According to the Danish contractor, this stainless steel rebar was used only to avoid concrete shrinkage in the pile caps due to its massive dimensions. An approximated steel reinforcement index of 0.15% (equal to the area of steel divided by the pier cap cross section concrete area) of type 304 stainless steel smooth rebar (30 mm in diameter) was used.

Figure 1. View of cross girders and piles during the construction process.

The pier consisted of massive concrete and un-reinforced circular piles (3 m in diameter), arches (0.40 m wide) and walls. The pile caps (2.5 m in base and 3.0 m high) were the only structural elements reinforced with stainless steel. In gross numbers, 72,000 m^3 of concrete were used: 32 thousand for the circular piles, 30 thousand for the pile caps, arches and walls, and the rest for peripheral supports. A total amount of 23 thousand tons of cement were consumed, from which 17 thousand came from Denmark, and the rest from Mexico and the USA. An approximated total of 220 tons of stainless steel type 304 were used [4], and 170 thousand cubic meters of crushed limestone rock, of which 57 thousand were used as road filler and the rest were used for concrete fabrication. Its structural design was conceived to support a uniformly distributed load of 4 tons/m^2.

According to Christiani & Nielsen, the allowable design stress applied by the substructure to the foundation was 15 kg/cm^2, which increased to 25 kg/cm^2 when adding the other live loads [2]. Fig. 1 shows the pier construction. This pier is still in service whose maintenance is minimum and it focused on small concrete repairs and painting. Such repairs are associated to the installations of boat docking and boat impacts. Nevertheless, its load rating is in jeopardy at this moment, due to the load increase and traffic frequency, which has caused some structural degradation (i.e. crack appearance in some pile caps and arches).

2.2. Port extension (1980s–1990s)

During the 1980s, the Mexican federal government initiated the construction of a Remote Terminal, to which the old Progreso pier was joined by a 4-lane viaduct. The Progreso pier, whose original viaduct length was 2.2 km, now has an additional 4.5 km. Fig. 2 shows the whole pier extension. This addition transformed the Progreso port to a deep port, which can allow 10-m deep ships to dock.

The project and the materials with which the extension was constructed were very different from the first stage constructed by the Danish contractor. The Progreso deep port has been growing in a regular way during the last decade; to the degree that the traffic on the old 2.2-km viaduct (a 2-lane road) is

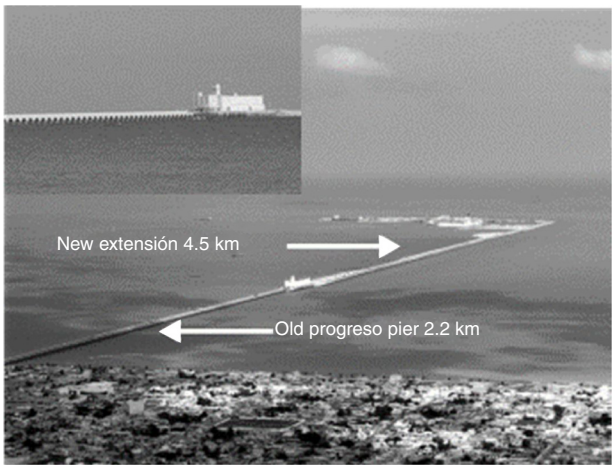

Figure 2. Aerial photograph of the old pier and the extension built in the 80s.

getting very slow, with more frequent vehicular transit and heavier loads. Studies made by the Mexican Institute of the Transportation (IMT in Spanish initials) demonstrated that the loads that the old viaduct is receiving at the moment are already matching the allowed fully factored design loads, which are 10 times greater than those that were supported by the pier structure at the beginning of its operation in 1941 [3].

2.3. *Old viaduct evaluations (2002–2013)*

In 2001, several inspections by the Mexican Institute of Transportation (IMT in Spanish), Research Center and Advanced Studies from IPN (CIN-VESTAV in Spanish), and the College of Engineering from the Autonomous University of Yucatan (FIUADY in Spanish), found evidence of the initiation of electrochemical and structural deterioration [1].

It was obvious that the pier was over demanded, and that a plan was needed to preserve its structural and electrochemical integrity. In common agreement with the Port authorities (the Integral Harbor Administration, API in Spanish), a plan to continuously evaluate the performance of the pier began in 2001. The evaluation program includes at least two annual inspections of its substructure (piles, pile caps and arches). These inspections have and will include load rating capacity of the structure and vehicular dynamic weighing, monitoring the appearance of incipient damages like arch cracking, and monitoring chemical and electrochemical parameters of the materials (i.e. concrete and stainless steel). During these inspections the research group has been able to obtain valuable data so that the harbor authorities can consider a maintenance plan in the short term.

The inspections included concrete material evaluation: petrography analysis, carbonation front, and electrical resistivity; and stainless steel evaluation: metallographic analysis, electrochemical measurements (half-cell potentials and corrosion rate). In addition to material evaluations, the program includes visual and structural surveys of the whole structure, dynamic monitoring (natural frequencies, modes of vibration) and static load evaluation (load vs. strain performance).

Results from the material evaluation performed to the concrete have shown high concentrations of chlorides (on the order of 1–2% by weight of concrete) at the rebar depth. This amount is about ten to twenty times the amount of chlorides needed to start corrosion of regular carbon steel, and in the barge of initiating corrosion of the stainless steel rebar used in the Progreso pier. Few corrosion problems were observed at the pier cap West and East face although stress corrosion cracking was developed in specific and non-concrete covered rebar hooks. This has warned API that a preventive maintenance program is needed to avoid corrosion problems in the old section of the pier in the near future.

Other results obtained during the continuous evaluation plan, performed by this group, included a detailed crack survey from some of the arches of the viaduct (its pattern is similar to the observed in Fig. 3). This crack intensification has warned API

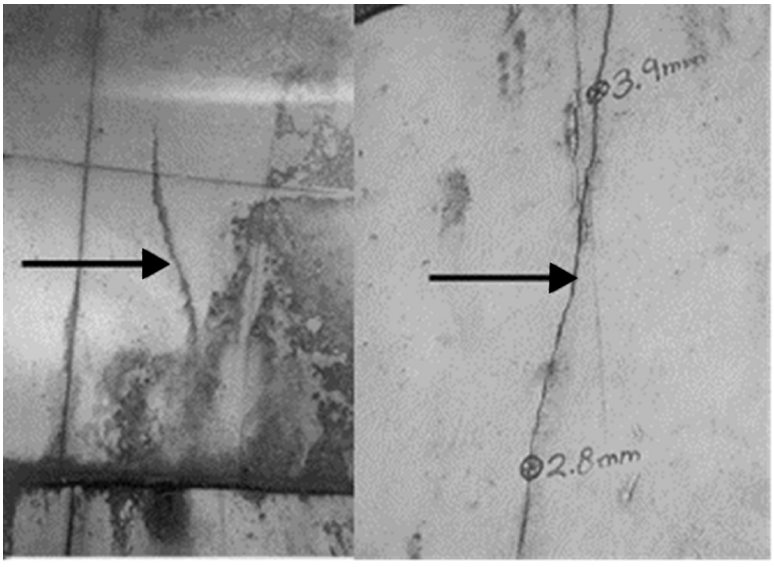

Figure 3. Typical structural cracks observed on the unreinforced concrete arches.

Figure 4. Rehabilitation of one of the cracked arches.

and the working group presented to API a detailed protocol to perform static and dynamic load tests to several of the pier arches [3].

2.4. Old viaduct rehabilitation (2003–2009)

As an important consequence of the detection of crack intensification (as it has warned API) and beginning of 2003, 54 arches were externally reinforced with Carbon Fiber-Reinforced Polymer (CFRP) composites, which have shown good corrosion resistance and enough structural strength to hold together the cracked arches (see Fig. 4). The way the CFRP bands were located was conceived to decrease the crack opening due to constant loading of the distress arches.

During a routine inspection in 2007, more arches presents structural cracks, therefore a second rehabilitation work was performed using similar CFRP strips during 2008. However, during this rehabilitation work, additional cracks were observed on the already repaired arches using the localized procedure: CFRP strips glued just in the crack length (Fig. 5). Thus, the procedure of externally reinforced the cracked arches using CFRP strips was changed from localized reinforcement (just placing CFP on top of cracks) to a general reinforcement placing CFP strips on all the width of the arches. In 2009 API obtained additional economical resources to reinforce all the 145 arches of the old viaduct, finishing this work at the end of 2009.

3. New Progresos' viaduct

After externally reinforcing all the arches of the new viaduct, the next maintenance strategy to the old viaduct was to avoid the transit of heavy load truck on it. Therefore, the need of a new viaduct construction was unavoidable, because there is no other way to maintain the old viaduct applying the heavy loads without possible collapse of part of this important structure in the port: the only passage to the Progreso's deep port. That is why at the end of 2013 API announced bidding for the executive project of a new viaduct, parallel to the old one, considering durability criteria in the design of this new structure. IMT was again solicited to be the entity to supervise the steps of the executive project, and define the durability criteria during the design of

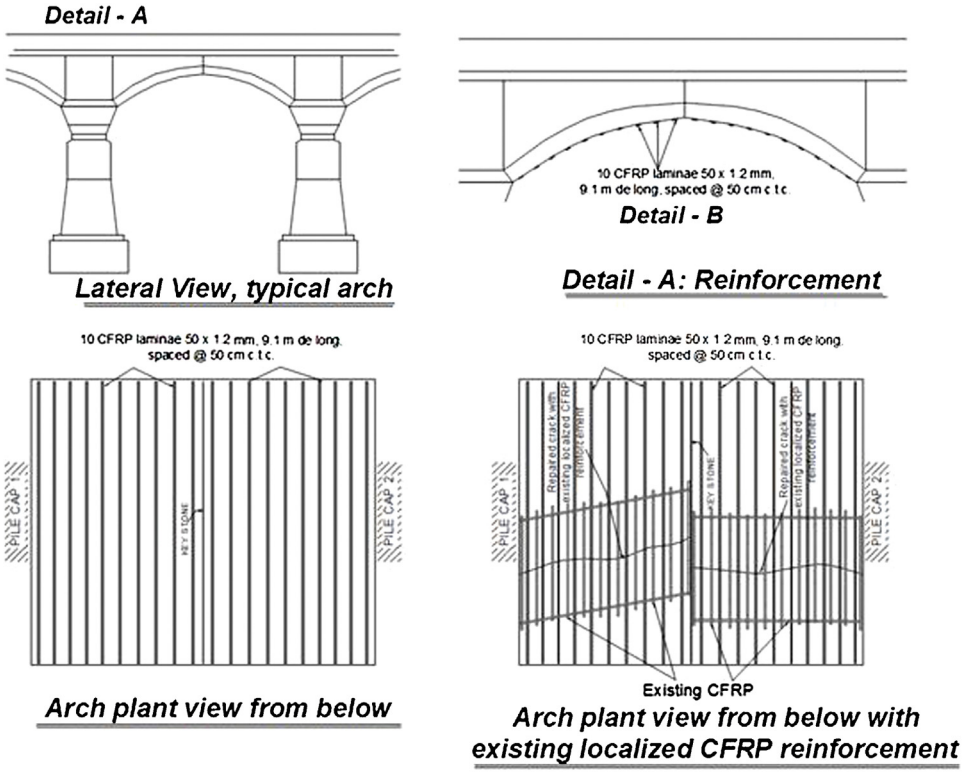

Figure 5. CFRP reinforcement of the cracked arches at the entire arch width. (a) Arch without previous reinforcement, (b) arch previously reinforced with localized CFRP strips.

the materials, construction procedures and future maintenance procedures.

3.1. Materials specifications

Although the good durability performance observed in the old viaduct from the use of thick concrete covers (>20 cm) and stainless steel bars, the possibility of using similar specifications for the new viaduct was rejected due to the price of the stainless steel reinforcement. This material is not available in Mexico, and the need to import all of it was not an option. Therefore, the design group was considering the improvement of the concrete performance, instead of using high cost reinforcement.

The main concern of the design group was to build a new concrete viaduct (bridge) with same service life than the old viaduct, using same porous aggregate (limestone with about 20–25% total void content). Another concern was to establish some kind of quality control with the cement, since the actual Mexican standard is loose on defining the type, quality, and quantity of the mineral additions integrated to the Mexican cements, to diminish the amount of Clinker on them. Therefore, several specifications were considered to the concrete's mix design to increase the durability of the main material of the new viaduct structure.

Based on the experiences obtained by the design group after more than 15 years of inspection, evaluation, diagnosis, and rehabilitation of several bridges and piers in Mexican marine environment, a concrete's mix design was proposed and some hardened concrete specifications were also defined to achieve a durable concrete with a service life of at least 80 years. The main laboratory tests considered for hardened concrete's quality control was electrical wet resistivity, thus concrete's mix proportion was design to get high values of this physical parameter, which helps to measure indirectly the porosity and the tortuosity. Another specification dealt with the rapid chloride permeability test, which the concrete of this new viaduct need to fulfill. Based on the raw material available in the Yucatan Peninsula to fabricate the concrete (mainly aggregates, water, and Portland cement type), the executive project considered the components listed in Table 1 to obtain a durable concrete for this new viaduct.

Table 1
Concrete mix characteristics.

Material	Properties
Portland cement	Clinker content >95%; Blaine >4000 g/cm^2; cement content >480 kg/m^3
Water to cement ratio w/c ratio	0.35
Coarse aggregate	MAS: 19 mm; specific gravity >2.4; Los Angeles wearing machine <40%
Fine aggregate	Specific gravity >2.4
Water	Cl^- content <90 ppm
Silica fume	>5%, but <10%
Electrical wet resistivity	>70 kΩ cm
Rapid chloride permeability	<500 C

3.2. New viaduct geometry

The geometry of the structural elements in the substructure as well as the structure in the new viaduct, was also considered

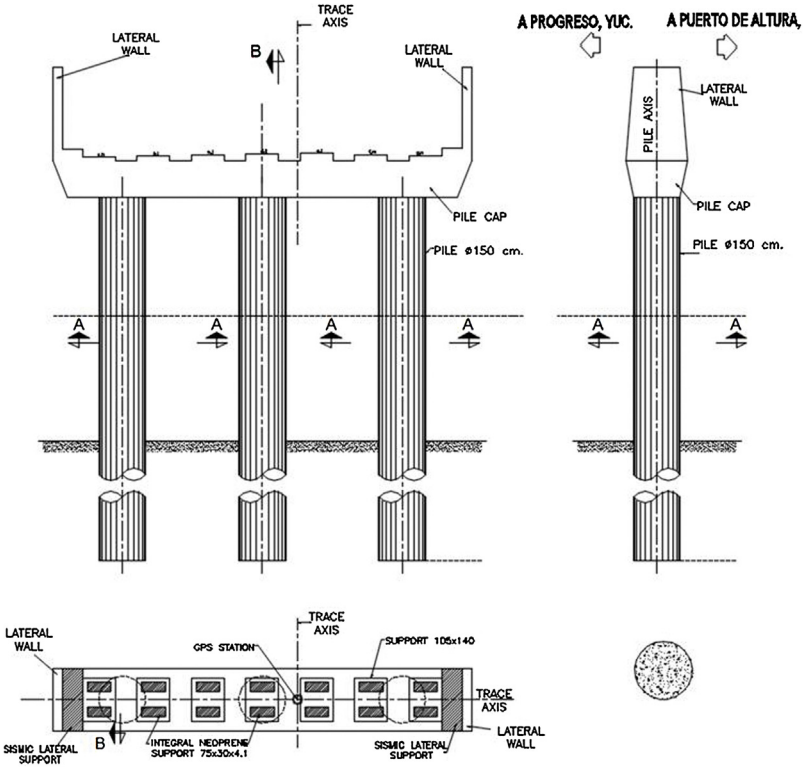

Figure 6. Substructure detail of the Progreso's new viaduct.

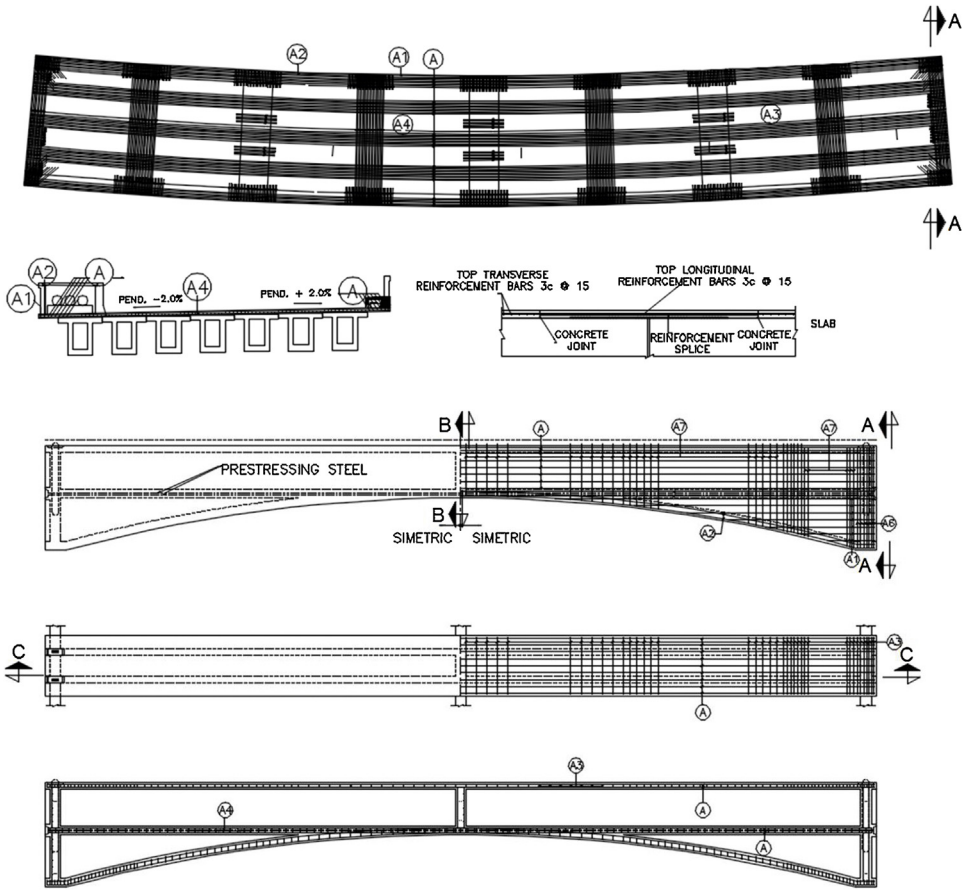

Figure 7. Superstructure details of the Progreso's new viaduct: above deck, below prestressed arched beam.

to get a durable structure with little maintenance (mainly routinely, i.e. bearings, deck surface, deck joints, painting metallic elements, parapets, trenches). The substructure consists of three reinforced concrete pylons (1.5 m diameter, 10 cm concrete cover) and one reinforced pile cap (1.20 × 1.50 m, 7 cm concrete cover), as presented in Figs. 6 and 7.

A second specification considered to increase the durability of the new viaduct was to use in all reinforcement a polymer/ceramic/corrosion inhibitor coating. This coating was considered after a laboratory evaluation before the construction of the new viaduct (no chemical composition of this coating from the manufacturer was obtained). With the experiences observed in substructures in similar tropical marine environment, where epoxy coated rebar was used and failed by corrosion initiation in periods less than 10 years of being in service [5], tests were performed to determine how much is the protection of the steel reinforcement if the concrete was contaminated with chlorides (>2% by cement weight) during the executive project conceptualization. The tested coating included a corrosion inhibitor to increase the chloride critical threshold to initiate corrosion of typical carbon steel.

Finally, a third corrosion protection was defined in the new viaduct executive project, which included a siloxane coating to all concrete elements (no chemical composition of this coating from the manufacturer was obtained): reinforced (substructure/superstructure) and prestressed (superstructure) elements. Special care was taken to achieve a good penetration of the siloxane coating since the concrete design was to obtain a low permeability material, thus the siloxane molecule redesign to have it smaller than the commercial product has.

3.3. New viaduct construction

Construction started in February 2014, and ended in May 2017. Fig. 8 shows some aspects of the construction of Progreso's new viaduct. More details of the construction processes will be published in the near future. The works are programed to end in May next year, but everybody knows that construction works normally ends few weeks later, or even months due to none programed activities or contract extensions.

4. Conclusions

Detailed inspection of Progreso's viaduct provided enough quantitative information to determine that the stainless steel bars from the girders are exposed to a high chloride concentration. A structural inspection, including load capacity tests, indicated that the old viaduct is experiencing structural distresses by the formation of surface cracks on arches and pier caps. The rehabilitation techniques used included the use of external CFRP strip reinforcement for the crack opening attenuation. The crack distress continued, thus the design and construction of a new viaduct was

Figure 8. Construction process photographs: substructure construction stage.

proposed to the Port Authorities, thus its construction started in 2014 and ended in 2017. A detailed inspection program has been presented to the Mexican Government authorities to perform a detailed inspection in order to increase the service life of the old viaduct, with strategic, historical and technological importance for the region.

Financial support

The present investigation was partially supported by the Integral Port Administration (API in Spanish) of Progreso, since the beginning in 2002 until 2017.

Acknowledgements

The authors are indebted to the Administracion Portuaria Integral (API in Spanish) Progreso for the support of this investigation, design, construction technology development, and innovation. The opinions and findings in this investigation are those of the authors and not necessarily those of the funding agencies.

References

[1] P. Castro, O. Troconis, E. Moreno, A.A. Torres-Acosta, M. Martínez, A. Nudsen, Inspecting a half-century reinforced concrete pier made with stainless steel reinforcement in Mexico, in: NACE Corrosion/2002 Paper 02207, 2002, pp. 10.

[2] A. Christensen, Pier at Progreso. In 50 Years of Civil Engineering: Christiani & Nielsen, Copenhagen, Denmark, 1954.

[3] M.J. Fabela-Gallegos, A.A. Torres-Acota, Structural integrity of arches 5 and 12 of the Progreso pier old viaduct. Technical Report 001/2004 Project EE03/04, Instituto Mexicano del Transporte, Sanfandila, Queretaro, Mexico, 2004 (in Spanish).

[4] A. Knudsen, T. Skovsgaard, Ahead of its peers, Concr. Eng. Int. (1999) 58–61.

[5] A.A. Sagüés, Corrosion Evaluation of Bridges with Epoxy-Coated Rebar. Final Report Contract No. BD544-23 Florida Department of Transpoortation, Tallahassee, FL, USA, 2009.

últimos números publicados

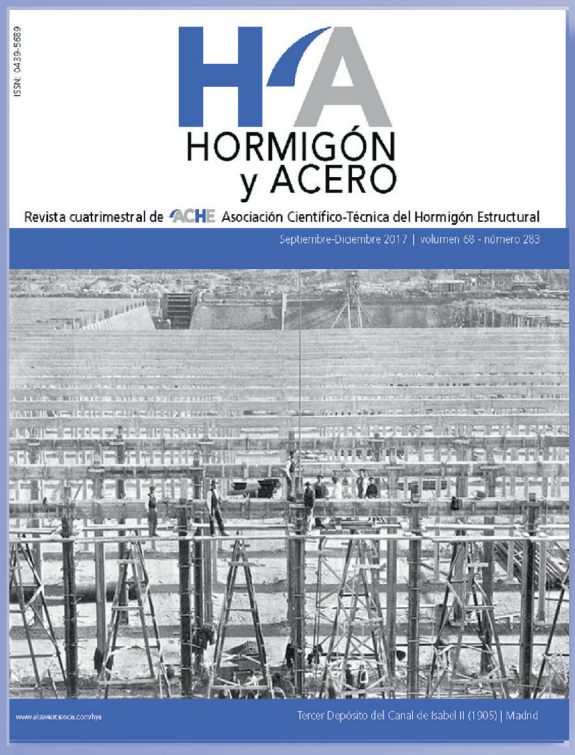

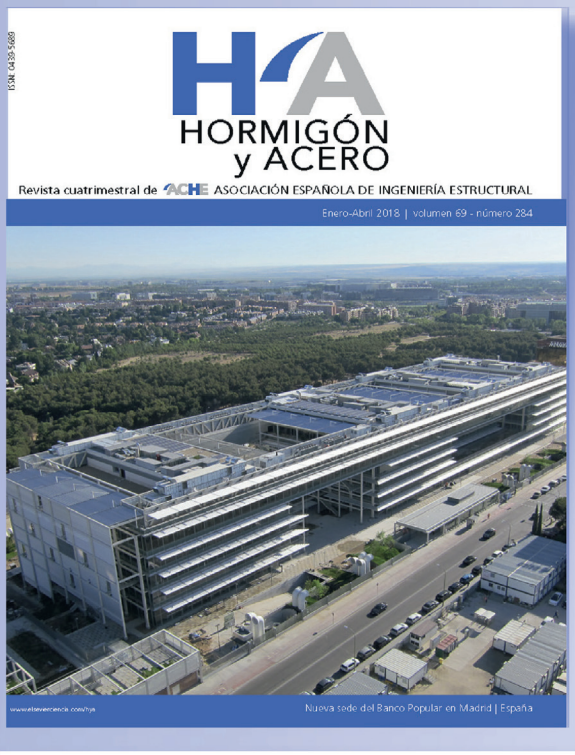

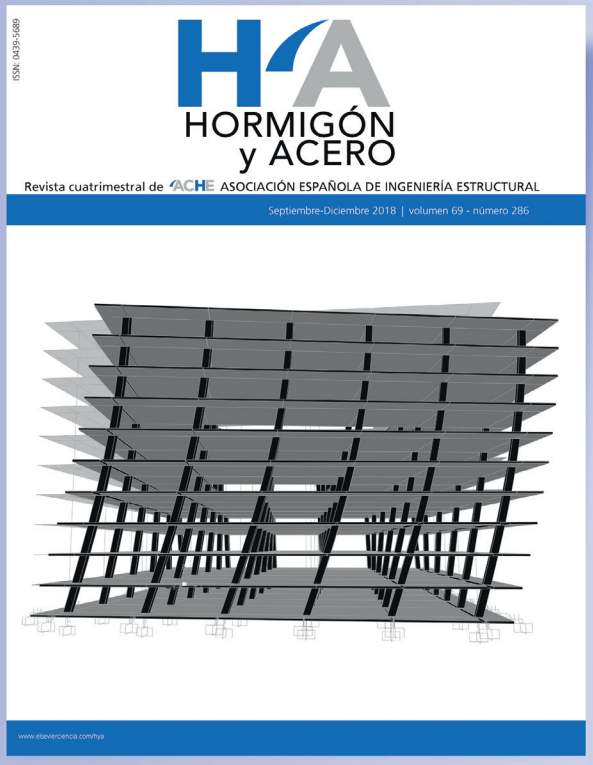

ACHE

Base de datos de artículos publicados en números
cambiar esta dirección Web por:
www.hormigonyacero.com

Available online at
ScienceDirect
www.sciencedirect.com
Hormigón y Acero 2019; 69(S1):43–51
www.e-ache.com
www.elsevierciencia.com/hya

Application of combined electrochemical treatments to reinforced concrete: Electrochemical chloride extraction plus cathodic protection

Aplicación de tratamientos electroquímicos combinados al hormigón armado: extracción electroquímica de cloruros más protección catódica

Miguel Ángel Climent [a,*], Jesús Carmona [b], Pedro Garcés [a]

[a] *Dr. en Ciencias Químicas, Catedrático, Departamento de Ingeniería Civil, Universidad de Alicante, Alicante, Spain*
[b] *Dr. Ingeniero de Caminos, Profesor Ayudante Doctor, Departamento de Ingeniería Civil, Universidad de Alicante, Alicante, Spain*

Received 11 December 2017; accepted 17 May 2018
Available online 14 July 2018

Abstract

It has been studied the possibility of using a graphite–cement paste anode for combined treatments of electrochemical chloride extraction plus cathodic protection on reinforced concrete elements. These treatments would be interesting in cases of structures heavily contaminated with chlorides and continuously exposed to a harsh chloride environment. It has been shown that, in the experimental conditions of this work, the anode is not damaged during the electrochemical chloride extraction step. The application of a previous chloride extraction step allows working with a lower current density at the cathodic protection step, which reduces the risk of damages of the anodic system. A chloride barrier effect parameter has been defined, based on the reduction of the chloride uptake by concrete, due to cathodic protection action, referred to the chloride uptake of the reference (not treated) specimens. The values of the chloride barrier effect parameter found in this work are about 20%.

Keywords: Steel reinforced concrete; Corrosion; Electrochemical chloride extraction; Cathodic protection; Cathodic prevention

Resumen

Se ha estudiado la posibilidad de utilizar un ánodo de pasta de grafito-cemento para tratamientos combinados de extracción electroquímica de cloruros y protección catódica de elementos de hormigón armado. Dichos tratamientos serían interesantes en casos de estructuras contaminadas con cloruros y permanentemente expuestas a un ambiente salino agresivo. Se ha demostrado que, en las condiciones de este trabajo, el ánodo no resulta dañado durante la etapa de extracción de cloruros. La aplicación de una etapa previa de extracción de cloruros permite aplicar la protección catódica con una densidad de corriente menor, hecho que reduce el riesgo de daños del sistema anódico. Se ha definido un parámetro de efecto barrera de cloruros, basado en la reducción de la penetración de cloruros, debida a la protección catódica, referida a la penetración de cloruros de referencia (sin protección catódica). Los valores de dicho parámetro encontrados en este trabajo son del 20%, aproximadamente.

Palabras clave: Hormigón armado; Corrosión; Extracción electroquímica de cloruros; Protección catódica; Prevención catódica

1. Introduction

Several electrochemical techniques have been successfully used to the protection and remediation of steel corrosion in reinforced concrete structures. All these techniques are based on the lowering of the electric potential of steel [1–7]. This effect can be obtained both by connection to a less noble metal, as in cathodic protection (CP) by sacrificial anodes, or by connection to the negative pole of an electric direct current source, as in CP by impressed current [8–12]. The techniques can also be classified in permanent and temporary techniques. Permanent

* Corresponding author.
E-mail address: ma.climent@ua.es (M.Á. Climent).

https://doi.org/10.1016/j.hya.2018.05.003

techniques are CP, whose aim is to stop the steel reinforcement corrosion, and its variant called cathodic prevention (CPre), following Pedeferri et al. [9,11]. The objective of CPre is to prevent the initiation of steel corrosion in new structures. On the other hand, temporary techniques are those intended to change the prevailing corrosion conditions of the structures by lowering its chloride content, such in electrochemical chloride extraction (ECE) [13–18], or by increasing the pH of concrete, such in electrochemical realkalization (ER) [19,20]. In this work we concentrate on applications of the techniques aimed to prevent the onset of corrosion (CPre), improve the prevailing conditions (ECE) or stop the corrosion of steel reinforcement (CP), due to chloride contamination of concrete, excluding sacrificial anode applications.

All the electrochemical techniques have in common the reactions at the surface of steel, the cathode, i.e. oxygen reduction to produce hydroxide ions (the basis of ER), and eventual hydrogen gas evolution if negative enough potentials are reached. Hydrogen production is considered as a potentially harmful process, due to the possibility of hydrogen embrittlement of high strength steels [5,6]. Besides to these reactions the system benefits also from effects due to migration of ions induced by the electric field: hydroxide (OH^-) and chloride (Cl^-) ions move from cathode to the external anode. This latter effect is the basis of ECE. The permanent techniques, i.e. CPre and CP can be considered as more sophisticated in the sense that they need to guarantee the maintenance (CPre), or the new formation and maintenance (CP), of the passivating layer on steel, by maintaining the potential of steel below the pitting potential imposed by the presence of a certain Cl^- concentration in the concrete's inner pore solution [9–12]. These electrochemical conditions induce a reduction of the ratio of the concentrations of chloride and hydroxide ions, $[Cl^-]/[OH^-]$, near the steel. A non-negligible contribution to the maintenance of the passivating layer comes from the so-called chloride barrier effect acting in CPre and CP applications on steel reinforced structures permanently exposed to an aggressive chloride environment [9,11].

The operation conditions of the abovementioned electrochemical techniques differ in each case. CP and Cpre, applied to reinforced concrete, need using a permanently fixed anode, which is usually an embedded metallic wire mesh, typically a titanium mesh activated with mixed metal oxides, or they use conductive coatings or overlays, such as conductive cementitious overlays [21–24]. CP typically applies current density values between 5 and 20 mA/m^2, while CPre needs only 1–3 mA/m^2. Nevertheless, in the case of CP the actual current density needed to effectively protect the steel is higher the higher is the Cl^- content of concrete. The success of CP or CPre depends greatly on an optimum design of the anodic system, able to provide an adequate current distribution on the steel reinforcement [9]. ECE, as a temporary technique aimed to reduce the Cl^- content of concrete, uses external anodes and electrolytes [25], although it has been demonstrated that a conductive cementitious anodic overlay can also be used as the anode for ECE [26,27,28,29]. The typical current density for ECE applications on reinforced concrete elements is in the range 1–5 A/m^2, while the total electric charge passed is usually between 1×10^6 and 5×10^6 C/m^2. From an electrochemical point of view the current density should be defined as referred to electrode surface, i.e. the surface of the steel cathode. However, in engineering field applications it is sometimes difficult to know the steel reinforcement area. So, many times the current density is referred to exposed concrete surface, which, in the case of anodic overlay systems is equal to the anode area.

In the case of CP a critical point of concern is the possibility of malfunction of the anodic system, due to the acidity produced by the electrochemical reactions at the anode, which can impair the contact between the embedded conducting material of the anode and the surrounding cement paste. This risk increases when the applied current density is higher than 20 mA/m^2 [21].

The Department of Civil Engineering of the University of Alicante has been conducting research on the use of conductive cement pastes (CCP), based on mixes of cement with different carbonaceous materials, as anodic coatings for applications of electrochemical techniques on reinforced concrete [24,26–31]. One of the most appealing possibilities offered by these permanent anodic overlays is the possibility of combined successive treatments of ECE plus CP, without changing the anode. This combination of treatments may be convenient in the case of structures heavily contaminated with Cl^- ions, whose chloride environmental load is expected to be maintained high in the future, for instance the case of reinforced concrete exposed to de-icing chloride salts, or a harsh marine environment. In these cases it may be deemed necessary to first reduce the Cl^- content of concrete by applying ECE, and later maintain the steel protected by a permanent CP treatment, without the need to apply a too high CP current density, thus reducing the risk of malfunction of the anode due to the acidity produced at its surface.

2. Methodology

Table 1 indicates the nomenclature of the specimens and the electrochemical treatments applied to each one. The specimens intended for CPre trials (P and B) were prepared with chloride free concrete, since the CPre treatments are designed for being continuously applied to newly constructed structures, starting from the very beginning of the structure's service life [9,11]. On the other hand, the rest of specimens dedicated to testing the CP, ECE + CP or ECE + CPre were prepared with concrete admixed with Cl^- ions. The CP treatments are known to allow stopping an ongoing reinforcement corrosion process due to chlorides. Finally, the combined treatments, (ECE + CP and ECE + CPre), are tested here to represent situations in which, the ECE technique is first applied to reduce an initial excessive Cl^- content, but afterwards it is deemed convenient or necessary a subsequent application of a continuous protective treatment, (CP or CPre), because the structure will follow being exposed to an aggressive chloride environment. It must be stressed that all specimens included in Table 1, even those that were not given any of the electrochemical treatments (R and P), were subjected to the same salting regime during the 24 weeks period that lasted the CP or CPre treatments: 65 ml NaCl 0.5 M weekly sprayed

Table 1
Nomenclature of specimens for application of the electrochemical techniques.

Studied techniques	Initial % Cl^- in concrete	Reference sample	Treated sample
CP	2	R (no electrochemical treatment)	A (CP treated)
CPre	0	P (no electrochemical treatment)	B (CPre treated)
ECE + CP	2	ER (treated only with ECE)	EA (ECE + CP treated)
ECE + CPre	2		EB (ECE + CPre treated)

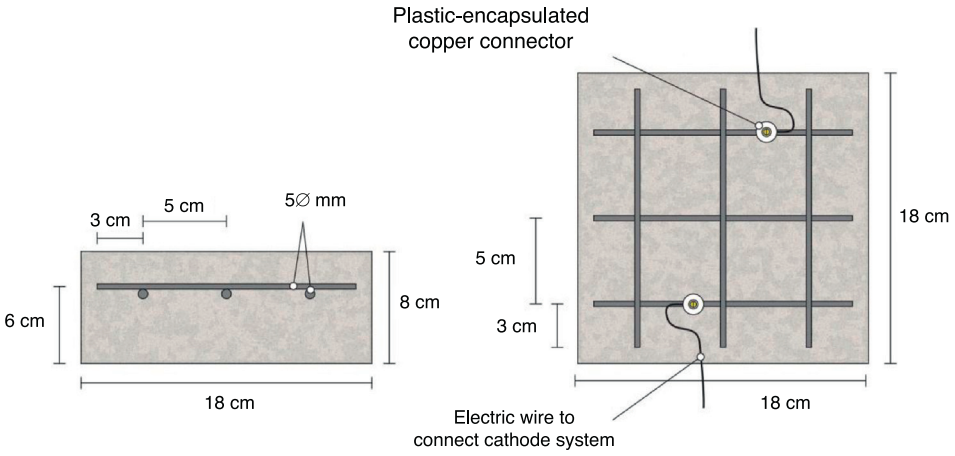

Figure 1. Sketch of reinforcement of samples and connection of the cathodic system (steel reinforcement). Adapted from [24].

onto the concrete or anodic overlay surface, in order to simulate the continued chloride contamination due to exposure to a very aggressive environment as mentioned above.

2.1. Reinforced concrete specimens

The specimens were prism-shaped reinforced concrete elements, with a dimension of $18 \times 18 \times 8\,cm^3$, which were reinforced by a grid $16 \times 16\,cm^2$ composed of six steel bars (5 mm diameter) welded symmetrically forming squares of 5 cm side, and placed 2 cm under the anode, Fig. 1. The concrete dosage was as shown in Table 2. Two mixes were prepared: one without added chloride for preparing the specimens intended for pure cathodic prevention (CPre) treatments, and another mix containing 2% Cl^- relative to cement mass for the specimens used in cathodic protection (CP) applications or combined treatments (ECE + CP) and (ECE + CPre), see Table 1. Once the formwork was removed, the specimens were moist-cured at 95–98% relative humidity (RH) for 28 days. The characteristics of the hardened concrete were as follows: compressive strength 37.8 N/mm^2 [32], porosity 11.1% [33], and bulk density 2.38 T/m^3 [34].

Table 2
Concrete dosage for preparation of the test specimens.

Material	Dosage
Portland cement CEM I 42.5 R	250 kg/m^3
w/c ratio	0.65
Limestone aggregate max. size 12 mm	1890 kg/m^3
Superplasticizer	2.50 kg/m^3
NaCl	Nil or 3.3% (2% Cl^- relative to cement mass)

Fig. 1 also shows the system used for connecting the reinforcement (cathode system) to the negative pole of the electric power source, through plastic isolated copper connectors screwed to the rebar.

2.2. Common experimental details of the electrochemical tests

All the electrochemical tests were performed using a CCP anode. The anodic overlay system was prepared by hardening a graphite–cement paste (GCP) obtained by mixing graphite powder and Portland cement at 50%–50% in mass. Water to solid mix ratio was 0.8. Secondly, a 2 mm thick layer of this paste was applied on the surface of each specimen, and then all of them were moist-cured for 10 days. After that, two grooves were performed lengthwise onto the anodic overlay, without reaching the concrete surface, in order to receive both graphite rods to connect to the positive pole of the electric source. To finish up, these rods were overlaid with graphite–cement paste in order to join with the anode system perfectly, but avoiding any contact between graphite rods and concrete. A PVC receptacle was assembled on the top of the samples to retain both ECE electrolyte (distilled water) and/or the dissolution used during CP or CPre applications to simulate a continued chloride contamination (65 ml NaCl 0.5 M applied weekly), Fig. 2. The ratio between the surface of concrete covered by the anodic overlay and the surface of the primary anodes (graphite rods) was 9.6;

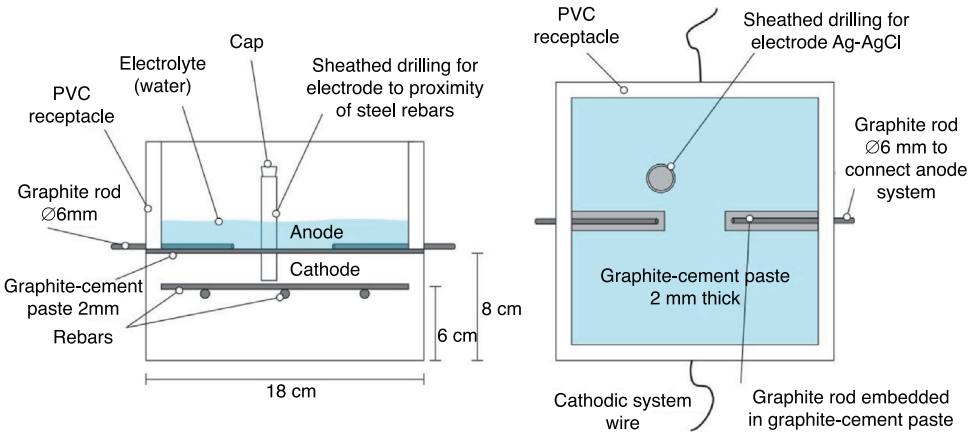

Figure 2. Sketch of specimen assembly.
Adapted from [24].

the ratio between the surface of concrete covered by the anodic overlay and the total surface of the steel bars was 1.7, Fig. 2. All current density and electric charge density values reported in this work are relative to surface of concrete, (equal to the anode surface), except otherwise stated.

The resistivity of the graphite–cement paste was measured through the four-probe method. To this end, paste specimens were cast in $4 \times 4 \times 16\ cm^3$ moulds, and moist-cured at 95–98% RH during 14 days. The experimental details of the measurements can be found elsewhere [35]. The average obtained resistivity was 1.5 Ω m.

The measurements of steel corrosion potential (E_{corr}) and all the single electrode potentials, were performed using Ag–AgCl reference electrodes. These electrodes were housed in respective holes drilled from the exposed surface of the concrete specimen (that bearing the graphite–cement anode) to the vicinity of the rebar, Fig. 2. For this purpose, the holes were sheathed with a plastic tube, and filled with a KOH 0.2 M aqueous solution, trying to approach the physical-chemical conditions of the concrete's inner pore solution.

In this way nine specimens were prepared, seven of them with salt in the mixing water and two without it. Two of the salted specimens were used only for determining the efficiency of the ECE process. Concrete cores were extracted from them, and their chloride content profiles were determined, in one case before and in the other case after ECE. These two specimens were discarded after coring. The seven remaining specimens were intended for the tests corresponding to CP, CPre, and the combined treatments (ECE + CP) and (ECE + CPre), see Table 1.

The ECE efficiencies were calculated as the percentages of reduction of the initial chloride content. Obtaining the chloride content profiles before and after the ECE trials allowed calculating the local and overall efficiencies. At the end of the 24 weeks of exposure to a severe Cl^- load, i.e. the first phase of CP and CPre treatments, see Section 2.4, chloride content profiles were obtained from all the reinforced concrete specimens. The Cl^- profiles were measured following essentially RILEM recommended procedures [36]. Cylindrical concrete cores, 95 mm diameter and 20 mm height (up to the rebar depth), were extracted. From these cores, concrete dust samples were obtained by grinding thin (2 mm thick) successive parallel layers to the exposed surface [36]. In this way 10 concrete dust samples were gained from each core, thus allowing the obtention of sufficiently detailed chloride content profiles. The determination of the samples' acid soluble chloride contents was carried out by potentiometric titration [37,38]. All the chloride content values are expressed in this work as % Cl^- relative to cement mass.

2.3. ECE treatments

Four of the specimens made with saline mixing water were subjected to ECE. For this purpose, the specimens were electrically connected in series by pairs to a direct current source. The relevant parameters of the ECE treatments are shown in Table 3. A low charge density was applied, only 1.5 MC/m^2 relative to concrete surface (2.6 MC/m^2 relative to steel surface). The current source feeding voltage (ΔE_{feed}) was controlled at a level below 40 V during the processes, for safety reasons. It was necessary in this respect to interrupt the current passage two times (two pauses of 24 h each one) along the treatment. The whole processes were performed inside a fume hood to eliminate the chlorine, $Cl_2(g)$, produced by electrochemical oxidation of the Cl^- ions extracted from the concrete. When the ECE processes were finished, the pH values of the electrolytes were measured in order to check the acidifying effect caused by the electrochemical anodic reactions.

2.4. Application of CP, CPre and the combined treatments ECE + CP and ECE + CPre

This section describes the details of the experiments carried out to demonstrate the applicability of the GCP anodes for combined protective treatments of ECE + CP and ECE + CPre, please refer to Table 1.

The CP treatments were applied with 15 mA/m^2 of current density (relative to concrete or anode surface) to two specimens, one of those previously treated with ECE (EA in Table 1) and the other one without previous treatment (A in Table 1). On the other

Table 3
Summary of ECE data.

ECE. Specimens with GCP as anode. Electrolyte: dammed distilled water			
Initial % Cl^-	2% relative to cement mass		
Current density	2 A/m^2 of concrete exposed surface (3.4 A/m^2 of steel surface)		
Initial ΔE_{feed}	16–24 V	Final ΔE_{feed}	23–22 V
Electric charge density	1.5 MC/m^2 of concrete exposed surface (2.6 MC/m^2 of steel surface)		

hand the application of CPre with 2 mA/m^2 of current density (relative to concrete surface) to a sample previously ECE treated (EB in Table 1) and to another manufactured without salt and not ECE treated (B in Table 1). The values of the current densities relative to the steel bars surface are 25.5 mA/m^2 and 3.4 mA/m^2 for the CP and Cpre treatments, respectively. The direct current source was programmed to maintain a constant current density along the whole processes. Each application has its reference sample without treatment of CP or CPre to compare the results. The reference sample for the specimens subjected to combined treatments (EA for ECE + CP, and EB for ECE + CPre) is ER. R is the reference for A, and P is the reference for B.

The application of CP and CPre consisted of two phases:

Phase 1. First 24 weeks. The aforementioned treatments CP and CPre were continuously applied during the first 13 weeks. Then, the current was switched off for 4 weeks and after that, treatments were resumed to the end. Chloride contamination was continuously applied, even during the switch off periods.

While applying the CP and CPre treatments some electrochemical parameters were measured. During the current passing periods the feeding voltage of each specimen, ΔE_{feed}, was obtained as the potential difference between cathode and anode; and the individual anodic and cathodic potentials, E_a and E_c, respectively, were measured against the reference electrode Ag–AgCl. Finally, in order to check the efficiency of CP and CPre as maintainers of protection conditions of steel, the "100 mV decay" criterion was used, as is specified in ISO 12696:2012 [39]. This criterion has been also extensively employed for this purpose by several researchers [21,40]. The method consists in obtaining the 4 h potential decay (ΔE_{decay}), that is the difference between E_c^{4h} (the value of E_c 4 h after the current switch off), and the instant-off cathodic potential E_c^{io}, which in this case was measured 1 s after the current switch off. The minimum value of the 4 h depolarization must be 100 mV for an adequate corrosion protection of steel [39]. The values of E_c^{io} were monitored with an automatic data logger able to obtain and record 500 measurements in 6 s, after the current switch off.

Once the 24 weeks processes were fulfilled, cores were extracted from all specimens of Table 1, and their respective Cl^- content profiles were obtained. This was done with the purpose of evaluating the net effect of the electrochemical treatments on the Cl^- ion uptake by the reinforced concrete specimens during the continued exposure to a very aggressive environment.

Phase 2. At the end of Phase 1 it was observed that all the specimens had lost the steel protection condition, evidenced by ΔE_{decay} values lower than 100 mV. Then, it was decided to start this second phase with the objective of recovering the protection conditions of steel by adjusting the current density of the CP treatments. The procedure was to increase progressively the current density during 4 weeks, starting with a value of 20 mA/m^2, until obtaining the protection conditions.

3. Results and discussion

3.1. Application of ECE

Four of the reinforced concrete specimens were subjected to an ECE treatment before starting the first phase of the CP and CPre treatments, see Section 2.3. Once finished the ECE process with the settled parameters, Cl^- content profiles were obtained, corresponding to the states before and after the ECE treatment. The local ECE efficiencies, understood as percentage of Cl^- content removed, are plotted in Fig. 3. The average of removed Cl^- was 51% of the initial content, i.e. the residual Cl^- content of concrete after ECE was approximately 1% referred to cement mass. This indicates a good performance of the ECE process applied on a conventional ordinary Portland cement concrete with the GCP anodic overlay system, for a relatively low charge density of 1.5×10^6 C/m^2 relative to concrete surface. This result can be compared to the 41% efficiency obtained for a very similar reinforced concrete element, with the same initial amount of Cl^-, subject to an ECE treatment, using a Ti–RuO_2 mesh anode, and passing a total charge density of 1 MC/m^2 relative to concrete surface [26].

The pH values determined for the electrolytes, after the ECE experiments, were in the range 5–5.5. This means that the acidity

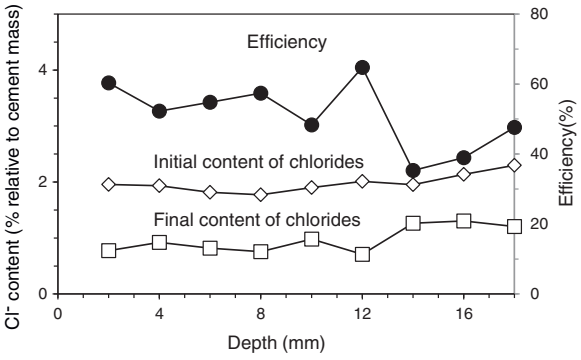

Figure 3. Chloride concentration profiles before ECE (initial) and after ECE (final), and local efficiencies of the extraction process. ECE details: current density: 2 A/m^2, charge density: 1.5 MC/m^2, both related to exposed concrete surface.
Adapted from [24].

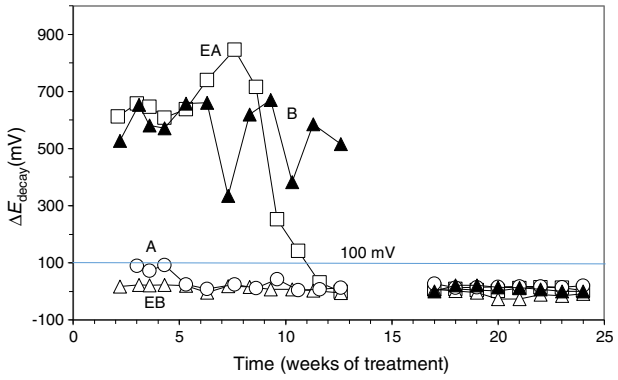

Figure 4. Evolution of ΔE_{decay} during the CP or CPre treatments. A: CP; B: CPre; EA: ECE + CP; EB: ECE + CPre. All of them subjected to Cl^- contamination during the 24 weeks. The electrochemical treatments were interrupted between week 13 and week 17.
Adapted from [24].

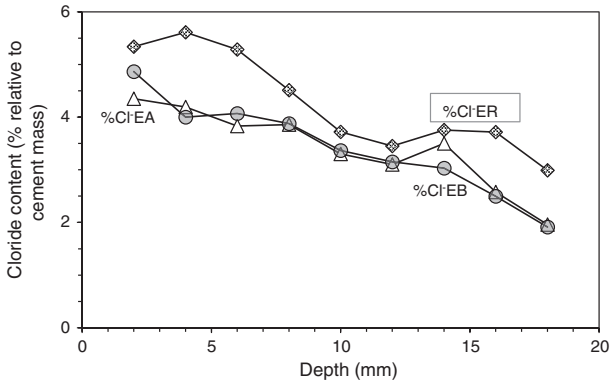

Figure 5. Profiles of Cl^- content in specimens treated previously with ECE and after with CP (EA), with ECE and after CPre (EB), and in the reference sample only treated with ECE (ER), all of them subjected to Cl^- contamination process, after ECE and first phase of CP or CPre (24 weeks).
Adapted from [24].

of the electrolytes had increased slightly, (the initial electrolyte was distilled water). This acidifying effect may be due to several of the electrochemical anodic reactions, namely the oxidation of hydroxide ions or water to O_2(g) and the oxidation of carbon to CO_2(g). It is possible that the alkaline character of the graphite–cement paste anode may have reduced the acidity produced by those electrochemical processes. It is worth noting that no sharp increase of the feeding voltage was observed during the ECE treatments. This suggests that no important damage of the GCP overlay has been produced during ECE [21], even though these trials are performed with a high current density of 2 A/m^2. We must recall that the ECE trials are performed under continuous liquid ponding of the anode, and its duration is short, about eight days.

3.2. First phase of CP and CPre treatments

In this section we describe the results of tests carried out to investigate the performance of the GCP anodes during protective electrochemical treatments to reinforced concrete elements affected by steel corrosion due to chloride contamination, such are CP, CPre and combined treatments of ECE + CP or ECE + CPre, see Table 1.

To verify the effectiveness of CP and CPre treatments for protecting steel from corrosion, the "100 mV decay" criterion [39] was used, as stated in Section 2.4. Fig. 4 shows the evolution of the ΔE_{decay} values for the specimens in Table 1, during the 24 weeks experiments. The ΔE_{decay} values of the A specimen, treated only with CP, practically never reached the threshold value of 100 mV. It seems that a 15 mA/m^2 current density was not sufficient to provide protection to steel in such harsh conditions: initial Cl^- content of 2% plus the continued salting regime (65 ml NaCl 0.5 M weekly sprayed onto the anodic overlay surface). Regarding the EA specimen (ECE + CP), the protection conditions of steel were kept during 11 weeks because of the current circulation, despite external Cl^- loading. Cathodic protection of 15 mA/m^2 current density, relative to concrete surface, was able to keep protective conditions for the steel reinforcement if the initial Cl^- content of the specimen was about 1% (EA). In the case of the specimen with initial Cl^- content of about 2% (A), a higher current density would be needed for reaching the protection conditions [9,11]. These observations corroborate the main hypothesis of the present research, i.e. in cases of reinforced concrete structures with a high Cl^- contamination subject to very harsh chloride environments, it would be advantageous to apply successively an initial ECE treatment to reduce the Cl^- content, and then maintain protective conditions to steel through a continuous CP treatment without the need of using a too high CP current density, which could eventually impair the performance of the anodic system [21]. These combined treatments, ECE + CP, would be more conveniently implemented with the CCP coatings, since the same anode can serve both for the ECE and for the CP treatments.

Regarding the CPre treated specimens (cathodic current density 2 mA/m^2 relative to concrete surface), specimen B showed ΔE_{decay} values higher than 100 mV up to the current switch off at 13th week, confirming the capacity of continuously applied CPre treatments to keep steel protection conditions for an initially Cl^- free reinforced concrete, despite extensive external Cl^- load [9,11,41,42]. On the other hand such a low current density is unable to protect steel if concrete is previously contaminated at a level of about 1% relative to cement mass, and steel has started to corrode, as shown for specimen EB (ECE + CPre) in Fig. 4.

At the end of Phase 1 all the reinforced concrete specimens had reached a very high degree of Cl^- contamination, as can be appreciated in Table 4. Nevertheless, some comparisons can be done on the behaviour of the different cases. For instance, Fig. 5 shows that the specimens treated with ECE + CP (EA) or ECE + CPre (EB) during Phase 1, have experienced less Cl^- ingress than the reference specimen ER, which after the ECE trial was left untreated during the Phase 1. This represents a further evidence of the "chloride barrier effect", mentioned by Pedeferri [9], as one of the beneficial secondary effects of CP, as the polarity of the electric field induces a repellent effect of the negative ions, thus reducing the chloride uptake by concrete. The effect can be quantified by using a Cl^- barrier effect parameter

Table 4
Final averaged chloride contents (expressed in % Cl^- relative to cement mass) at the end of the 24 weeks of exposure to a severe Cl^- load (first phase of CP and CPre treatments).

Specimen	Initial Cl^- content (% ref. cem. mass)	Electrochemical treatment previous to the 24 weeks first phase	Electrochemical treatment during the 24 weeks first phase	Final averaged[a] Cl^- content (% ref. cem. mass)
P	0	–	–	4.93
R	2	–	–	6.08
ER	2	ECE	–	4.26
A	2	–	CP	5.39
B	0	–	CPre	3.94
EA	2	ECE	CP	3.41
EB	2	ECE	CPre	3.42

[a] The final Cl^- content was calculated as the mean value of those found in the Cl^- content profile determined through the concrete cover zone (20 mm width).

(Cl^- BEP), which is defined here as the percentage of reduction of the Cl^- uptake by concrete, due to CP or CPre actions, referred to the Cl^- uptake of the reference, (not treated) specimens, see Eq. (1).

$$Cl^- BEP = \frac{(Cl^- Uptake\ by\ Reference) - (Cl^- Uptake\ by\ Treated\ Specimen)}{(Cl^- Uptake\ by\ Reference)} * 100 \quad (1)$$

Table 5 shows the net values of the Cl^- barrier effect parameter found for the specimens tested in this work, putting in evidence that this parameter reaches values of about 20% in the experimental conditions of this work.

3.3. Second phase of CP treatments

Given that after the 24 weeks of treatments of Phase 1, including rest periods between the 13th and 17th weeks, the steel reinforcements in all concrete specimens had completely lost their protection conditions, and having been demonstrated that a CP of 15 mA/m^2 was unable to restore the protective conditions (Fig. 4), the Phase 2 was started. The external Cl^- load was discontinued since all the specimens had reached very high Cl^- contents, see Table 4. In these conditions, CP was applied with higher current densities. The question was if it would be possible to recover the protection conditions of steel by increasing the current density to the appropriate value. In the beginning of this last phase, the current density was set at 20 mA/m^2. After 4 weeks in operation the threshold value of 100 mV ΔE_{decay} was not reached, i.e. the protection conditions were not obtained, Fig. 6. Neither success was obtained in a second attempt at 25 mA/m^2 (data not shown in Fig. 6). Finally, a third step of 40 mA/m^2 was set. In this case, after 4 weeks, the rule of 100 mV of ΔE_{decay} was achieved for EA, A and B specimens.

Table 5
Values of the chloride barrier effect parameter for the tested specimens.

Specimen	Treatment of specimen	Reference	Treatment of reference	Cl^- BEP (%)
A	CP	R	None	17.0
B	CPre	P	None	21.0
EA	ECE + CP	ER	ECE	26.0
EB	ECE + CPre	ER	ECE	25.7

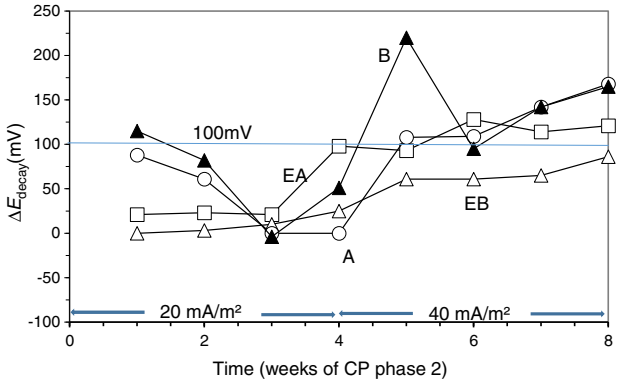

Figure 6. Evolution of ΔE_{decay} during Phase 2 of CP. First step of 4 weeks with 20 mA/m^2 of current density, and third step with 40 mA/m^2. Specimens A, B, EA and EB.
Adapted from [24].

Moreover, protection conditions were verified with the measurement of depolarization potential difference values 7 days after switch off [39]. In fact, more than 150 mV of ΔE_{decay} was reached after 7 days (209 mV for EA, 211 mV for A and 153 mV for B). This efficiency of CP is similar to that obtained by other researchers [40,43]. However, this was not the case for EB. After 4 weeks with a cathodic current density of 40 mA/m^2 the protection conditions were not recovered for this latter specimen.

4. Conclusions

The results of this work point out that it is possible to use a graphite–cement paste, overlaid on the surface of a reinforced concrete element, as the anode for successive treatments of electrochemical chloride extraction, to reduce the chloride content, and then cathodic protection to maintain protective conditions for the steel reinforcement. The following aspects can be emphasized, namely:

- The application of ECE, in the experimental conditions of this work, does not seem to produce damage of the GCP anodes, which could impair the performance of the anodic system in the posterior continuous CP treatment.

- The chloride barrier effect parameter (Cl^- BEP) is defined as the percentage of reduction of the Cl^- uptake by concrete, due to CP or CPre actions, referred to the Cl^- uptake of the reference (not treated) specimens. This parameter allows evaluating the magnitude of the chloride barrier effect due to the application of CP or CPre to reinforced concrete elements continuously exposed to a harsh chloride environment. The found values of this parameter, both for simple CP or CPre trials and for the combined treatments of ECE + CP, are about 20%, in the experimental conditions of this work.
- A cathodic current density of 2 mA/m^2, typical of CPre applications, is unable to protect steel after an ECE treatment.
- It is possible to recover protective conditions against corrosion of steel reinforcement in concrete by applying a combined treatment of ECE followed by a continuous CP treatment. The current density value of the CP step must be set at the proper value, according to the residual chloride content in concrete. The needed CP current density value will be lower than if the ECE was not applied, thus reducing the risk of damage of the anode. In this sense the GCP overlays on concrete may show an advantageous versatility, over other types of anodic systems, since the same anode is used on the two steps of the combined treatment.

Acknowledgements

This research was funded by the Spanish Agencia Estatal de Investigación (AEI), and Fondo Europeo de Desarrollo Regional (FEDER) through project BIA2016-80982-R. We acknowledge also funding from the Spanish Ministerio de Ciencia e Innovación (MAT2009-10866), and Generalitat Valenciana (PROMETEO/2013/035).

The authors would like to dedicate this work to honour our master and friend Prof. Carmen Andrade Pérdrix, who suggested our research group undertaking research on the application of electrochemical techniques to reinforced concrete structures.

References

[1] C.L. Page, Interfacial effects of electrochemical protection method applied to steel in chloride containing concrete, in: D.W.S. Ho, F. Collins (Eds.), Proceedings of the International RILEM/CSIRO/ACRA Conference on Rehabilitation of Concrete Structures, Melbourne, Australia 1992, RILEM, Melbourne, Australia, 1992, pp. 179–187.

[2] J. Mietz, Electrochemical rehabilitation methods for reinforced concrete structures: a state of the art report, in: Publication Number 24 of the European Federation of Corrosion, IOM Communications Ltd, London, UK, 1998, pp. 57.

[3] C. Andrade, M. Castellote, C. Alonso, An overview of electrochemical realkalisation and chloride extraction, in: D.W.S. Ho, I. Godson, F. Collins (Eds.), Rehabilitation of Structures, Proceedings of 2nd International RILEM/CSIRO/ACRA Conference, Melbourne, Australia, 21–23 September 1998, RILEM, Melbourne, Australia, 1998, pp. 1–12.

[4] J. Tritthart, Electrochemical Chloride Removal: An Overview and Scientific Aspects, The American Ceramic Society, Westerville, OH, USA, 1998, pp. 401–441.

[5] P. Pedeferri, L. Bertolini, Tecniche elettrochimiche (Electrochemical techniques), in: La Durabilità del Calcestruzzo Armato (The Durability of Reinforced Concrete), McGraw-Hill, Milano, Italy, 2000, pp. 253–273 (in Italian).

[6] L. Bertolini, B. Elsener, P. Pedeferri, R.B. Polder, Electrochemical techniques, in: Corrosion of Steel in Concrete, Wiley-VCH, Weinheim, Germany, 2004, pp. 345–374.

[7] R.B. Polder, Electrochemical techniques for corrosion protection and maintenance, in: H. Böhni (Ed.), Corrosion in Reinforced Concrete Structures, Woodhead Publishing, Cambridge, UK, 2005, pp. 215–241.

[8] C.L. Page, Cathodic protection of reinforced concrete. Principles and applications, in: Proceedings of the International Conference on Repair of Concrete Structures, Svolvaer, Norway, 1997, pp. 123–132.

[9] P. Pedeferri, Cathodic protection and cathodic prevention, Constr. Build. Mater. 10 (1996) 391–402.

[10] R.B. Polder, Cathodic protection of reinforced-concrete structures in The Netherlands – experience and developments, Heron 43 (1) (1998) 3–14.

[11] L. Bertolini, F. Bolzoni, P. Pedeferri, L. Lazzari, T. Pastore, Cathodic protection and cathodic prevention in concrete principles and applications, J. Appl. Electrochem. 28 (1998) 1321–1331.

[12] G.K. Glass, J.R. Chadwick, An investigation into the mechanisms of protection afforded by a cathodic current and the implications for advances in the field of cathodic protection, Corros. Sci. 36 (1994) 2193–2209.

[13] J.E. Slater, D.R. Lankard, P.J. Moreland, Electrochemical removal of chlorides from concrete bridge decks, Mater. Perform. 15 (1976) 21–26.

[14] Ø. Vennesland, O.A. Opsahl, A.P. Russell-Rayner, Removal of chlorides from concrete. European Patent Application number 86302888.2. Publication number 0 200 428, 1986.

[15] I.L.H. Hansson, C.M. Hansson, Electrochemical extraction of chlorides from concrete. Part I – A qualitative model of the process, Cem. Concr. Res. 23 (5) (1993) 1141–1152.

[16] B. Elsener, M. Molina, H. Böhni, The electrochemical removal of chlorides from reinforced concrete, Corros. Sci. 35 (1993) 1563–1570.

[17] P. Garcés, M.J. Sánchez de Rojas, M.A. Climent, Effect of the reinforcement bar arrangement on the efficiency of electrochemical chloride removal technique applied to the reinforced concrete structures, Corros. Sci. 48 (2006) 531–545.

[18] M.J. Sánchez de Rojas, P. Garcés, M.A. Climent, Electrochemical extraction of chlorides from reinforced concrete: variables affecting treatment efficiency, Mater. Constr. 56 (284) (2006) 17–26.

[19] R.B. Polder, H.J. Van der Hondel, Electrochemical realkalization and chloride removal of concrete, in: D.W.S. Ho, F. Collins (Eds.), Proceedings of the International RILEM/CSIRO/ACRA Conference on Rehabilitation of Concrete Structures, Melbourne, Australia, 1992, RILEM, Melbourne, Australia, 1992, pp. 135–147.

[20] G. Sergi, R.I. Walker, C.L. Page, Mechanism and criteria for the realkalisation of concrete, in: C.L. Page, P.B. Bamforth, J.W. Figg (Eds.), Corrosion of Reinforcement in Concrete Constructions, Royal Society of Chemistry, Cambridge, UK, 1996, pp. 491–500.

[21] L. Bertolini, F. Bolzoni, T. Pastore, P. Pedeferri, Effectiveness of a conductive cementitious mortar anode for cathodic protection of steel in concrete, Cem. Concr. Res. 34 (4) (2004) 681–694.

[22] L. Westhof, Field experience with a conductive cement-based composite as anode for the cathodic protection of reinforced concrete structures, in: M.G. Grantham, R. Jaubertie, C. Lanos (Eds.), Proceedings of the 2nd International Conference on Concrete Solutions, BRE Press, Watford, UK, 2006, pp. 400–409.

[23] J. Xu, W. Yao, Current distribution in reinforced concrete cathodic protection system with conductive mortar overlay anode, Constr. Build. Mater. 23 (6) (2009) 2220–2226.

[24] J. Carmona, P. Garcés, M.A. Climent, Efficiency of a conductive cement-based anodic system for the application of cathodic protection, cathodic prevention and electrochemical chloride extraction to control corrosion in reinforced concrete structures, Corros. Sci. 96 (2015) 102–111.

[25] M.A. Climent, M.J. Sánchez de Rojas, G. de Vera, P. Garcés, Effect of type of anodic arrangements on efficiency of electrochemical chloride removal from concrete, ACI Mater. J. 103 (4) (2006) 243–250.

[26] A. Pérez, M.A. Climent, P. Garcés, Electrochemical extraction of chlorides from reinforced concrete using a conductive cement paste as the anode, Corros. Sci. 52 (2010) 1576–1581.

[27] A. Cañón, P. Garcés, M.A. Climent, J. Carmona, E. Zornoza, Feasibility of electrochemical chloride extraction from structural reinforced concrete using a sprayed conductive graphite powder–cement as anode, Corros. Sci. 77 (2013) 128–134.
[28] B. del Moral, O. Galao, C. Antón, M.A. Climent, P. Garcés, Usability of cement paste containing carbon nanofibres as an anode in electrochemical chloride extraction from concrete, Mater. Constr. 63 (309) (2013) 39–48.
[29] J. Carmona, M.A. Climent, C. Antón, G. de Vera, P. Garcés, Shape effect of electrochemical chloride extraction in structural reinforced concrete elements using a new cement-based anodic system, Materials 8 (2015) 2901–2917.
[30] M.A. Climent, J. Carmona, P. Garcés, Graphite–cement paste: a new coating of reinforced concrete structural elements for the application of electrochemical anti-corrosion treatments, Coatings 6 (2016) 32.
[31] J. Carmona Calero, M.A. Climent Llorca, P. Garcés Terradillos, Influence of different ways of chloride contamination on the efficiency of cathodic protection applied on structural reinforced concrete elements, J. Electroanal. Chem. 793 (2017) 8–17.
[32] U NE EN 12390-3:2009 Ensayos de Hormigón Endurecido. Parte 3: Determinación de la Resistencia a Compresión de Probetas (Testing Hardened Concrete – Part 3: Compressive Strength of Test Specimens), Asociación Española de Normalización y Certificación (AENOR), Madrid, Spain, 2009 (in Spanish).
[33] UNE 83980:2014 Durabilidad del Hormigón. Métodos de Ensayo. Determinación de la Absorción de Agua, la Densidad y la Porosidad Accesible al Agua del Hormigón (Concrete Durability. Test Methods. Determination of the Water Absorption, Density and Accessible Porosity for Water in Concrete), Asociación Española de Normalización y Certificación (AENOR), Madrid, Spain, 2014 (in Spanish).
[34] UNE EN 12390-7:2009 Ensayos de Hormigón Endurecido. Parte 7: Densidad del Hormigón Endurecido (Testing Hardened Concrete – Part 7: Density of Hardened Concrete), Asociación Española de Normalización y Certificación (AENOR), Madrid, Spain, 2009 (in Spanish).
[35] O. Galao, F.J. Baeza, E. Zornoza, P. Garcés, Strain and damage sensing properties on multifunctional cement composites with CNF, Cem. Concr. Comp. 46 (2014) 90–98.
[36] Ø. Vennesland, M.A. Climent, C. Andrade, Recommendation of RILEM TC 178-TMC: testing and modelling chloride penetration in concrete, Methods for obtaining dust samples by means of grinding concrete in order to determine the chloride concentration profile, Mater. Struct. 46 (2013) 337–344.
[37] M.A. Climent, E. Viqueira, G. de Vera, M.M. López, Analysis of acid-soluble chloride in cement, mortar and concrete by potentiometric titration without filtration steps, Cem. Concr. Res. 29 (1999) 893–898.
[38] M.A. Climent, G. de Vera, E. Viqueira, M.M. López, Generalization of the possibility of eliminating the filtration step in the determination of acid-soluble chloride content in cement and concrete by potentiometric titration, Cem. Concr. Res. 34 (2004) 2291–2300.
[39] ISO 12696: 2012(en) Cathodic Protection of Steel in Concrete, ISO, Geneva, Switzerland, 2012.
[40] G.K. Glass, A.M. Hassanein, N.R. Buenfeld, Cathodic protection afforded by an intermittent current applied to reinforced concrete, Corros. Sci. 43 (2001) 1111–1131.
[41] Y. Liu, X. Shi, Modeling cathodic prevention for unconventional concrete in salt-laden environment, Anti-Corros. Methods Mater. 59 (2012) 121–131.
[42] M. Dugarte, A.A. Sagüés, K. Williams, Cathodic prevention for reinforcing steel in cracked concrete of chloride contaminated structures, in: Proceedings of CORROSION 2015 Conference, NACE-2015-6102, Houston, TX, USA, 15–19 March 2015, NACE International, Houston, TX, USA, 2015, p. 11.
[43] C. Christodoulou, G.K. Glass, J. Webb, S. Austin, C. Goodier, Assessing the long term benefits of impressed current cathodic protection, Corros. Sci. 52 (2010) 2671–2679.

ACHE

SECRETARÍA DE ACHE - Tel.: 91 336 66 98

www. e-ache.com

ACHE
www.e-ache.com

Disponible en
ScienceDirect
www.sciencedirect.com

Hormigón y Acero 2019; 69(S1):53–69

HORMIGÓN y ACERO
www.elsevierciencia.com/hya

Predicción de fracturas en estructuras de hormigón combinando los métodos de elementos finitos y de elementos discretos

Fractures prediction in concrete structures combining the finite and discrete element methods

Francisco Zárate [a,b,*] y Eugenio Oñate [a,b]

[a] *Centre Internacional de Mètodes Numèrics en Enginyeria (CIMNE) , Barcelona, España*
[b] *Universitat Politècnica de Catalunya (UPC), Barcelona, España*

Recibido el 8 de enero de 2018; aceptado el 17 de mayo de 2018
Disponible en Internet el 17 de julio de 2018

Resumen

El presente trabajo plantea los conceptos básicos y de aplicación de la estrategia que combina los métodos de elementos finitos y de elementos discretos para el estudio de la propagación de fracturas en estructuras de hormigón. El cálculo de la estructura, modelada como un continuo, se inicia con los métodos de elementos finitos y se hace uso de los métodos de elementos discretos para iniciar y hacer crecer las grietas que puedan aparecer en la estructura. Esta metodología ha sido propuesta por los autores en 2 y 3 dimensiones. Recientemente se ha agregado el uso de elementos unidimensionales de acero embebidos en el continuo para modelar el efecto resistente del armado en estructuras de hormigón. En el trabajo se presentan diferentes ejemplos de aplicación al estudio de la rotura de piezas y estructuras de hormigón en masa y armado, así como la rotura múltiple de una estructura histórica de mampostería debida a un terremoto.

Palabras clave: Método de elementos discretos; Método de elementos finitos; Mecánica de fractura; Estrategia elementos finitos-discretos

Abstract

This paper presents the basic concepts and application of the strategy that combines finite element methods (FEM) and discrete elements (DEM) for the study of the propagation of fractures in concrete structures. The calculation of the structure, modeled as a continuum, begins with the FEM and the DEM is used to start and grow the cracks that may appear in the structure. This methodology has been proposed by the authors in two and three dimensions. Recently, the use of one-dimensional steel elements embedded in the continuum has been added to model the reinforcement in concrete structures. The work presents different examples of application to the study of the breakage of parts and structures of concrete in mass and armed, as well as the multiple breakage of a historic structure of masonry due to an earthquake.

Keywords: Finite element method; Discrete element method; Fracture mechanics; Finite-discrete element strategy

1. Introducción

Recientemente muchos autores han realizado interesantes desarrollos con la finalidad de poder definir el inicio y crecimiento de una fractura dentro de una estructura, modelada como un medio continuo, ya sea frágil o dúctil [1–4].

Uno de los trabajos más recientes discretiza el medio continuo por medio de elementos discretos de forma circular (en 2 dimensiones) o esférica (en 3 dimensiones) [5]. Sin embargo, la dificultad inherente para calibrar los parámetros del material en el método de los elementos discretos (DEM, por sus siglas en inglés), así como la necesidad de contar con un gran número de

* Autor para correspondencia.
Correo electrónico: zarate@cimne.upc.edu (F. Zárate).

https://doi.org/10.1016/j.hya.2018.05.002

elementos discretos [2,5], pone en duda su efectividad, a pesar de que cualitativamente el número y dirección de las grietas y los resultados numéricos obtenidos de la carga última de la estructura son bastante aceptables.

Este trabajo hace uso de una estrategia que utiliza el método de elementos finitos (FEM, por sus siglas en inglés) para discretizar la estructura inicial y seguir su comportamiento bajo cargas crecientes hasta el inicio de la primera fisura. Tras ello se utiliza una técnica de eliminación de los elementos finitos dañados y se introducen elementos discretos en los labios de las fisuras [6–8]. La denominada técnica FEM-DEM se ha utilizado con éxito en 2 y 3 dimensiones [9,10] para estudiar el comportamiento no lineal y el fallo de estructuras de hormigón y mampostería bajo diferentes solicitaciones cuasi-estáticas y dinámicas.

Otros aspectos importantes inherentes a la formulación FEM-DEM son el uso de un campo de esfuerzos suavizado, la conservación de la masa y el uso de un algoritmo simple para asegurar el contacto posfractura entre las paredes de la grieta. Adicionalmente, la armadura de acero se considera embebida en la malla de elementos finitos, lo cual simplifica los cálculos.

2. Formulación método de elementos finitos-método de elementos discretos

En general la estrategia que se sigue para el cálculo no lineal de estructuras con modelos de elementos finitos de sólido bidimensionales (2D) o tridimensionales (3D) [11] pasa para evaluar a lo largo del tiempo la respuesta de la estructura discretizada con una malla de elementos finitos. En dicha malla las conectividades interelementales emulan los enlaces entre los elementos que se degradan de forma progresiva, generalmente mediante un sencillo modelo de daño isótropo. Dichos enlaces interelementales pueden interpretarse como las conexiones entre una colección de elementos discretos que reemplazarían los nodos de la malla de elementos finitos. Esta analogía es el punto de partida de la técnica FEM-DEM [9,10].

La estrategia FEM-DEM se puede resumir en los 5 pasos siguientes:

- Discretización del continuo que modela la estructura mediante el FEM.
- Obtención del campo de tensiones sobre la estructura.
- Obtención del daño en el interior y los lados de los elementos.
- Discretización mediante el DEM.
- Integración temporal en subpasos.

Debido a la naturaleza de los ejemplos se describirán los pasos anteriores enfocados al caso 3D, utilizando tetraedros lineales de 4 nodos para la discretización con el FEM.

Una de las claves de la técnica FEM-DEM es el procedimiento para pasar el daño producido en un elemento finito, con la consiguiente degradación de la rigidez elemental, a una discretización de los labios de la fisura por elementos discretos de forma circular (en 2D) o esférica (en 3D).

Cuando el daño que se induce en un elemento es mayor que un cierto valor se considera que la rigidez del elemento se encuentra tan disminuida que es posible eliminarlo; para ello se utiliza una técnica de eliminación de elementos [6–8]. En ese momento se crean nuevos elementos discretos en los vértices del tetraedro eliminado (en 3D), lo que permite la apertura de la grieta en el continuo discretizado por los elementos finitos, mientras que los labios de la fisura quedan definidos por los elementos discretos. A medida que la fisura crece, e incluso se ramifica, algunos elementos discretos pueden separarse de la malla de elementos finitos creando una disgregación del continuo. El hecho de utilizar elementos discretos para definir las grietas permite, de manera natural, considerar la apertura y cierre de estas sin añadir procedimientos adicionales.

3. Discretización mediante el método de elementos finitos

El FEM es probablemente la técnica numérica más popular para modelar el inicio y la propagación de fisuras en materiales friccionales (hormigón, rocas, mampostería, cerámicas, etc.) [12–16]. Sin embargo, la mayoría de los procedimientos basados en el FEM para la predicción de la aparición y evolución de grietas utilizan formulaciones de elementos muy sofisticadas, que en ocasiones requieren un remallado en la vecindad de las posibles grietas [15,16]. El enfoque seguido en este trabajo utiliza el FEM para modelar la estructura mediante elementos de sólido (2D o 3D), cuya eventual fractura se describe mediante el DEM. En trabajos previos de la técnica FEM-DEM hemos utilizado el sencillo triángulo de 3 nodos en 2D y el tetraedro de 4 nodos en 3D [9,10].

Considerando, por ejemplo, el caso 3D, inicialmente todo el dominio de la estructura se discretiza con una malla de tetraedros, como en cualquier análisis lineal 3D por el FEM. La no linealidad se modela introduciendo una degradación de la rigidez elemental mediante la clásica teoría de daño isótropo [13,17].

El efecto resistente de la armadura de acero se modela mediante elementos unidimensionales (1D) embebidos en la malla de tetraedros. Ello implica localizar los puntos de intersección entre los elementos 1D que modelan el acero y todos los tetraedros que discretizan el dominio. Para cada tetraedro intersectado se determinan los puntos de intersección, los cuales corresponden a los nodos del segmento de la armadura embebida en el tetraedro. Como es posible describir el desplazamiento de dichos nodos en función de los nodos del tetraedro, la matriz de rigidez del elemento 1D de acero es función de dichos desplazamientos.

Esta técnica no incrementa el número de ecuaciones a resolver y permite de una forma muy sencilla tomar en cuenta la rigidez asociada a la armadura.

3.1. Definición del campo de tensiones

El considerar un campo de tensiones adecuado es fundamental para poder definir correctamente el nivel del daño en la estructura y la trayectoria de las fisuras. Dado que en el FEM las tensiones entre elementos son discontinuas [11], es esencial realizar un alisado de las mismas para obtener un campo continuo de las tensiones entre elementos. En problemas 2D se obtiene un campo de tensiones continuo alisando los valores de

las tensiones, calculadas inicialmente en el baricentro de cada elemento, para obtener su valor el centro de los lados de cada elemento. Esta estrategia corresponde al método de la parcela superconvergente propuesta por Zienkiewicz y Zhu [18], y evita agregar términos de estabilización al campo de tensiones como es necesario en otros procedimientos alternativos [12–14].

En análisis 3D se procede de manera similar, ya que el campo de tensiones entre elementos es discontinuo, por lo que se utiliza el mismo mecanismo de suavizado. Es decir, las tensiones en cada una de las aristas de un elemento tetraédrico es la media aritmética de las tensiones evaluadas dentro de todos los elementos que comparten dicha arista.

Al igual que en el caso 2D [9], se ha utilizado el criterio de fallo de Rankin para definir el inicio de una fractura en materiales frágiles tomando en cuenta la tensión principal mayor σ_l [13,17]. El crecimiento del daño se realiza mediante la siguiente ley exponencial que degrada progresivamente la rigidez del material [19].

$$d = 1 - \frac{\sigma f}{\sigma 1} \exp\left[A\left(1 - \frac{\sigma 1}{\sigma f}\right)\right] \; con \; A = \left[\frac{G E_0}{l \sigma_f^2} - \frac{1}{2}\right]^{-1} \quad (1)$$

donde l es la longitud de la arista del elemento finito dañado, σf es el límite elástico a tracción del material, G la energía de fractura y E_0 el módulo de Young del material no dañado. Resulta obvio que entre 2 pasos de tiempo el daño de un lado o una arista no puede disminuir, ya que ello implicaría la reparación espontánea del material, lo cual es termodinámicamente inadmisible.

3.2. Definición del daño elemental

Una vez que el daño ha sido evaluado en cada lado o arista de un elemento (es decir, un enlace virtual entre elementos discretos) el daño sobre el conjunto del elemento se calcula como el máximo daño existente en todos los planos que cortan un triángulo (2D) o un tetraedro (3D) (fig. 1). En cada tetraedro existen 4 planos de corte que aíslan un vértice (fig. 1 b) y otros 3 que aíslan 2 vértices (fig. 1 c). De esta manera, el daño sobre el plano de corte se define como el valor medio del daño de cada arista del elemento que corta dicho plano.

Si el daño elemental sobrepasa un cierto umbral entonces se elimina el triángulo o tetraedro de la malla [6–8] y se crean nuevos elementos discretos en los vértices. El tamaño de estos elementos discretos se define de manera que se conserve la masa del elemento eliminado.

4. Discretización mediante método de elementos discretos

Cuando un tetraedro es totalmente eliminado (*i.e.* su rigidez es despreciable) se crean 4 nuevos elementos discretos en los vértices de dicho elemento finito. La creación de dichos elementos discretos queda condicionada a que no hayan sido creados con anterioridad debido a la eliminación de algún elemento finito vecino. En este trabajo se han utilizado círculos y esferas para representar los elementos discretos en 2D y 3D, respectivamente. La masa de cada elemento discreto corresponde a la masa nodal que es compatible con la obtenida mediante elementos finitos. El radio de un nuevo elemento discreto esférico se obtiene de tal manera que sea el máximo que garantice el contacto con las esferas vecinas, pero sin crear solapamientos. Existen otros algoritmos para generar elementos discretos [2,20], sin embargo, el propuesto, a pesar de su simplicidad, ha dado buenos resultados.

Una vez que se crea un elemento discreto las fuerzas en las interfaces de contacto se usan para definir la interacción de dicho elemento con los adyacentes. Estas fuerzas se deben únicamente a un mecanismo de contacto en las direcciones normal y tangencial al plano de contacto entre esferas (en 3D), considerando el radio mínimo entre las 2 partículas en contacto [5].

En problemas 3D la fuerza normal de contacto se genera en el punto de contacto entre 2 esferas y viene dada por:

$$F_n^{ij} = \frac{A^{ij}}{d_{ij}} E_0 u_n \; con \; A^{ij} = \pi r_c^2 \quad (2)$$

donde A^{ij} es el área de la superficie de contacto entre las 2 esferas, r_c es el radio de la menor de las 2 esferas que interactúan en la interfaz $i\,j$; u_n es el solapamiento en la dirección de los centros de las dos esferas y d_{ij} es la distancia entre dichos centros [5].

La fuerza tangencial F_s en el punto de contacto se descompone en 2 direcciones ortogonales s_1 y s_2 contenidas en el plano normal a la dirección d^{ij}. Para cada dirección s_j la fuerza tangencial se describe por:

$$F_S = \min \begin{cases} u_{si} \frac{E_0}{2(1+u)} \\ \mu_n^F \left(\frac{u_{si}}{u_s}\right) \end{cases} \quad (3)$$

donde μ es el coeficiente de rozamiento entre esferas y u es el coeficiente de Poisson. Más detalles de las ecuaciones (2) y (3) se pueden encontrar en Oñate et al. [5].

En general, el número total de elementos discretos generados en un análisis es solo una pequeña fracción del número total de nodos en la malla de elementos finitos [10]. Por lo tanto, los algoritmos de búsqueda para localizar las fuerzas de contacto entre elementos discretos solo representan un pequeño porcentaje del tiempo total de cálculo.

Es importante mencionar que la estrategia del uso de elementos discretos para definir el contacto entre los labios de una fisura permite resolver problemas estructurales en donde existe apertura y cierre de múltiples grietas, como se muestra en el análisis sísmico de un edificio histórico de mampostería, presentado al final de este artículo.

5. Integración temporal en subpasos

Uno de los principales problemas en el análisis 3D en el tiempo es el gran número de ecuaciones que surgen de la discretización. Sumando a estos la dificultad para considerar un gran período de tiempo, se concluye que en problemas dinámicos la integración implícita en el tiempo es la mejor estrategia de solución. Sin embargo, este tipo de integraciones son complejas de utilizar en el DEM debido a que es imposible identificar y

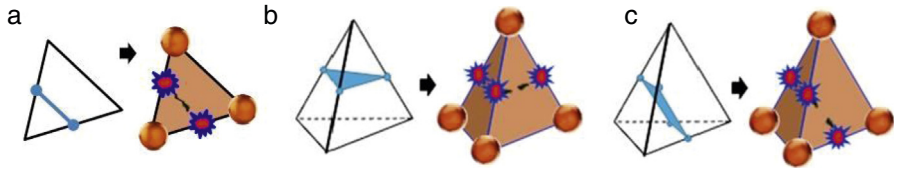

Figura 1. Planos de corte. a) Elemento triangular; b) tetraedro aislando un vértice; c) tetraedro aislando 2 vértices.

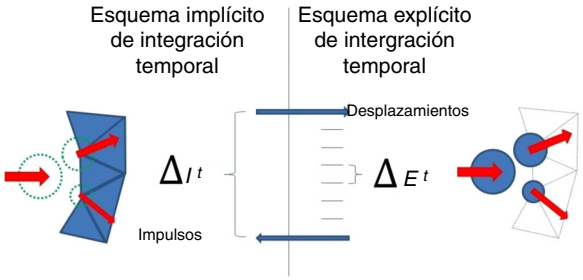

Figura 2. Integración temporal en subetapas utilizado para el análisis conjunto de elementos finitos y discretos.

cuantificar correctamente los contactos y las fuerzas de contacto entre elementos discretos.

La implementación para el estudio de problemas transitorios seguida en esta investigación corresponde a un esquema de integración temporal de subetapas en el cual los elementos finitos se calculan mediante un esquema implícito de Newmark, y los elementos discretos mediante un esquema explícito de diferencias centradas. Normalmente el incremento de tiempo del esquema implícito suele ser 100 veces mayor que el explícito.

La ventaja de esta estrategia es que el número de elementos discretos suele ser mucho menor que el de elementos finitos que discretizan la estructura, por lo que la integración explícita realizada dentro de un paso de tiempo implícito es bastante rápida. Antes de comenzar un nuevo paso de tiempo $\Delta_i t$ en el esquema implícito, se calcula el mismo período de tiempo con un esquema explícito sobre los elementos discretos, usando un incremento de tiempo $\Delta_E t$.

El contacto entre elementos discretos se cuantifica por la suma de los impulsos que se producen a lo largo del análisis explícito, y se expresa como una fuerza sobre los elementos discretos, aplicada en el tiempo $t+1$ correspondiente al esquema implícito, tal como se muestra en la figura 2.

Se ha observado que no es aconsejable que los intervalos de tiempo $\Delta_i t$ y $\Delta_E t$ tengan una relación mayor que 1: 500, ya que puede haber discrepancias entre la solución explícita y la implícita. Teniendo esto en cuenta, la estrategia de solución en subpasos implementada permite obtener excelentes resultados, como se muestra en los ejemplos del siguiente apartado.

6. Ejemplos

En este apartado se exponen varios ejemplos a fin de mostrar el buen comportamiento de la estrategia FEM-DEM descrita. El primer ejemplo corresponde al estudio 3D de una probeta normalizada en un ensayo a tracción. El segundo ejemplo es una viga de hormigón bientallada donde predomina la fractura

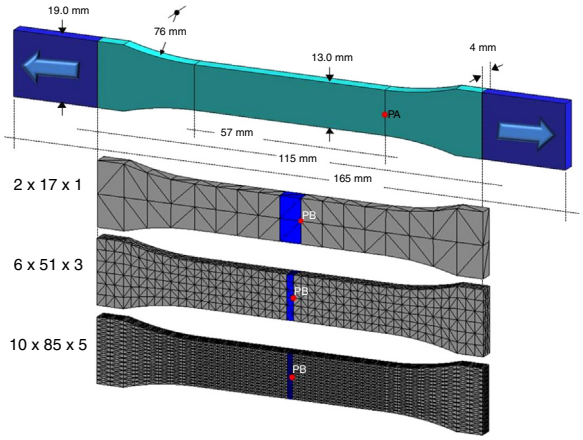

Figura 3. Ensayo normalizado 3D de tracción. Malla de elementos finitos y dimensiones según la norma ASTMD638.

en modo mixto. El tercer ejemplo corresponde al ensayo de tracción indirecta, ampliamente usado en mecánica de rocas. El cuarto ejemplo consiste en un ensayo de cortante en hormigón propuesto por Luong [21]. El quinto ejemplo es un ensayo de una probeta a compresión simple. El sexto ejemplo es el estudio de un forjado reticular de hormigón armado, afectado por un asentamiento diferencial. El acero se considera embebido y solidario con los desplazamientos de los elementos finitos utilizados.

Finalmente, en el sexto ejemplo, se presenta el análisis sísmico de la nave central de la iglesia del monasterio de Poblet, formada por elementos de mampostería, aplicándole un sismo de 6 M_w. En este ejemplo se puede observar como la estrategia FEM-DEM modela el efecto de la apertura y cierre de múltiples grietas.

6.1. Ensayo normalizado de tracción

El primer ejemplo corresponde al análisis de fractura de una probeta de hormigón sujeta a fuerzas de tracción. El objetivo principal es mostrar la independencia del tamaño de la malla en la generación de la grieta, de manera que la energía utilizada en la fractura sea independiente del tamaño elemental. La geometría se define de acuerdo con la norma D638 de la Sección Norteamericana de la Asociación Internacional de Ensayo de Materiales *(American Society for Testing and Materials)* [22]. En la figura 3 se muestran las 3 mallas de elementos tetraédricos de 4 nodos utilizadas, así como las condiciones de contorno. La probeta se carga imponiendo un campo de velocidad constante de tracción en sus extremos, representados por la zona oscura en la figura.

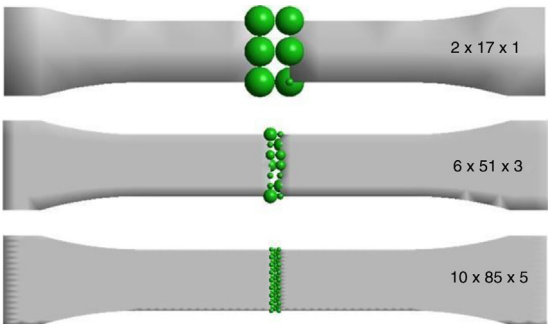

Figura 4. Ensayo normalizado de tracción. Zona agrietada incluyendo los elementos discretos generados para las 3 mallas de elementos finitos consideradas.

El estudio se ha realizado utilizando la metodología FEM-DEM en 3D antes descrita. Con el fin de localizar la fractura, solo se permite que una banda de elementos se rompa al nivel de la tensión de fallo, usando el modelo de daño mencionado. Los resultados obtenidos se analizan dibujando los desplazamientos de los puntos PA y PB mostrados en la figura 3.

El módulo de Young, el coeficiente de Poisson y la densidad son respectivamente $M_w = 30 \times 10^9$ Pa, $\upsilon = 0{,}2$, $y = 1{,}0 \times 10^3$ N/m^3, la tensión máxima de tracción $\sigma_f = 10 \times 10^3$ Pa y la energía de fractura $G = 7{,}5 \times 10^{-3}$ J/m^2.

La probeta se deforma aplicando una velocidad constante de tracción de $0{,}5 \times 10^{-7}$ m/s en ambos extremos. La figura 4 muestra la geometría dañada para las 3 mallas del FEM consideradas.

Obsérvese que cuando se produce una fractura se crean elementos discretos en los labios de la única fisura que aparece en este ejemplo, como se explica en los apartados anteriores. El tamaño de las esferas no es uniforme debido a que no todos los elementos llegan al daño máximo de manera simultánea.

Con objeto de evaluar la apertura de la grieta se analiza el desplazamiento de los puntos PA y PB situados a la derecha y en el centro de la probeta, respectivamente (fig. 3). La figura 5 muestra la relación carga-desplazamiento en estos puntos. Para las 3 mallas consideradas la evolución del desplazamiento es muy similar, y de acuerdo con los resultados esperados [9]. Debido a que los elementos por donde se abre la grieta tienen un tamaño diferente para cada malla, el desplazamiento del punto PB en la región elástica se hace más pequeño a medida que se reduce el tamaño del elemento.

6.2. *Viga bientallada a flexión*

El siguiente ejemplo corresponde al ensayo de una viga de hormigón en masa bientallada. El análisis se realiza mediante las hipótesis de tensión plana y es un buen ejemplo de fractura en modo mixto. La viga se sostiene en 2 puntos y se somete a flexión aplicando un desplazamiento impuesto mediante control de velocidad equivalente a 1 mm/s en los 2 puntos representados en la figura 6. Igualmente, en dicha figura también se muestran la geometría y las dimensiones de la probeta.

La viga presenta 2 puntos singulares en la punta de las 2 entallas, en donde las tensiones de tracción son altas y el daño comienza en esta zona. Las propiedades del material son $E_0 = 30 \times 10^9$ Pa, $\upsilon = 0{,}2$, $\sigma_f = 2$ MPa y $G = 1 \times 10^2$ J/m^2. El problema ha sido resuelto con la técnica FEM-DEM en 2D.

En la figura 7 se muestra un detalle de las 3 diferentes mallas utilizadas, formadas por 1.165 nodos y 2.202 elementos triangulares lineales para la malla gruesa, 1.847 nodos y 3.480 elementos para la malla intermedia y 5.747 nodos y 11.206 elementos para la malla fina. El análisis se ha realizado tanto de forma cuasiestática como de forma dinámica, respetando la velocidad de aplicación de la carga. En ambos casos los resultados han sido muy similares, como se observa en la figura 8.

La figura 9 muestra la dirección de las fisuras para las 3 mallas analizadas, las cuales coinciden con los experimentos numéricos [14]. La figura 8 muestra la relación entre la reacción y el desplazamiento impuesto en cualquiera de los 2 puntos representados en la figura 6 (los resultados son idénticos para los 2 puntos). Los gráficos son concordantes con los resultados obtenidos por Cervera et al. [14].

6.3. *Ensayo de tracción indirecta*

El ensayo brasileño de tracción indirecta *(Brazilian Tensile Strength)* es un procedimiento sencillo para evaluar la resistencia a la tracción de hormigón y geomateriales. La probeta de hormigón analizada es un cilindro de,2 m de diámetro (D) y 0,1 m de espesor (t), sujeto a una carga diametralmente opuesta (fig. 10). El valor de la resistencia a la tracción se calcula mediante la siguiente expresión [23,24]:

$$\sigma_f \frac{2P}{\pi t D} \tag{4}$$

Donde P es el valor de la carga aplicada. Las propiedades del material son $E_0 = 21 \times 10^9$ Pa, $\upsilon = 0{,}2$, $y = 7{,}8 \times 10^3$ N/m^3, $\sigma_f = 10$ KPa y $G = 1 \times 10^2$ J/m^2, lo que proporciona una carga máxima de fallo de $P = 314{,}16$ N.

Para realizar los análisis se han usado 3 mallas de 9.338, 31.455 y 61.623 elementos tetraédricos lineales, como se muestra en la figura 10. El ensayo se realiza imponiendo una velocidad constante vertical en la parte superior de la probeta.

La figura 11 muestra la grieta y los elementos discretos generados. Se puede observar que el patrón de fisuración es similar para las 3 mallas y de acuerdo con el resultado esperado. La figura 12 muestra la curva de carga-desplazamiento. Los valores obtenidos para la resistencia a la tracción máxima para las mallas gruesa, media y fina son respectivamente: 10.693 KPa, 10.351 KPa y 10.235 KPa, correspondientes a un rango de entre 6% y 2% de error frente al valor esperado de $\sigma_f = 10$ KPa.

Es remarcable la insensibilidad de la curva carga-desplazamiento al tipo de malla de elementos finitos utilizada. Esta «objetividad» de los resultados numéricos frente al tamaño de la malla del FEM es una de las características esenciales de la técnica FEM-DEM.

6.4. *Ensayo de cortante*

El ensayo de cortante se diseña para aplicar un esfuerzo de cizalladura sobre una probeta, de modo que experimente una falla por deslizamiento a lo largo de un plano paralelo a las

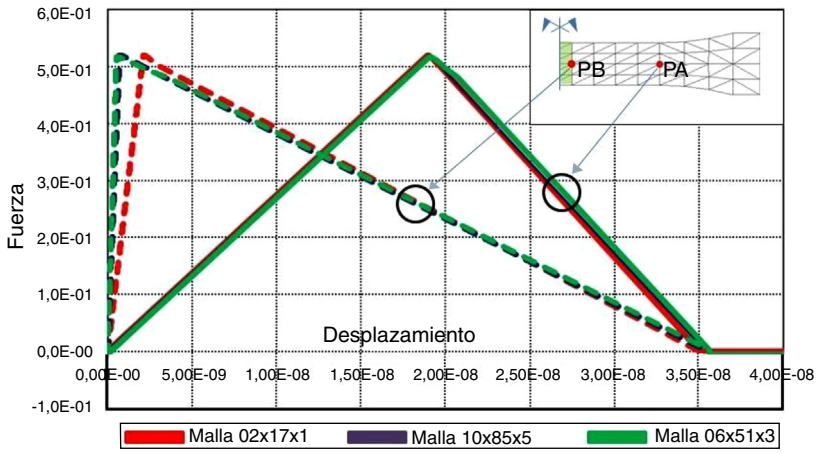

Figura 5. Ensayo normalizado 3D de tracción. Curva carga-desplazamiento de los puntos PA y PB de la muestra.

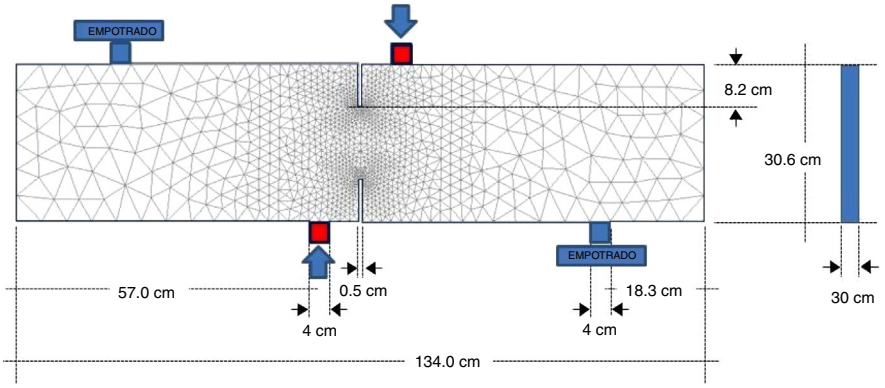

Figura 6. Viga bientallada a flexión. Geometría y condiciones de contorno.

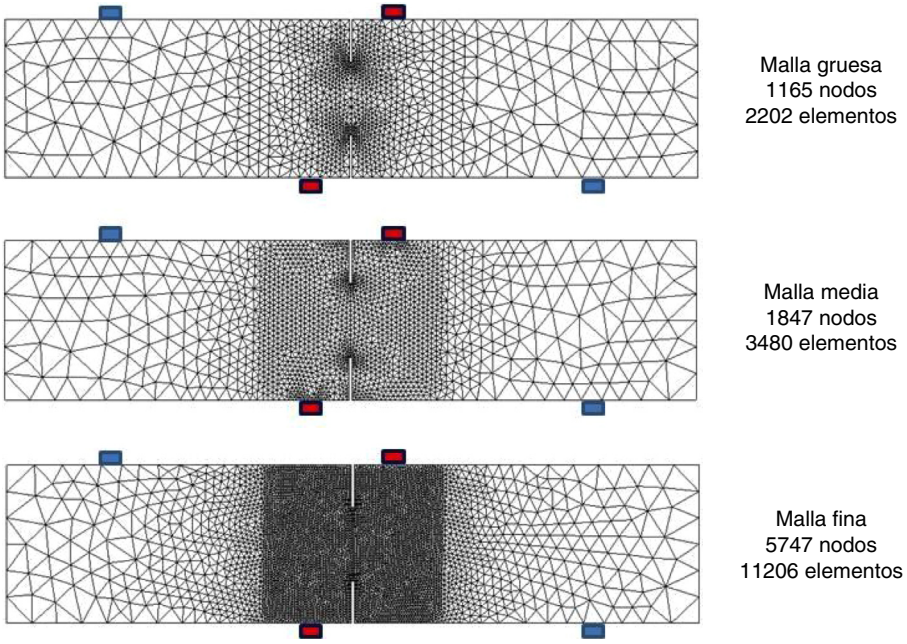

Figura 7. Viga bientallada a flexión. Mallas utilizadas.

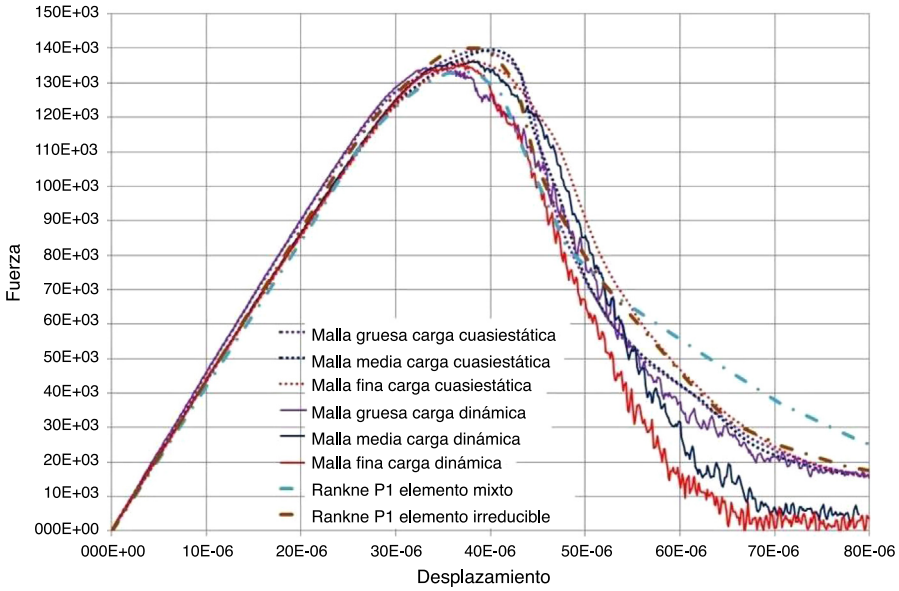

Figura 8. Viga bientallada a flexión. Relación entre la fuerza y el desplazamiento en cualquiera de los puntos referenciados en la figura 6. Los resultados obtenidos son comparados con aquellos dados en Cervera et al. [14].

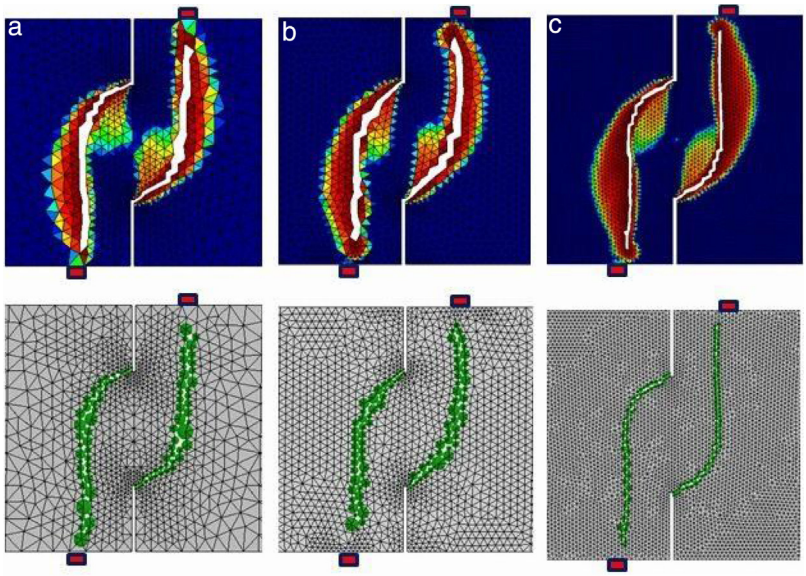

Figura 9. Viga bientallada a flexión. Superficies de igual desplazamiento y apertura de las grietas. a) Malla gruesa; b) malla intermedia; c) malla fina.

fuerzas aplicadas. Por lo general las fuerzas de cizallamiento provocan que una de las superficies de fallo de un material se mueva en una dirección y la otra superficie en dirección opuesta, de manera que el material se encuentra sometido a un estado de corte. Este ejemplo se realizó en 80 minutos usando un procesador a 2,5 MHz.

El ensayo que aquí se considera tiene como objetivo determinar la resistencia a cortante del hormigón y ha sido propuesto por Luong [21]. La probeta tiene forma tubular y su eje coincide con el eje $z=0$. Tiene varias entallas y se somete a una carga central en una de sus caras y otra excéntrica en la cara opuesta, de manera que se generen tensiones cortantes paralelas al eje $z=0$, como se describe en la figura 13, en la que también se muestran las condiciones de contorno impuestas. La profundidad de la entalla es de 10 mm y su ancho es de 4 mm. La carga se aplica imponiendo a la placa superior una velocidad constante de 1 mm/s hasta llegar a la fractura.

La definición geométrica y la malla de elementos finitos utilizada se muestran en la figura 14. El plano de cizallamiento ha sido discretizado con 4 elementos finitos tetraédricos de 4 nodos, con el fin de captar adecuadamente el gradiente de tensiones en esta zona.

Las propiedades del hormigón son $E_0 = 35 \times 10^9$ Pa, $v = 0{,}22$, $y = 7{,}8 \times 10^3$ N/m^3, $\sigma_c = 30$ MPa, $\sigma_f = 3$ MPa y $G = 75 \times 10^{-3}$ J/m^2. En general el esfuerzo máximo de corte

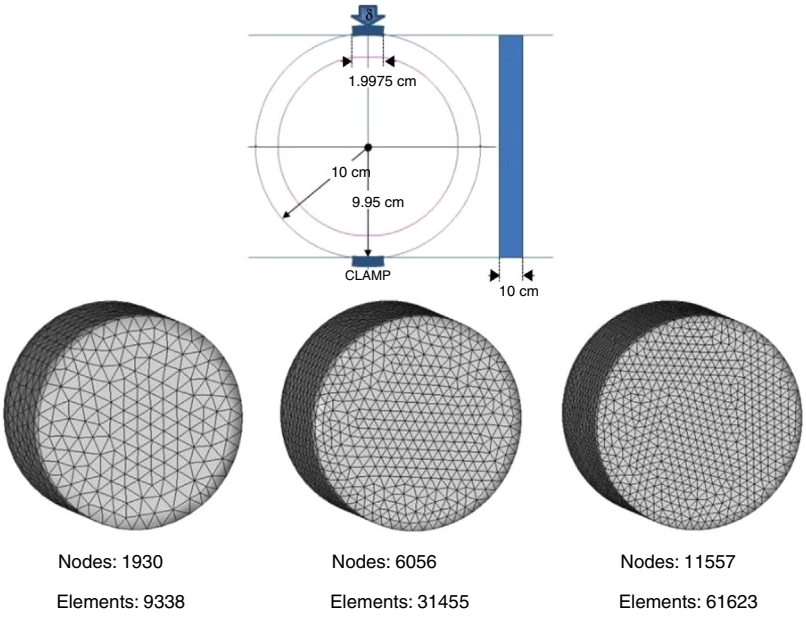

Figura 10. Ensayo de tracción indirecta. Dimensiones de la muestra, condiciones de contorno y mallas usadas de elementos finitos tetraédricos de 4 nodos.

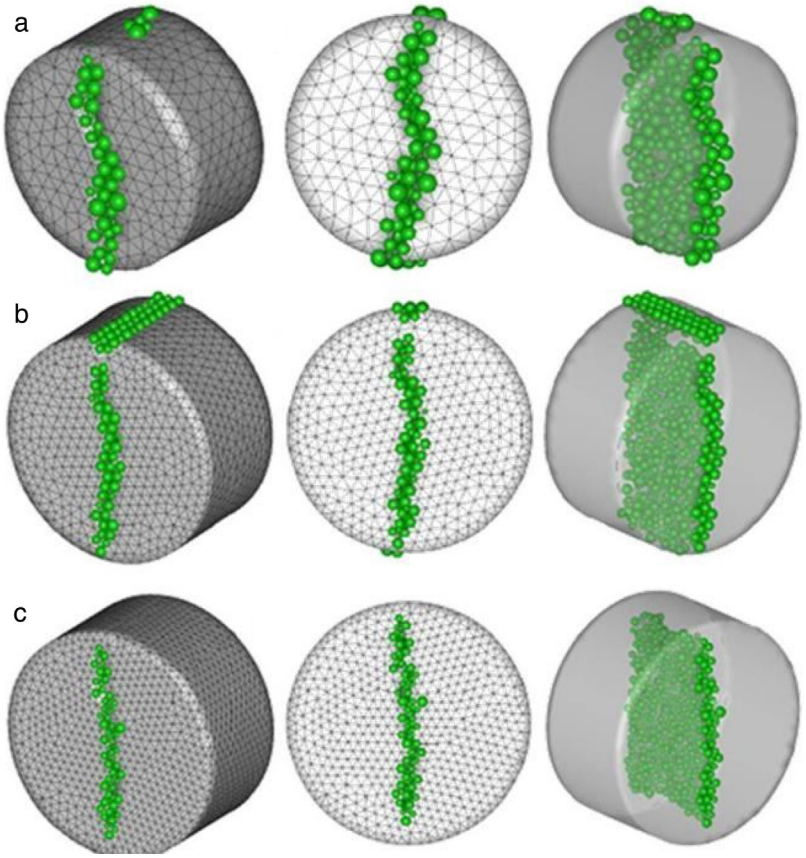

Figura 11. Ensayo de tracción indirecta. Grieta y elementos discretos generados. a) Malla gruesa; b) malla intermedia; c) malla fina.

en el hormigón es aproximadamente 1/5 o 1/6 del esfuerzo a compresión [21].

La figura 15 muestra la grieta obtenida por el experimento numérico con la técnica FEM-DEM, y se compara con los resultados de los ensayos realizados en el laboratorio. La figura 16 muestra la relación fuerza-desplazamiento obtenida numéricamente y en la que se muestra claramente la rama elástica hasta que los elementos comienzan a dañar. Considerando el tamaño de la probeta, de esta gráfica se desprende que el esfuerzo cortante último alcanza un valor de

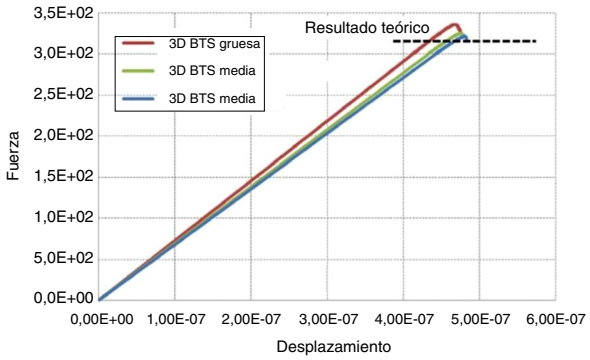

Figura 12. Ensayo de tracción indirecta. Relación fuerza-desplazamiento para las 3 mallas utilizadas.

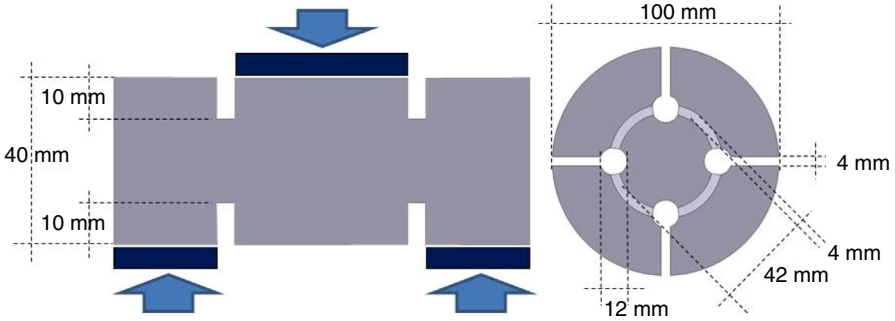

Figura 13. Ensayo de cortante. Geometría, cargas y condiciones de contorno.

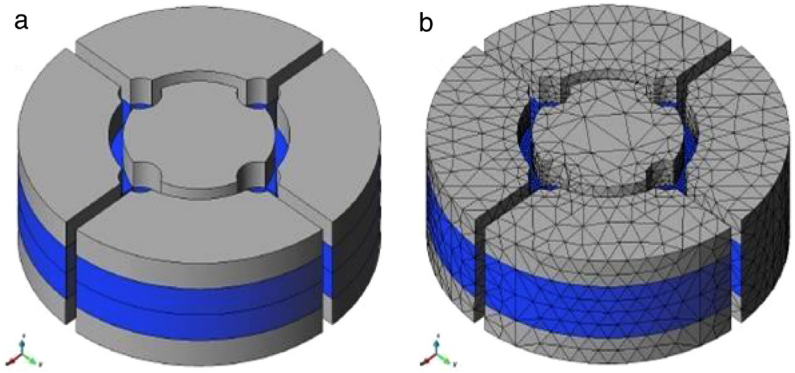

Figura 14. Ensayo de cortante. a) Definición geométrica de la probeta b) Malla de elementos finitos.

5,10 MPa. Este resultado es coherente y próximo al valor esperado [21].

6.5. *Ensayo de compresión simple*

Uno de los ensayos más frecuentes realizados en probetas de hormigón es el de compresión simple [25]. El ensayo se realiza de acuerdo con la instrucción de hormigón estructural (EHE-08) [26], la cual hace referencia a la norma UNE-EN 12390-3.2009 [27], en donde se especifica las dimensiones de las probetas y las condiciones de ensayo.

El experimento numérico que se presenta se realiza en 2D, utilizando probetas hexaédricas en tensión plana y para el caso 3D probetas cilíndricas normalizadas.

El ensayo 2D consiste en comprimir la probeta cuyas dimensiones y condiciones de carga se muestran en la figura 17, y en la cual también se presentan las mallas utilizadas. El objetivo del ensayo no solo se trata de encontrar la tensión máxima a compresión que es capaz de resistir la probeta, sino también la forma de las fisuras en función de las distintas condiciones de contorno que se pueden dar en el ensayo.

Las propiedades del hormigón utilizadas son: $E_0 = 30{,}0 \times 10^9$ Pa, $\upsilon = 0{,}20$, $\gamma = 24 \times 10^3$ N/m^3, $\sigma_c = 2.000$ MPa, $\sigma_t = 20{,}0$ MPa y $G = 105 \times 10^{-3}$ J/m^2. En este caso la tensión máxima de compresión, independientemente de las condiciones de apoyo, es de 20×10^6 Pa. En la figura 18 se muestra que los resultados obtenidos con ambas probetas se acercan mucho al resultado esperado.

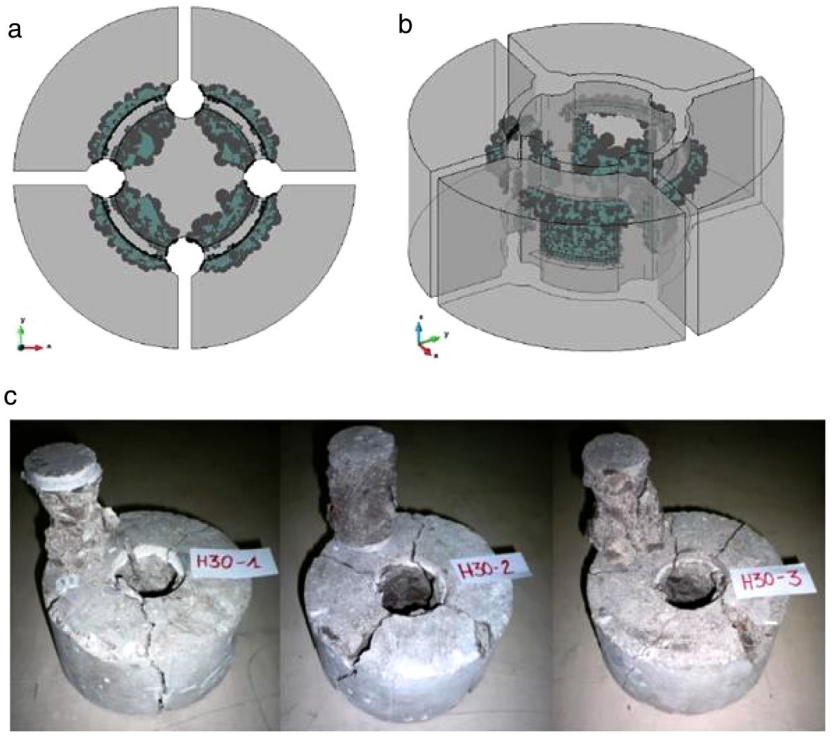

Figura 15. Ensayo de cortante. a) Vista superior; b) perspectiva de la grieta obtenida por la técnica FEM-DEM; c) rotura en probetas de laboratorio.

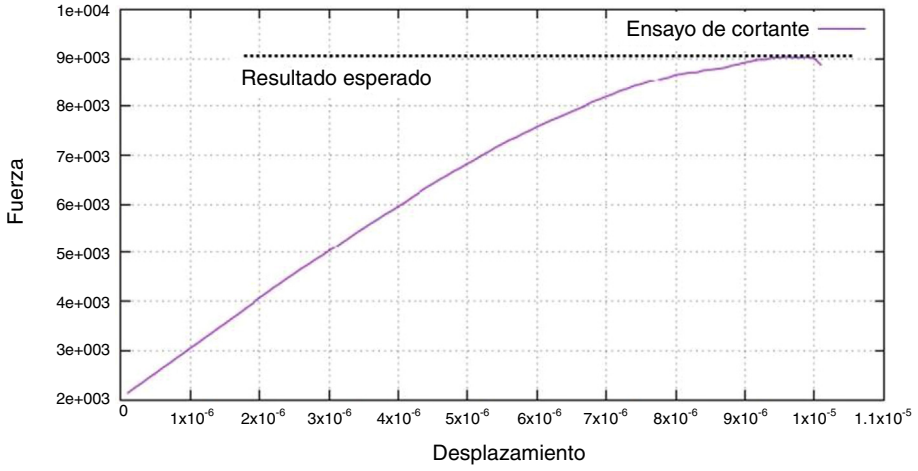

Figura 16. Ensayo de cortante. Relación fuerza-desplazamiento obtenida por el ensayo numérico.

Los resultados más interesantes en este caso se muestran en las figuras 19-21. En todas ellas la figura *a)* corresponde al patrón de grietas generado, la *b)* son las superficies de igual desplazamiento y la figura *c)* el daño elemental. Estos resultados se pueden comparar con la figura *d)* que corresponde a los resultados teóricos [28], o con la figura e), que corresponde a los resultados obtenidos con LS-DYNA [29] para el caso biempotrado (figs. 19 y 20) o con un ensayo real (fig. 21).

La figura 19 corresponde al caso en que las superficies de carga tienen un desplazamiento horizontal nulo utilizando la malla de elementos finitos estructurada. Los resultados muestran claramente 2 grietas a 45° claramente definidas, y corroboradas por el patrón de daño mostrado. El resultado numérico mostrado en la figura *e)* muestra el mismo patrón. Sin embargo, observando los resultados teóricos [28] el daño se genera sobre 2 bandas a 45° formadas por grietas verticales.

La figura 20 muestra el mismo caso, con el desplazamiento horizontal de las superficies de carga impedidas, pero utilizando la malla no estructurada. Como se puede observar en la fig. 20 *a)* el patrón de grietas se asemeja más a los resultados teóricos esperados, con grietas verticales localizadas en 2 bandas a 45°. Es importante mencionar que ningún código numérico al que los autores han tenido acceso es capaz de presentar este tipo de resultados, pues todos muestran correctamente la banda de daño (figuras e), pero no así las fisuras verticales sobre dicha banda. El por qué la malla no estructurada presenta un resultado más

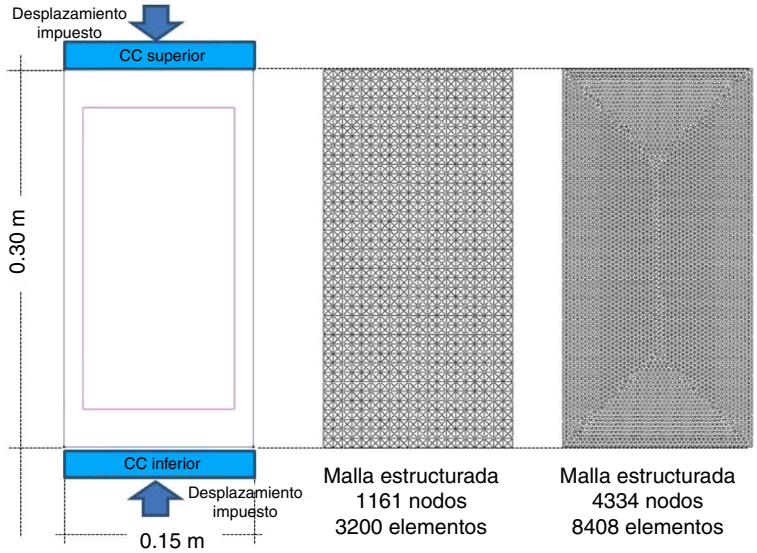

Figura 17. Ensayo de compresión simple. Probeta y mallas utilizadas en el ensayo 2D.

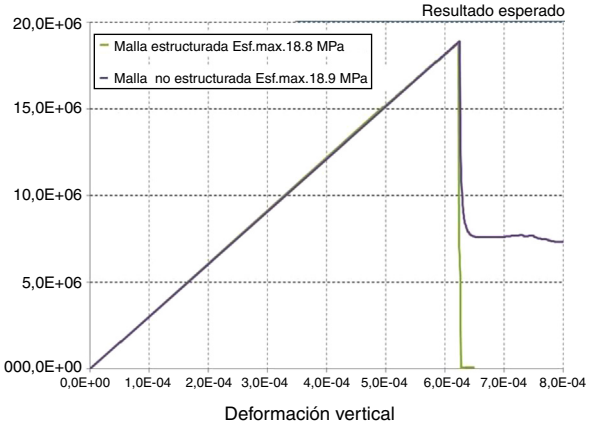

Figura 18. Ensayo de compresión simple. Relación tensión-deformación para el análisis 2D.

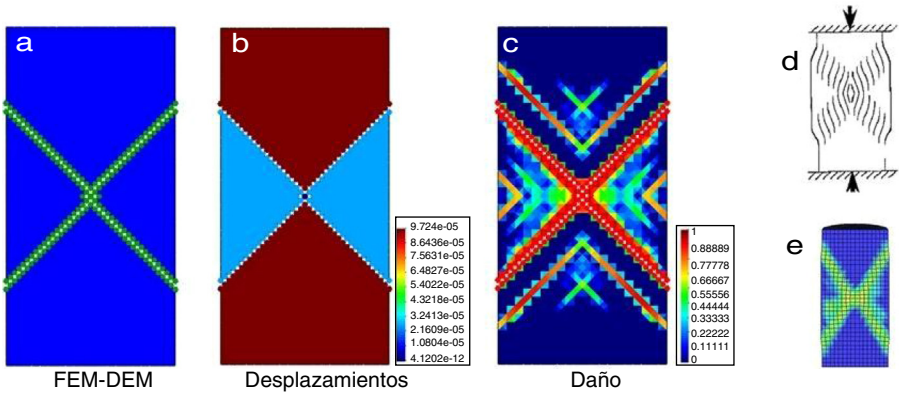

Figura 19. Ensayo de compresión simple. Probeta biempotrada, malla estructurada.

próximo al teórico está relacionado con la no uniformidad en la discretización de dominio. Las pequeñas variaciones numéricas inducidas por los elementos de distinto tamaño son suficientes para alterar la estabilidad de los resultados que se obtienen con una malla estructurada, encontrado así un resultado diferente.

La figura 21 presenta los resultados obtenidos con la malla no estructurada en el caso en que las superficies de carga tengan libertad de movimiento horizontal. Teóricamente [28], como se muestra en la figura 21 d, la fisura debe ser vertical, sin embargo, como se observa en la figura 21 e los ensayos de laboratorio

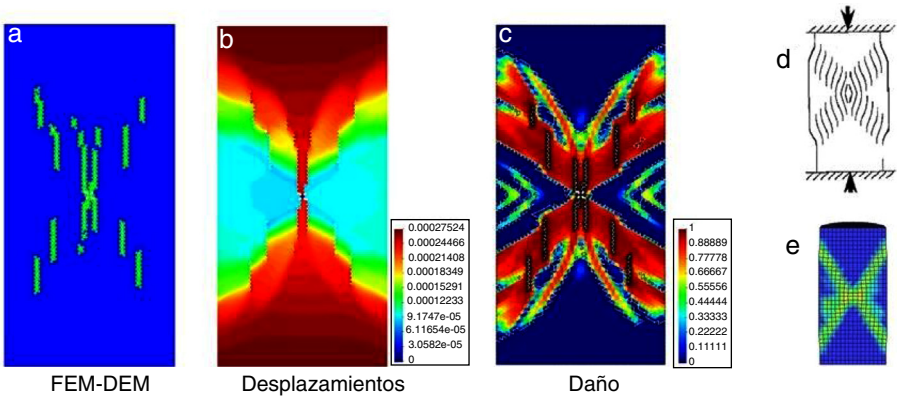

Figura 20. Ensayo de compresión simple. Probeta biempotrada, malla no estructurada.

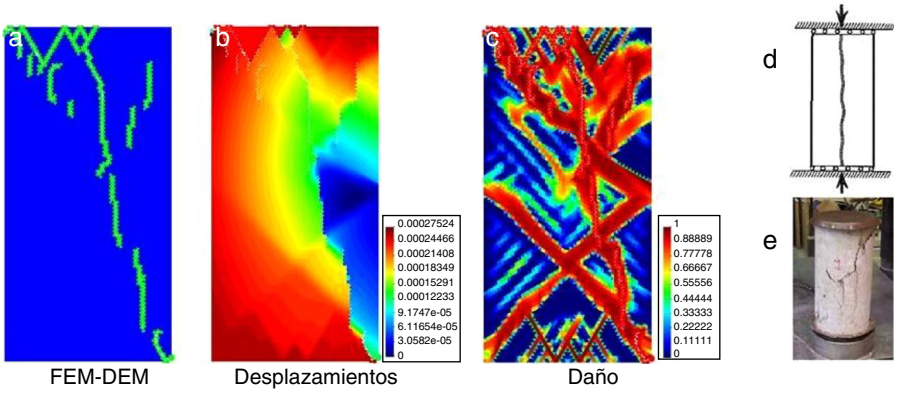

Figura 21. Ensayo de compresión simple. Probeta simplemente apoyada, malla no estructurada.

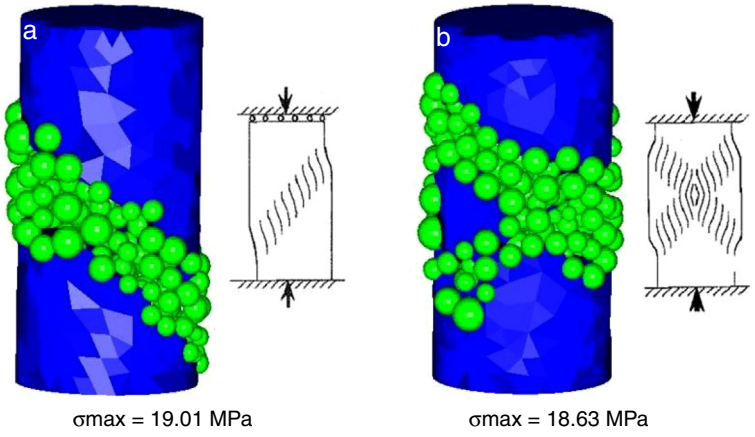

Figura 22. Ensayo de compresión simple. Probeta 3D para distintos casos de apoyo. a) Bases empotrada-libre; b) bases biempotradas.

tienden a presentar varias fisuras verticales [27]. Los resultados mostrados en la figura 21 a concuerdan con los resultados esperados.

El mismo ejemplo ha sido resuelto en 3D utilizando una probeta circular (fig. 17) y las mismas propiedades mecánicas. La malla está formada por 926 nodos y 4.030 tetraedros. Los resultados obtenidos se muestran en la figura 22 a para el caso en que una de las superficies de carga se encuentre impedida en su desplazamiento horizontal, mientras que la otra no. La figura 22 b muestra el caso en que ambas superficies tengan el desplazamiento horizontal impedido. En ambos ejemplos la tensión máxima se aproxima bastante a la esperada. No solo eso, a pesar que la malla sea tan gruesa, las grietas generadas coinciden con los resultados teóricos. Cabe comentar que este ejemplo no requiere más de 5 minutos de cálculo en un procesador a 2,5 GHz.

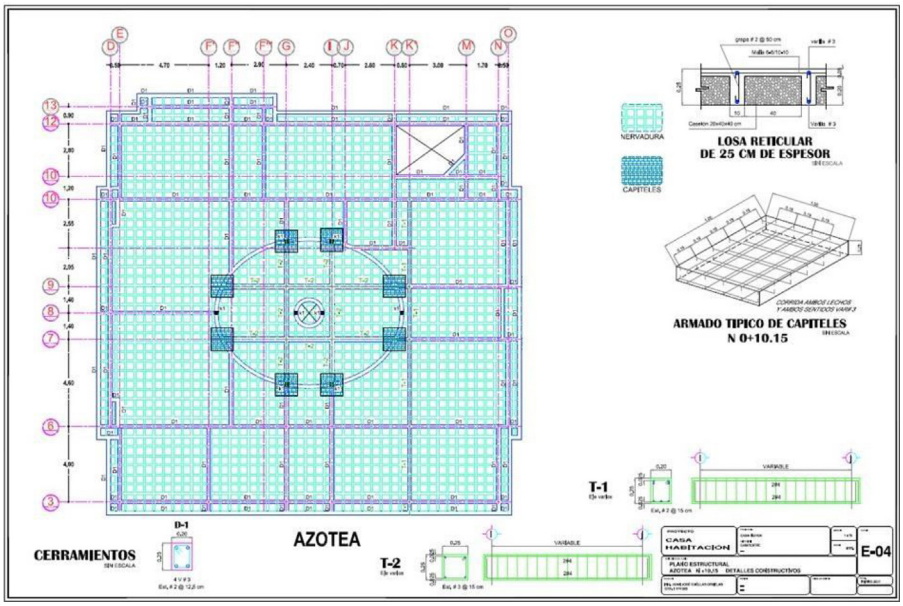

Figura 23. Losa reticular. Plano estructural.

6.6. *Losa reticular*

El uso de forjados reticulares como elementos estructurales está ampliamente consensuado y permite construir geometrías arquitectónicas más libres. El forjado analizado corresponde al techo de una vivienda. La planta es un cuadrado de 22 m de lado, con una superficie plana ovalada en el centro y los lados en parteaguas con un desnivel de 2 m. En la figura 23 se muestra la planta estructural en donde se puede observar claramente la armadura de acero. Básicamente se trata de un forjado reticular de 0,25 m de espesor con una capa de compresión de 0,05 m y casetones de $0{,}40 \times 0{,}40 \times 0{,}20$ m. A lo largo de las nervaduras se colocan varillas de acero del n.° 3 ($\phi = 0{,}0095$ m).

Adicionalmente existe una serie de cerramientos (D1) y vigas (T1 y T2), así como 4 capiteles de columna. Los cerramientos tienen una sección de $0{,}25 \times 0{,}20$ m armados con 4 varillas de acero del n.° 3. Las vigas T1 y T2 tienen un espesor de 0,25 m y un ancho de 0,20 m para la viga T1 y de 0,25 m para la viga T2. Ambas están armadas con 4 varillas de acero del n.° 4 ($\phi = 0{,}0127$ m). Finalmente, el armado de los capiteles se realiza con varillas del n.° 3 @ 0,15 m en ambos lechos y en ambas direcciones. La figura 24 a) muestra el armado de toda la losa, así como un detalle del armado de los capiteles en la figura 24 b).

Las propiedades del hormigón son. $E_0 = 21 \times 10^9$ Pa, $v = 0{,}20$, $y = 24 \times 10^3$ N/m^3, $\sigma_c = 20$ MPa, $\sigma_f = 2$ MPa y $G = 100 \times 10^{-3}$ J/m^2.

La placa se encuentra apoyada sobre los muros mostrados en la figura 25. A efectos del análisis dichos muros se consideran lo suficientemente rígidos y empotrados en su base.

Las cargas consideradas son el peso propio de la estructura, las cargas muertas 1.620 N/m^2 y las cargas vivas 400 N/m^2. Dichos valores consideran el peso del plafón, las instalaciones y acabados finales, sin considerar cargas de nieve o viento. Adicionalmente se impone un asentamiento diferencial de 0,0035 m de los puntos de la base del muro, como se indica en la figura 25.

El problema se ha resuelto utilizando una malla de 1.369,192 tetraedros y 368.969 nodos. Por otra parte, se han definido 5.084 elementos lineales para representar las varillas de acero. La figura 26 a representa el conjunto del forjado y muros a analizar, mientras que la figura 26 b corresponde a un detalle cercano al lucernario, donde se aprecian las nervaduras de la placa, así como algunas de las vigas T2.

La figura 27 a muestra los resultados del desplazamiento de la estructura después de que el asentamiento diferencial de la base sea de 0,0035 m. En la figura 27 b se aprecia un corte muy definido en la cubierta superior. Se observa que el desgarro en la cubierta es perpendicular a la dirección del muro, poniendo de manifiesto la gran rigidez que tiene la cubierta superior.

En la figura 28 a se puede apreciar la deformidad de la estructura vista desde abajo. Es interesante observar que el lucernario sufre los desplazamientos máximos, incluso mayores a los que sufre el muro sujeto al asentamiento diferencial. La figura 28 b muestra una vista inferior de la losa donde se aprecia el daño producido en la unión del muro con esta.

En la figura 29 se observan los esfuerzos axiales sobre los elementos de acero pertenecientes a la viga T2 en la zona cercana al lucernario. En esta figura se puede observar los elementos en tracción y compresión debido a gran flexión a la que está sujeta esta parte de la estructura.

La figura 30 muestra las zonas dañadas de la estructura utilizando una visualización de la estructura deformada con un factor de escala de 5.000. El recuadro *a)* muestra una vista inferior de la losa en donde se puede observar la separación entre el muro y la losa, mientras que el recuadro *b)* muestra una vista superior mostrando el desgarro de la cubierta. En vista de los resultados obtenidos es claramente notoria la gran rigidez que posee la losa.

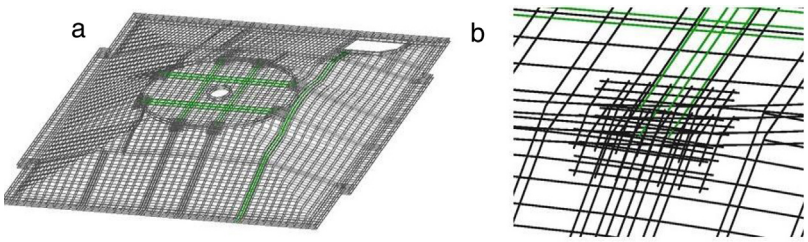

Figura 24. Losa reticular. a) Parrilla del armado de la losa; b) detalle del armado en los capiteles.

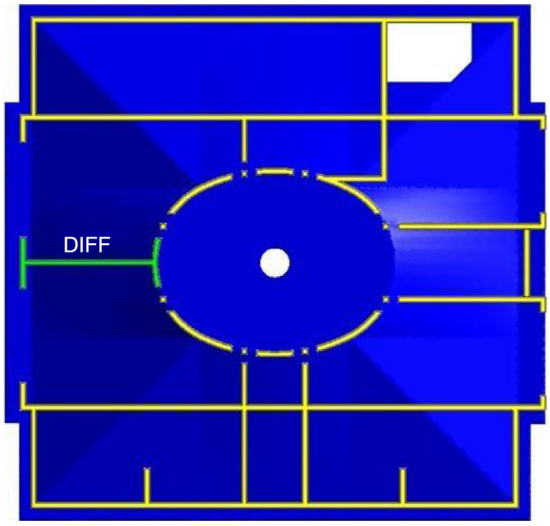

Figura 25. Losa reticular. Localización de los muros de carga. El muro con un asentamiento diferencial se encuentra marcado como DIFF.

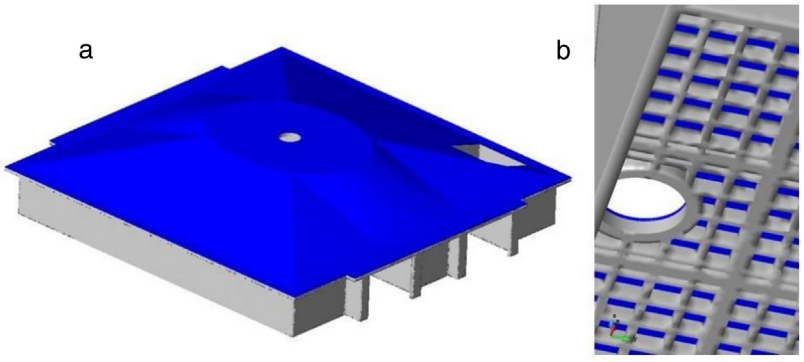

Figura 26. Losa reticular. a) Vista del conjunto; b) detalle de las nervaduras cercanas al lucernario.

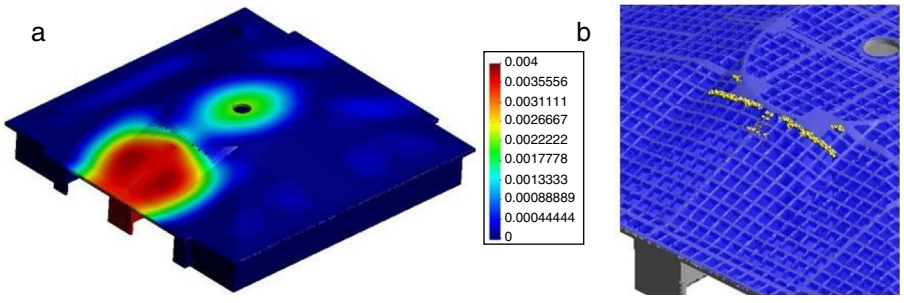

Figura 27. Losa reticular. a) Vista superior de la estructura con iso-superficies de igual desplazamiento; b) vista superior de las grietas generadas.

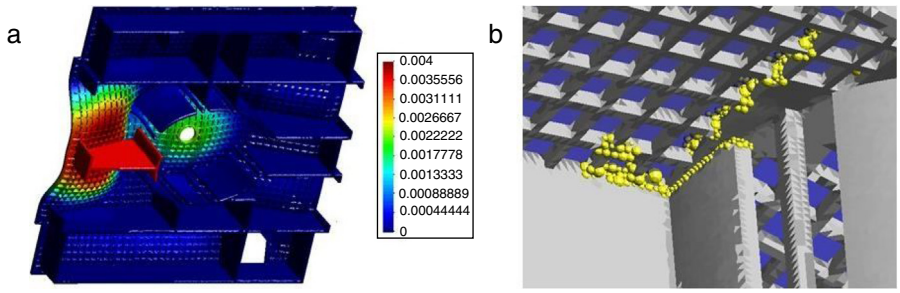

Figura 28. Losa reticular. a) Vista inferior de la estructura deformada; b) vista inferior de las grietas generadas.

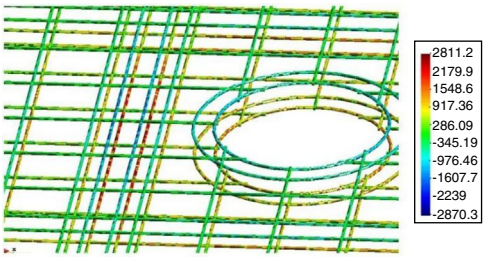

Figura 29. Losa reticular. Elementos del refuerzo de acero en la zona cercana al lucernario.

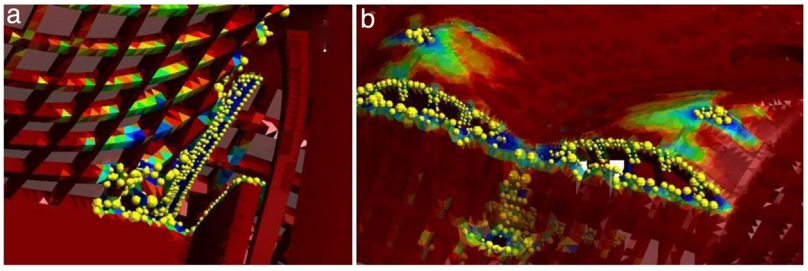

Figura 30. Losa reticular. Daño en la estructura. a) Vista inferior; b) vista superior.

Figura 31. Iglesia cisterciense del monasterio de Poblet. a) Vista interior de la nave central; b) planta y sección analizada.

6.7. Iglesia cisterciense del monasterio de Poblet

La iglesia, perteneciente al Real Monasterio de Santa María de Poblet, ubicado en Vimbod (Tarragona), es un monumento histórico artístico declarado por la UNESCO como patrimonio de la humanidad. Construido a partir de la segunda mitad del siglo XII, el templo adopta una planta basilical, orientado su ábside al Este. La integran 3 naves de 7 tramos, con crucero, ábside central, girola y capillas absidiales. La nave central tiene unas dimensiones de 85 m de longitud, 21 m de anchura y 28 m de altura, mientras que las laterales alcanzan los 18 m de altura. La diferencia de altura respecto a la nave central no se resuelve

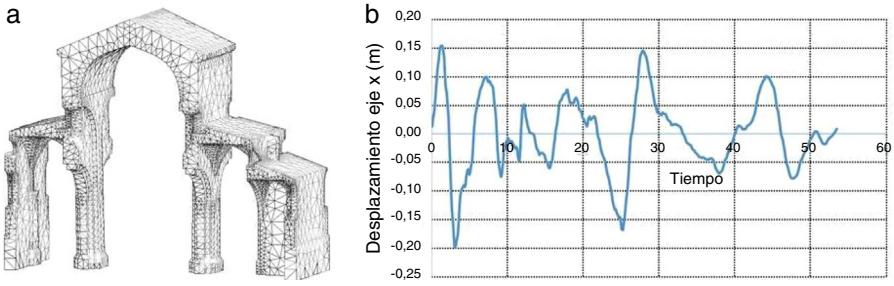

Figura 32. Iglesia cisterciense del monasterio de Poblet. a) Malla de elementos finitos de una sección perteneciente a la nave principal; b) excitación temporal en desplazamientos.

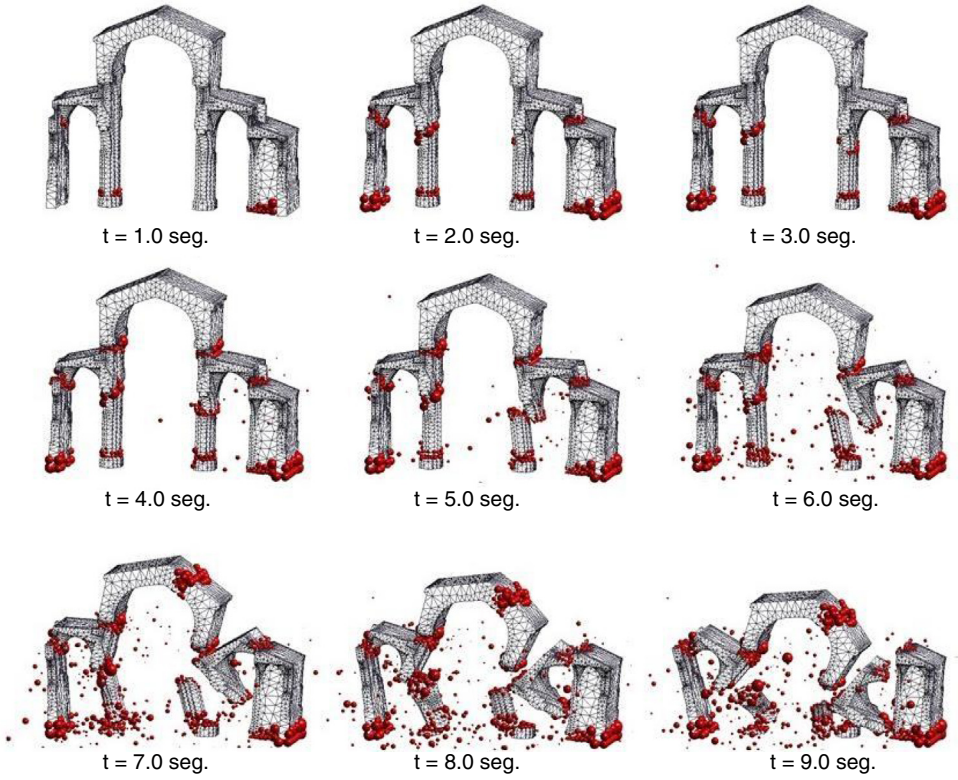

Figura 33. Iglesia cisterciense del monasterio de Poblet sometida a un terremoto. Evolución de las fracturas en la nave central en distintos tiempos.

mediante arbotantes del estilo gótico, sino con contrafuertes. La nave central plenamente románica está cubierta con bóveda de cañón apuntada, con arcos fajones en cada tramo, como se muestra en la figura 31.

Para simplificar el estudio se analiza únicamente una sección de la nave central que se considera simétrica respecto al eje normal a la dirección de dicha nave. La malla que discretiza la iglesia tiene 9.294 nodos y 32.487 elementos tetraédricos de 4 nodos, como se muestra en la figura 32 a. Las propiedades del material utilizado se corresponden con una piedra caliza propia de la región, con $E_0 = 35 \times 10^9$ Pa, $\upsilon = 0{,}22$, $\gamma = 25 \times 103$ N/m^3, $\sigma_c = 780$ MPa, $\sigma_f = 5$ MPa y G = 100×10^{-3} J/m^2. En cuanto a las condiciones de apoyo se considera empotrada toda la superficie inferior del modelo.

Las cargas aplicadas corresponden a un movimiento oscilatorio impuesto en dirección normal al eje de la nave central, como se muestra en la figura 32 b. Los valores mostrados corresponden al movimiento oscilatorio en dirección S 00E de los registros en desplazamientos obtenidos del acelerograma del sismo «El Centro» del 18 de mayo de 1940 [30]. Estos valores se aplican al modelo con una reducción del 50%, de forma que simule un sismo de magnitud 6,0 M_W.

Aunque el registro de movimientos dura más de 50 segundos la estructura solo es capaz de soportar en pie 4 segundos, colapsando de forma total a partir de ese instante. En la figura 33 se observa a intervalos de un segundo las grietas formadas en la iglesia. Inicialmente ocurre un cizallamiento de las columnas y de la pared más rígida, para posteriormente cortar las bases de los arcos. A partir del segundo 5 se observa cómo la estructura colapsa en su totalidad reduciéndose a escombros.

Este ejemplo muestra claramente la capacidad de la técnica FEM-DEM para simular la aparición y propagación de múltiples fracturas en estructuras de mampostería, así como el eventual colapso de la estructura bajo cargas dinámicas.

7. Conclusiones

Se ha descrito en el presente artículo las líneas generales de la metodología FEM-DEM propuesta por los autores en Zárate y Oñate [9] y Zárate et al. [10] para la predicción de la aparición y evolución de fisuras en estructuras de hormigón. Los ejemplos que se han presentado muestran las posibilidades de la técnica FEM-DEM para el cálculo no lineal de estructuras de hormigón en masa y armado, así como en estructuras de mampostería. La técnica FEM-DEM es también aplicable al estudio de la fractura en macizos rocosos [31,32].

Agradecimientos

Los autores agradecen la colaboración del Ing. Juan José Cuellar Ornelas, al facilitar de forma desinteresada la información usada en el análisis del forjado. Los resultados aquí presentados han sido obtenidos utilizando los programas FEM2DEM y DEMPACK (http.//www.cimne.com/dempack) en los que se ha implementado la metodología FEM-DEM descrita.

Bibliografía

[1] P.A. Cundall, O.D.L. Strack, A discrete numerical model for granular assemblies, Geotechnique 29 (1979) 47–65.
[2] Labra C. Advances in the development of the discrete element method for excavation processes, Ph.D. Thesis. Barcelona; 2012.
[3] J. Rojek, E. Oñate, F. Zarate, J. Miquel. Modelling of rock, soil and granular materials using spherical elements. Cracow: 2nd European Conference on Computational Mechanics ECCM-2001; 26-29 June 2001.
[4] J.R. Williams, O'Connor, discrete element simulation and contact problem, Archives of Computer Methods in Engineering 6 (1999) 279–304.
[5] E. Oñate, F. Zárate, J. Miquel, M. Santasusana, M.A. Celigueta, F. Arrufat, et al., A local constitutive model for the discrete element method, Application to Geomaterials and Concrete, Computational Particle Mechanics 2 (2015) 139–160.
[6] S. Katagiri, S. Takada. Development of fem-dem combined method for fracture analysis of a continuos media. Memoirs of the Graduate School of Science and Technology. Kobe University Japan; 20A (2002-03), 65-79.
[7] A. Munjiza. The combined finite-discrete element method. John Wiley & Sons Ltd, England; 2004.
[8] S. Shmauder, J. Wulf, H.F. Fischmeister, Finite element modelling of crack propagation in ductile fracture, Computation Materials Science 1 (1993) 297–301.
[9] F. Zárate, E. Oñate, A simple FEM-DEM technique for fracture prediction in materials and structures, Computational Particle Mechanics 2 (2015) 301–314.
[10] F. Zárate, A. Cornejo, E. Oñate, A three-dimensional FEM-DEM technique for predicting the evolution of fracture in geomaterials and concrete, Computational Particle Mechanics (2017), 10.1007/s40571-017–z.0178.
[11] E. Oñate. Cálculo de estructuras por el método de elementos finitos. Análisis estático lineal. Vol. 1. Sólidos (CIMNE, Barcelona, 2017, en castellano). Vol 2. Placas y láminas (Springer, Barcelona, 2009, en inglés).
[12] M. Cervera, M. Chiumenti, C. Agelet de Saracibar, Shear band localization via local j2 continuum damage mechanics, Computer Methods in Applied Mechanics and Engineering 193 (2004) 849–880.
[13] M. Cervera, M. Chiumenti, R. Codina, Mixed stabilized finite element methods in nonlinear solid mechanic's part I. Formulation, Computer Methods in Applied Mechanics and Engineering 199 (2010) 2559–2570.
[14] M. Cervera, M. Chiumenti, R. Codina, Mesh objective modelling of cracks using continuous linear strain and displacements interpolations, International Journal for Numerical Methods in Engineering 87 (2011) 962–987.
[15] P.R. Johnson, N. Petrinic, E. Sli. Element –splitting for simulation of fracture in 3D solid continua. Barcelona: VIII International Conference on Computational Plasticity; 2005.
[16] L. Mishnaevsky Jr., N. Lippmann, S. Schmauder, Computational modelling of crack propagation in real microstructures of steels and virtual testing of artificially designed materials, International Journal of Fracture 120 (2003) 581–600.
[17] J. Lopez, S. Oller, E. Oñate, J. Lubliner, A homogeneous constitutive model for masonry, International Journal for Numerical Methods in Engineering 46 (1999) 16511671.
[18] O.C. Zienkiewicz, J.Z. Zhu, The superconvergent patch recovery (spr) and adaptive finite element refinement, Computer Methods in Applied Mechanics and Engineering 101 (1992) 207–224.
[19] E. Oñate. Desarrollos y aplicaciones de modelos de fractura en la Escuela de Ingenieros de Caminos de Barcelona. Centro Internacional de Métodos Numéricos en Ingeniería, CIMNE; 2000.
[20] C. Labra, E. Oñate, High-density sphere packing for discrete element method simulations, Communications in Numerical Methods in Engineering 25 (2009) 837–849.
[21] M. Luong, Tensile and shear strengths of concrete and rock, Engineering Fracture Mechanics 1–3 (1990) 127–135.
[22] Astm standard d638-10, 2003. Standard test method for tensile properties of plastics. Astm international, west Conshohocken, PA, 2003. doi. 10.1520/d0638-10, www.astm.org.
[23] F. L. L. B. Carneiro. A new method to determine the tensile strength of concrete. Proceedings of the 5th meeting of the brazilian association for technical rules; 1943. p. 126-129 (Portuguese).
[24] C.G. Rocco, G.V. Guinea Tortuero, J. Planas Roselló, M. Elices Calafat, Efecto del tamaño de probeta sobre la resistencia a la tracción medida con el ensayo brasileño, Hormigón y Acero 204 (1997) 47–63.
[25] J. Rodríguez del Viso, J.R. Carmona, G. Ruiz López, Efecto de la forma y el tamaño de la probeta en la resistencia a compresión en hormigón de alta resistencia, Hormigón y Acero 248 (2008) 77–86.
[26] Norma a instrucción de hormigón estructural (EHE-08) [consultado 2017]. Disponible en: https//www.fomento.gob.es/MFOM/LANG_CASTELLANO/ORGANOS_COLEGIADOS/MASORGANOS/CPH/instrucciones/EHE_es/.
[27] UNE-EN 12390-3.2009 Ensayos de hormigón endurecido. Parte 3. Determinación de la resistencia a compresión de probetas (2009). Asociación Española de Normalización y Certificación AENOR.
[28] Z.P. Bazant, J. Planas, Fracture and size effect in concrete and other quasi-brittle materials, CRC Press LLC, 1998.
[29] Y.D. Murray, A. Abu-Odeh, R. Bligh. Evaluation of LS-DYNA Concrete Material Model 159 Publication No. FHWA-HRT-05-063 (2007) US Department of Transportation.
[30] Ground accelerogram from el centro, imperial valley irrigation district (comp s00e) [consultado 2017]. Disponible en: http//www.eng.ucy.ac.cy/petros/earthquakes/eq1.txt.
[31] J.M. González, F. Zárate, E. Oñate, Pulse fracture simulation in shale rock reservoirs: DEM and FEM–DEM approaches, Computational Particle Mechanics 5 (2017) 355–373.
[32] E. Oñate, F. Zárate, M.A. Celigueta, J.M. González, J. Miquel, J.M. Carbonell, et al., Advances in the DEM and coupled DEM and FEM techniques in non linear solid mechanics advances in computational plasticity, Springer, 2018, pp. 309–335.

Presentación del

Número especial de la revista "Hormigón y Acero" dedicado a Carmen Andrade

Sala Verde — Escuela Técnica Superior de Ingenieros de Caminos, Canales y Puertos — UPM
C/ Profesor Aranguren s/n — 28040 Madrid

Jueves, 14 de marzo de 2019

16:30 Apertura y presentación del acto

Presidido por el Director de la ETSI Caminos, C. y P., Francisco Javier Martín Carrasco

Miembros de la mesa e intervinientes:

Gonzalo Ruiz, Director de Hormigón y Acero
Rosa Menéndez, Presidenta del CSIC
Antonio M. Cutillas, Presidente de ACHE
Hugo Corres, Expresidente de fib
Carmen Andrade, Profesora de Investigación del CSIC (jubilada) — CIMNE

17:20 Presentaciones de autores de artículos en el número especial

Moderador: Javier Sánchez Montero, CSIC, Editor Asociado para el número especial

Intervienen:

Eugenio Oñate, Univ. Politécnica de Cataluña — CIMNE
Predicción de fracturas en estructuras de hormigón combinando los métodos de elementos finitos y de elementos discretos

Giuseppe Mancini, Politécnico de Turín
Desde experimentos hasta diseño: una definición probabilística de formulaciones de diseño a partir de modelos de resistencia empíricos y semiempíricos

Pedro Garcés, Universidad de Alicante
Aplicación de tratamientos electroquímicos combinados al hormigón armado: extracción electroquímica de cloruros más protección catódica

Gonzalo Ruiz, Universidad de Castilla-La Mancha
Ley tensión-deformación en compresión para el análisis no lineal de estructuras de hormigón reforzado con fibras de acero

Jesús Rodríguez Santiago, Univ. Politécnica de Madrid
Investigación e innovación en construcción: colaboración en los últimos 25 años

18:30 Café

19:00 Mesa redonda sobre durabilidad de estructuras de hormigón: necesidad de investigación y mantenimiento

Moderador: Jesús Rodríguez Santiago, UPM

Intervienen:

Hugo Corres, Expresidente de fib
Eugenio Nasarre, Subdirector de Infraestructura de ADIF
Luis Vega, Subdirector General de Arquitectura y Edificación, Ministerio de Fomento
Jaime López-Cuervo, Subdirector General de Conservación, DG Carreteras, Ministerio de Fomento
Carmen Andrade, Profesora de Investigación del CSIC (jubilada) — CIMNE

20:20 Clausura

20:30 Vino español

Inscripción gratuita: Secretaría de ACHE, Beatriz Gutiérrez Martínez de la Casa, beatriz@e-ache.net, 91 067 41 64
LOS ASISTENTES RECIBIRÁN UN EJEMPLAR GRATUITO DEL NÚMERO ESPECIAL

ACHE
www.e-ache.com

Available online at
ScienceDirect
www.sciencedirect.com

Hormigón y Acero 2019; 69(S1):71–74

HORMIGÓN y ACERO
www.elsevierciencia.com/hya

Research and innovation in construction: Collaboration in the last quarter century

Investigación e innovación en construcción: colaboración en los últimos 25 años

Jesús Rodríguez [1]

ETSAM-UPM, Spain

Received 27 May 2018; accepted 24 September 2018
Available online 22 November 2018

Abstract

This article summarises the developments in construction R&I since the nineteen nineties in the context of collaboration between private companies, research institutes and universities. Such cooperation has adopted the form of both continuous participation in R&I fora and partnering in specific research projects.

Keywords: Innovation in construction; Technology platforms

Resumen

Este artículo resume algunos aspectos de la I+D+i en el sector de la construcción, acontecidos desde los años noventa del siglo pasado, en relación con la colaboración entre las empresas y los organismos de investigación, a través tanto de la participación continua en foros en los que se aborda la I+D+i como de actuaciones puntuales en proyectos I+D+i en cooperación.

Palabras clave: Innovación en construcción; Plataformas tecnológicas

1. Introduction

The need to heighten competitiveness in productive industries has called for new forms of collaboration among companies, research bodies (universities and both research and technological institutes) and the end users of each industry's products. The construction industry, aware of that need, has been participating since the nineteen nineties in research, development and innovation initiatives. This article discusses some of the R&I-related initiatives undertaken in construction since the last decade of the twentieth century and the first two of the twenty-first.

2. Last decade of the twentieth century

Spain's accession to the European Union opened up new prospects for collaboration in R&I, with the country's participation in Framework Programmes in general and in Brite-Euram for construction-related proposals in particular. These projects were implemented by consortia involving six to ten European partners.

By way of example, during those 10 years Spain participated in Brite Euram projects on optimisation of aggregate crushing, the development of porous concrete pavements and the design of models to simulate the behaviour of concrete structures subject to decay induced by reinforcement corrosion, freeze–thaw processes or the alkali-aggregate reaction. Those projects, headed respectively by French, Dutch and English partners, were highly

E-mail addresses: jesus.rodriguez@upm.es, jesus.rodriguez.santiago@gmail.com
[1] Associate professor.

https://doi.org/10.1016/j.hya.2018.09.001

rewarding not only for the technical results but also for the introduction of new forms of partnering between companies and research bodies from different European countries. That collaboration prompted the establishment of relations that transcended technological developments.

Nationally, the experience acquired in Eureka R&I projects implemented with Spanish support paved the way for initiatives of interest. By way of example, collaboration among Spanish CSIC[1] (IETcc[2] and Cenim[3]) and Swedish (CBI[4]) research institutes and Geocisa (www.geocisa.com), a Spanish company, led to the development of devices for the non-destructive measurement of reinforcement corrosion in concrete structures. That project launched a whole new generation of devices presently used the world over.

In the same time frame, a group of European construction companies and material manufacturers created ENCORD (www.encord.org) to explore R&I partnering formulas from an industrial perspective. The aim was to further participation in European projects and share experiences, among others, around the difficulties involved in including project results in production streams (innovation). ENCORD later joined a broader network going by the name of Eccredi (www.eccredi.org), in which companies, professional associations, research institutes, universities and other stakeholders participated, primarily to unify strategies and liaise between construction industry R&I and the European Commission [1,2].

Participation in such fora generated new possibilities for collaboration and broke the ground for lobbying the European Commission to include construction industry priorities in calls for research and development projects. Briefly, the decade ushered in countless new R&I opportunities in the construction industry, although Spanish participation in European initiatives was not overly intense.

3. The first decade of the twenty-first century

The significant advances in R&I witnessed in this decade in both Europe and Spain were not lost on the construction industry.

Europe-wide, so-called integrated R&I projects were launched which, while similar to those prevailing in the preceding period, envisaged consortia with more members (20–30) and much larger budgets [2]. Such projects included initiatives in modular buildings and new approaches to city design with some of their services positioned underground, new developments in soil surveying and more efficient underground construction.

Significant change also took place in Spain with the furtherance of so-called singular strategic projects (Spanish initials, PSE) and CENIT[5] projects involving large consortia and budgets. The construction industry initiatives implemented under the former were reminiscent of the European integrated projects undertaken in similar domains. The latter conducted studies on sustainable construction and the construction and operation of motorways, among others.

A European Commission analysis of the experience acquired with R&I projects found their impact on European industry competitiveness to be insufficient. In 2004 the Commission consequently launched its Technological Platform initiative. Such Platforms can be used to define a given industry's vision of the future and the concomitant R&I priorities to be addressed by 2020–2030, as jointly established by companies, research institutes, universities, end users and other stakeholders. That exercise gave rise to so-called Strategic Research Agendas.

The construction industry responded enthusiastically and in the summer of 2004 launched the European Construction Technology Platform, ECTP (www.ectp.org), headed by a group of companies that formed part of the aforementioned ENCORD group. Spain played an active role through its construction majors and both research and technology institutes. ECTP defined its 2020 Vision and a number of versions of its Strategic Research Agenda. Some of its R&I priorities were included by the European Commission in calls announced by the Directorates General of Research and Innovation and Transport.

ECTP launched the E2B Energy Efficient Buildings initiative to address high energy consumption in buildings. The initiative was subsequently adopted by the European Commission as one of the main pillars, along with the green car and the factory of the future, of its 2008 Recovery Plan [3]. In addition, the Ad hoc Industrial Group created by the Commission and industry representatives defined a series of roadmaps that established many of the area priorities listed under the FP7 and H2020 programmes. ECTP also put forward the ReFINE (Research for Future Infrastructures in Europe) initiative to drive R&I in transport infrastructures, in light of the lack of Framework Programme calls specifically addressing these issues [2].

The 'local' nature of the construction market persuaded the industry that the European Construction Platform initiative should be replicated in member countries. National platforms were consequently established in a number of European States. In light of the prominence of Spanish organisations in ECTP, the Spanish Construction Technology Platform, PTEC (www.plataformaptec.es), was one of the first to be launched after the summer of 2004. Ever since, it has played a key role in furthering construction industry innovation [4].

In the early years, like the European scale ECTP, the Spanish initiative defined its Vision document and the Strategic Research Agenda. It was within PTEC where the scope of the major singular strategic and CENIT projects envisaged in those years was defined and where the large consortia required to undertake them were formed.

A significant initiative undertaken in that first decade by the European Commission identified so-called lead markets, acknowledging sustainable construction as one. The initiative aimed to identify the obstacles to innovation in the markets earmarked and spur policies between the European Union and Member States that would favour the application of the new technologies available in such markets. The objective was to

[1] Spain's National Research Council.
[2] Eduardo Torroja Institute for Construction Science.
[3] National Centre for Metallurgical Research.
[4] Technical Research Institute.
[5] Consorcios Estratégicos Nacionales en Investigación Técnica [strategic national consortia for technology research].

generate strategies that would help remove the hindrances to innovation.

4. The second decade of the twenty-first century

The present period has been heavily impacted by the financial crisis begun in the latter years of its predecessor, which has compromised the continuation of many of the R&I initiatives undertaken previously.

4.1. Activities in Spain

The construction industry has sponsored a number of R&I projects, most prominently the ones submitted to the CIEN[6] programme on subjects such as 3D printing in buildings, maintenance and repair of road and motorway pavement and improvements in tunnelling procedures.

The Spanish Construction Technology Platform has played an important role in furthering R&I in construction. In early 2013, it defined its new strategy based on three main pillars:

- Internationalising R&I among PTEC members
- Furthering innovation
- Enhancing the construction industry's image through R&I

Five PTEC working groups have been active in this period: two are strategic (R&I internationalisation and furtherance of innovation) and three theme-based (city of the future, transport infrastructures and construction processes). In addition, the platform has organised:

- Ten workshops to pool PTEC member experience in several areas and initiatives (protection for innovation; technical approvals for innovative solutions and their acceptance by third parties, including insurers; SMEs and construction innovation; the digital transformation: construction 4.0)
- Fourteen open fora that aim to further contact between PTEC members and other organisations in Spain to fuel construction innovation initiatives. Meetings on subjects such as innovation in the urban environment, transport infrastructures and construction processes were held in Barcelona, Bilbao, Madrid, Málaga, Santander, Seville, Valencia, Valladolid and Zaragoza. By way of example, one on innovation in construction processes was held at Seville in November 2016 [5] and another on innovation in transport infrastructures at Madrid in November 2017 [6].

In Spain in this period other efforts have focused primarily on furthering innovation in construction, an area generously addressed in the Spanish platform's [7] working programme, including items such as:

- Public procurement and innovation
- Protection of innovation
- Innovation culture in the private and public sectors
- Technical approvals for innovative solutions and their acceptance by third parties, including insurers

In connection with the first item, the construction industry deems that innovation should be client-driven, for the client is often a national, regional or municipal government. Here the recent transposition of European directives on public procurement should play an important role in according innovation more weight in such contracts. Although the Public Procurement of Innovation PPI [8], launched towards the end of the preceding decade, has failed to make a sufficient impact on the construction industry, initiatives using this tool will hopefully be possible with the waning of the crisis. Innovation in public procurement was amply debated at the Eighth PTEC Forum held at IETcc headquarters, Madrid, in 2008 [9], with authorities representing the Ministries of the Economy and Competitiveness, Finance and Public Works, as well as the regional governments of Valencia and Extremadura.

With respect to the second item, PTEC has sponsored initiatives in conjunction with the Spanish Patent and Trademarks Office (Spanish initials OEPM), a PTEC collaborating member. Progress in this area has been hindered, however, by the existing provisions on protection for technological developments and the certain provisions of public tenders that in practice rule out any mention of patented solutions in tenderers' quotes.

The want of innovation culture in companies and clients is an issue to be addressed in the future, although PTEC has organised a few events on the subject. All the stakeholders in construction must be lured out of their comfort zone and encouraged to accept innovation whenever the risk lies within reasonable limits.

One of the main obstacles encountered in this regard is related to technical approvals for innovative solutions acceptable to third parties, including insurers. This is the core subject of one of the PTEC working groups [7], which has drafted a paper identifying the shortcomings in the ad hoc assessment of the many innovations introduced on site and in engineering design.

Lastly, large corporations and construction holding companies have shown an interest in hosting startups' initiatives as a way to expedite corporate change and develop new construction materials, components and processes.

4.2. International cooperation

The European Construction Technology Platform, ECTP (www.ectp.org), embarked on a new stage in this period, merging with the Energy Efficient Buildings initiative to constitute a single association structured around five commissions:

- Active ageing and design
- Energy efficient buildings
- Heritage and regeneration
- Infrastructures and mobility
- Materials and sustainability

[6] Programme that finances large R&D projects involving the effective collaboration of two or more business groups.

PTEC engages in ongoing communication with ECTP and networks with national construction platforms in Austria, Belgium, Cyprus, Denmark, France, Germany, Greece, Hungary, Italy, Lithuania, Norway, Poland, Portugal, Slovenia, Spain, Sweden and UK. This network, coordinated by PTEC, aims to further collaboration among the countries involved and ECTP in innovating the European construction industry.

In 2014–2017 PTEC also participated in REFINET (http://infrastructure.ectp.org/csa-refinet), a coordination support action (CSA) that fosters R&I in transport infrastructures.

In this decade, the European Commission has sponsored initiatives for collaboration between European countries and the United States. The most prominent include:

- EraNet Plus Infravation, which financed nine R&I projects for roads with European and US partners under a European Conference of Directors General of Roads (CEDR) (http://www.cedr.eu/) initiative
- Twinning projects, which identifies European projects for which similar projects are underway in the US, leading to contacts and meetings to further collaboration among the consortia involved
- Symposia in which European and US organisations participate to discuss R&I-related subjects, including analysis of the application of research results to transport infrastructures on the two continents [10].

5. Final remarks

The vast changes taking place today will affect the construction industry and require new strategies to drive innovation in areas such as:

- The environment and compliance with circular economy criteria and demands to intensify recycling in buildings and infrastructures, both during and after construction
- Global warming, a reality that affects both transport infrastructures (flood-prone and coastal areas) and buildings and their energy efficiency
- The digital transformation to so-called Construction 4.0 with revolutionary change in the construction industry that will call for innovative policies
- The integration of initiatives, such as those originating in startups, in large companies' strategies
- The Public Procurement of Innovation PPI, an excellent tool to demand innovation of the government buyer, but scantly used in the construction industry. Industry reactivation (presently visible in building but still awaited in civil construction), in conjunction with the transposition of European directive-mediated legislation on public procurement, is expected to drive innovation in construction.
- The launch of a new European R&I Framework Programme, 2020–2027 (FP), that will prompt R&I collaboration, providing the construction industry is able to persuade Community authorities and Member States to prioritise R&I as it deserves in light of the industry's weight in the European production sector. All the foregoing is to be supplemented by national initiatives under national scientific and technical research and innovation plans.

Lastly, innovation and entrepreneurial culture must be furthered in university training and policies should be implemented to favour understanding and collaboration between companies and research institutions and universities. European and Spanish construction, road, railway and energy efficiency technology platforms should continue to play an instrumental role in driving collaboration in R&I.

Acknowledgements

The author's thanks go to the organisations with which he has cooperated in furthering R&I in the construction industry, in particular Dragados and Geocisa (ACS Group), construction companies, and the Spanish Construction Technology Platform, PTEC.

References

[1] J. Rodríguez. La I+D+i en el sector de la construcción. Revista de la Ingeniería Española n°18, Tecniberia, Nov-Dic. 2008, pp. 51–55.
[2] J. Rodríguez, M. Segarra, E. Martin. La I+D+i y la internacionalización. Congreso de ingeniería civil, Valencia, noviembre 2011.
[3] A European Economic Recovery Plan. European Commission. Communication from the EC to the European Council. Brussels, 26.11.2008.
[4] J. Rodríguez, La Plataforma Tecnológica de la construcción como foro para la colaboración entre empresas y organismos de investigación. VI Congreso de ACHE, Madrid, junio 2014.
[5] PTEC. La innovación en los procesos de construcción. Informe 12° Foro, Sevilla, noviembre 2016.www.plataformaptec.es<http://www.plataformaptec.es.
[6] PTEC. La innovación en las infraestructuras del transporte. Informe 14° Foro, Madrid, noviembre 2017. www.plataformaptec.es<http://www.plataformaptec.es.
[7] J. Rodríguez, M. Amérigo, C. Thomas. El fomento de la innovación en el sector de la construcción. VII Congreso de ACHE, La Coruña, Junio 2017.
[8] Fundación PTEC, Compra pública de tecnología innovadora. Algunos ejemplos del sector de construcción. Madrid, 2012.
[9] PTEC. La innovación en la contratación pública en el sector de construcción, Informe 8° Foro, Madrid, 2015. www.plataformaptec.es<http://www.plataformaptec.es.
[10] TRB Conference Proceedings 51: Transportation Research Implementation: Application of Research Outcomes. Second EU-U.S. Transportation Research Symposium, Paris, France, April 10–11, 2014.

Available online at
ScienceDirect
www.sciencedirect.com
Hormigón y Acero 2019; 69(S1):75–80
www.e-ache.com
www.elsevierciencia.com/hya

Model for the compressive stress–strain relationship of steel fiber-reinforced concrete for non-linear structural analysis

Ley tensión-deformación en compresión para el análisis no lineal de estructuras de hormigón reforzado con fibras de acero

Gonzalo Ruiz [a,*], Ángel de la Rosa [a], Sébastien Wolf [b], Elisa Poveda [a]

[a] *ETSI Caminos, C. y P., Universidad de Castilla-La Mancha, Avda. Camilo José Cela s/n, 13071 Ciudad Real, Spain*
[b] *ArcelorMittal Fibres, Route de Finsterthal, L-7769 Bissen, Luxembourg*

Received 17 October 2018; accepted 22 October 2018
Available online 3 December 2018

Abstract

A model for non-linear calculations of steel fiber-reinforced concrete (SFRC) elements in compression is proposed and described technologically. The same curve produced by Eurocode 2 (EC2) is used until compressive strength, although non-dimensional variables refer to fiber concrete parameters. Beyond the peak, we use a parabola that is derived so that the average energy consumption of the material equals this same mean energy obtained from a database comprised of 197 tests. Estimates for the compressive strength of SFRC and the corresponding critical strain are also provided by correlation with the database using the surface response methodology. The total energy consumption of SFRC in compression is approximately four times higher on average than the corresponding energy of the base plain concrete, which is included in the model. Therefore, it can considerably improve the modeling of ductility in SFRC structures.

Keywords: Steel fiber-reinforced concrete; Compressive stress-strain relationship; Non-linear structural analysis; Response-surface methodology

Resumen

Se propone y se describe, en formato tecnológico, un modelo para el cálculo no-lineal de elementos de hormigón reforzado con fibras de acero (HRFA) en compresión. Hasta el pico de carga, se usa la curva dada por el Eurocódigo 2 (EC2), aunque las variables adimensionales se refieren a los parámetros del hormigón reforzado con fibras. Después del pico, usamos una parábola que se calcula de modo que la energía consumida por el material sea igual al valor de esa misma energía dada por una base de datos compuesta por 197 ensayos. También se proporcionan estimaciones de la resistencia a compresión del HRFA y de la deformación crítica correspondiente, las cuales se obtienen por correlaciones con la base de datos usando la metodología de las superficies de respuesta. La energía consumida por el HRFA en compresión es, como media, unas cuatro veces mayor que la que tendría su matriz sin reforzar, lo cual es reproducido por el modelo. Así, éste puede mejorar considerablemente el modelado de la ductilidad en estructuras de HRFA.

Palabras clave: Hormigón reforzado con fibras de acero; Ley tensión-deformación en compresión; Análisis no-lineal; Metodología de las superficies de respuesta

1. Introduction

This technical note describes a model for the compressive stress–strain (σ–ε) behavior of steel fiber-reinforced concrete. The model is based on functions obtained from correlations with

* Corresponding author.
E-mail address: Gonzalo.Ruiz@uclm.es (G. Ruiz).

https://doi.org/10.1016/j.hya.2018.10.001

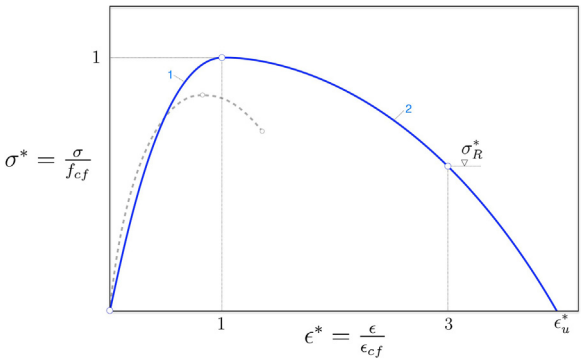

Figure 1. Schematic representation of the stress-strain relationship in SFRC for structural analysis (solid curve), compared with that of the corresponding base concrete (broken line curve).

an extensive database comprised of 197 well-documented SFRC compressive tests [1–20].

The following section describes the σ–ε model. Subsequently, we justify the assumptions made to formulate the model and provide a brief description of the database that supports a few of the expressions of the model, together with a short explanation of the response-surface methodology and the process followed in order to obtain the responses.

2. σ–ε relationship for non-linear structural analysis of SFRC

The relationship between σ and ε, shown in Fig. 1, may be used to model the response of SFRC to short term uniaxial compression. It has two distinct curves. The first runs from the origin of the axes to the maximum stress (curve 1 in Fig. 1) and is described by the following equation:

$$\sigma^* = \frac{\alpha\varepsilon^* - \varepsilon^{*2}}{1 + (\alpha - 2)\varepsilon^*} \tag{1}$$

where:

$\sigma^* = \frac{\sigma}{f_{cf}}$	Non-dimensional stress
f_{cf}	Compressive strength of SFRC
$\alpha = 1.05\varepsilon_{cf}\frac{E_f}{f_{cf}}$	Non-dimensional coefficient
ε_{cf}	Critical strain, i.e. strain that corresponds to f_{cf}
E_f	Elastic modulus of SFRC
$\varepsilon^* = \frac{\varepsilon}{\varepsilon_{cf}}$	Non-dimensional strain

The compressive strength and corresponding strain plus the elastic modulus of SFRC can be easily obtained by testing. These values can also be estimated by using the following equations:

$$f_{cf} = f_{c0}\left(1 + 4.174\ell_f^*\phi_f\right) \tag{2}$$

$$\varepsilon_{cf} = \varepsilon_{c0}\left[1 + 0.4823\ \lambda\ \left(\phi_f - 0.002606\ell_f^*\right)\right] \tag{3}$$

$$E_f = E_0 \tag{4}$$

where:

$\ell_f^* = \frac{\ell_f}{\ell_0}$	non-dimensional fiber length
$\ell_0 = 30$ mm	coefficient to maintain non-dimensionality
ϕ_f	volumetric fiber ratio
f_{c0}	compressive strength of the base concrete in MPa, determined according to Table 5.1 of EC2 [21] (see Fig. 2)
$\varepsilon_0 = 0.0007\left(\frac{f_{c0}}{f_0}\right)^{0.31}$	critical strain of the base concrete, i.e. strain at maximum stress
$f_0 = 1$ MPa	coefficient to maintain non-dimensionality
λ	fiber aspect ratio
E_0	elastic modulus of the base concrete

The second curve (labeled as 2 in Fig. 1) is a softening branch that runs from peak stress to zero. The following parabola defines the curve:

$$\sigma^* = 1 - \frac{1}{4}\left(1 - \sigma_R^*\right)\left(\varepsilon^* - 1\right)^2 \tag{5}$$

where σ_R^* is the following function of the parameters that characterize the fiber:

$$\sigma_R^* = 0.8279 + 0.3888\,\ell_f^*\,\left(35.03\,\phi_f - 1\right)\ <\ 1 \tag{6}$$

Actually, σ_R^* is the non-dimensional stress corresponding to $\varepsilon^* = 3$, as represented in Fig. 1, which implies that $\sigma_R^* < 1$ as stated in Eq. (6). This second stretch intercepts the x-axis at:

$$\varepsilon_u^* = 1 + \frac{2}{\sqrt{1 - \sigma_R^*}} \tag{7}$$

Note that Eqs. (1) and (5) and related parameters consider that stresses and strains are positive in compression. Likewise, the softening part of the curve, Eqs. (5)–(7), is only valid for SFRC with hook-ended fibers.

3. Justification of the model

The model described above depends basically on two points. The first is the peak of the stress–strain curve, that is, the point which represents the strength of the SFRC, f_{cf}, and its corresponding strain, ε_{cf} (critical strain). The second is the stress for a strain three times the critical strain, i.e. $\sigma_R - 3\varepsilon_{cf}$. We adopt a non-dimensional representation where stresses are divided by f_{cf} and strains by ε_{cf}. Therefore, these points are just (1, 1) and (σ_R^*, 3) in the non-dimensional curve, $\sigma^* - \varepsilon^*$.

The first part of the curve from the origin to the peak stress is modeled by using the same σ–ε curve that is already used in the EC2 for plain concrete. It should be noted though that the new curve refers to the strength and critical strain of the SFRC, rather than to those of the base concrete. The elastic modulus of the material, E_f, determines the slope at the origin, which is α in the non-dimensional curve. As stated above, f_{cf}, ε_{cf}, and E_f are easy to obtain by testing. In the case that an estimate of these values is needed and testing cannot be performed, the model offers Eqs. (2) and (3) in order to obtain f_{cf} and ε_{cf} based on the parameters characterizing the type of fiber (the fiber length, ℓ_f, and the fiber aspect ratio, λ) and the fiber content (ϕ_f). These functions were obtained by using the response-surface methodology on a database comprised of 197 compressive tests on SFRC

		Strength classes for concrete															Analytical expressions
		C12	C16	C20	C25	C30	C35	C40	C45	C50	C55	C60	C70	C80	C90	C100	
f_{ck}	MPa	12	16	20	25	30	35	40	45	50	55	60	70	80	90	100	
f_{cm}	MPa	20	24	28	33	38	43	48	53	58	63	68	78	88	98	108	$f_{cm} = f_{ck} + 8MPa$
f_{ctm}	MPa	1,6	1,9	2,2	2,6	2,9	3,2	3,5	3,8	4,1	4,2	4,3	4,5	4,7	4,9	5,1	$f_{ctm} = 0.30 \cdot f_{ck}^{2/3}$ (Class ≤ C50) $f_{ctm} = 1.10 \cdot f_{ck}^{1/3}$ (Class > C50)
$f_{ctk;0,05}$	MPa	1,1	1,3	1,5	1,8	2,0	2,2	2,5	2,7	2,9	3,0	3,1	3,2	3,4	3,5	3,7	$f_{ctk;0,05} = 0,7\ f_{ctm}$ (5%-fractile)
$f_{ctk;0,95}$	MPa	2,0	2,5	2,9	3,3	3,8	4,2	4,6	4,9	5,3	5,5	5,7	6,0	6,3	6,6	6,8	$f_{ctk;0,95} = 1,3\ f_{ctm}$ (95%-fractile)

Figure 2. Strength and mechanical characteristics of concrete according to Table 5.1 of the Eurocode 2 [21] (f_{c0} in the paper corresponds to f_{cm} in Table 5.1).

samples. The derivation process is explained in the following section. There is no equation for the elastic modulus of the SFRC because the correlation with the database indicates that the fiber parameters are not sufficiently significant in order to determine the $E_f\ /\ E_0$ ratio.

The second part of the curve is an inverted vertical-axis parabola the vertex of which is point (1, 1) and that passes through point (σ_R^*, 3). This point was chosen as a reference because all the tests in the database with a σ–ε curve at least reached it. In other words, the shortest σ–ε tail in the database reached the abscissa $3\varepsilon_{cf}$. The formula for obtaining σ_R^* (Eq. (6)) is derived as follows. The area below the σ–ε curves between the peak and $3\varepsilon_{cf}$ is correlated with the same area of the model expressed as a function of σ_R^*. The correlation process to obtain σ_R^* is similar to those for $f_{cf}\ /\ f_{c0}$ and $\varepsilon_{cf}\ /\ \varepsilon_{c0}$, and is explained in the following section. The last valid point of the model is ε_u^*, which is simply derived as the intercept of the parabola with the x-axis. Note that modeling the SFRC softening through this parabola errs on the side of caution, since most of the softening branches in the database are actually longer and consume more energy than the proposed curve.

It should be noted that very few specimens in the database showed hardening (only three; SFRCs in the database do not exceed a fiber content of 3% in volume). They were not considered in the correlation for calculating σ_R^* because the parabola should not increase (that is the reason we impose $\sigma_R^* < 1$). In the case that we seek to account for hardening in compression there could be recourse to the limit case of a horizontal straight line ($\sigma_R^* = 1$) and a restricted value of ε_u.

In regard to the total energy consumption of SFRC in compression, the proposed model reflects that it is several times higher than the corresponding energy of the base plain concrete, as suggested in Fig. 1 (the area below the dimensional curve represents the energy consumption per unit volume). In fact, the average energy consumption of the SFRC during the ascending/softening branch in the database is 1.5/2.8 times the energy of the corresponding base concrete in the ascending branch. Thus, the total energy consumed in SFRC is around four times larger on average than that of the corresponding base concrete (and this only considers the energy up to $3\varepsilon_{cf}$). Consequently, the use of the proposed σ–ε curve can considerably improve the modeling of ductility in SFRC structures.

4. Database and response-surface methodology

The database generated for this study contains 197 compressive tests on SFRC 150 × 300 mm^2 cylinders [1–20]. All have information concerning the base concrete. Likewise, all concretes were reinforced exclusively with steel hook-ended fibers with only one bend. 80 of the tests reported the complete σ–ε curve. Some of the relevant parameters of the database fall within the following ranges:

- Compressive strength of SFRC (f_{cf}): 29.4–93.5 MPa
- Maximum aggregate size (d_m): 10–25 mm
- Volumetric fiber ratio (ϕ_f): 0.24–3.00%
- Fiber length (ℓ_f): 10–80 mm
- Fiber diameter (d_f): 0.2–1.2 mm
- Aspect ratio ($\lambda = \ell_f\ /\ d_f$): 20–107

The time at which the compressive tests were performed was 28 days, with a few exceptions.

The response-surface methodology [22] is a correlation procedure to determine a continuous function f for n of the parameters that are thought to be significant for its response:

$$y = f(x_1,\ x_2,\ \ldots, x_n) + \xi \tag{8}$$

where ξ is the error in the response as compared to the database. In general, f is unknown and thus, it is necessary to experiment with conventional polynomial functions such as:

$$\sum_{i=1}^{n} \beta_i x_i + \sum_{i=1}^{n} \beta_{ii} x_i^2 + \sum_{i=1}^{n-1} \sum_{j>i}^{n} \beta_{ij} x_i x_j \tag{9}$$

where β_i are the coefficients for the linear terms, β_{ii} the coefficients for the quadratic terms and β_{ij} with $j>i$ the coefficients for the combination of variables.

In this particular application, we look for the response of the relative values of the elastic modulus E_f, the compressive strength f_{cf} and the critical strain ε_{cf} compared with the corresponding values of the base concrete, plus the response of σ_R (σ for $3\varepsilon_{cf}$) related to the compressive strength of the SFRC. We want to express these relative values as functions of basic parameters of the fiber reinforcement, namely the fiber length ℓ_f, the fiber aspect ratio λ and the fiber volume fraction ϕ_f. Consequently, the correlation was performed using non-dimensional

	I.T.	ℓ_f^*	λ	ϕ_f	$\ell_f^*\lambda$	$\ell_f^*\phi_f$	$\lambda\phi_f$	ℓ_f^{*2}	λ^2	ϕ_f^2
Linear, combined and quadratic coefficients										
E_f°	1	0.651	**−0.01852**	40.4	−0.00388	0.55	−0.402	−0.116	0.000192	−659
f_{cf}°	1	0.243	−0.00373	−13.50	0.00356	**7.81**	0.129	**−0.1868**	−0.000009	−26
ϵ_{cf}°	1	**0.879**	**−0.02637**	**0.8**	**−0.01678**	**−24.04**	**0.831**	**0.1326**	**0.000377**	628
σ_R^*	0.465	3.55	75.3	−0.0860	−4.8	−0.0511	0.120	0.092	**−2151**	0.001087
Linear and combined coefficients										
E_f°	1	−0.0012	−0.00113	7.92	0.000509	−2.97	−0.025	—	—	—
f_{cf}°	1	**−0.0344**	**0.00123**	−13.59	−0.000518	**8.76**	0.106	—	—	—
ϵ_{cf}°	1	0.345	**−0.00147**	−5.9	**−0.00469**	−10.73	**0.840**	—	—	—
σ_R^*	0.792	**−0.914**	20.5	−0.00583	3.8	**0.01094**	−0.078	—	—	—
Coefficients for significant terms only (second iteration)										
E_f°	1	—	**−0.0001**	—	—	—	—	—	—	—
f_{cf}°	0.98	—	—	—	—	**4.174**	—	—	—	—
ϵ_{cf}°	1.05	—	—	—	**−0.001257**	—	**0.4823**	—	—	—
σ_R^*	0.8279	**−0.3888**	—	—	—	**13.62**	—	—	—	—

(Coefficients in bold type mean that their variables are significant)

Figure 3. Coefficients for functions to fit the database (I.T. refers to an independent term).

data referring to the corresponding values of the base concrete ($E_f^o = E_f/E_0$, $f_{cf}^o = f_{cf}/f_{c0}$ and $\varepsilon_{cf}^o = \varepsilon_{cf}/\varepsilon_{c0}$) or the fiber concrete ($\sigma_R^* = \sigma_R/f_{cf}$). Regarding the fiber parameters, only the length had to be converted in order to be non-dimensional by using $\ell_f^* = \ell_f \ / \ \ell_0$ (note that the choice for ℓ_0 is arbitrary since its actual value only affects the resulting non-dimensional coefficients so that the final product is the same). The most complete correlation in this work includes linear, combined and quadratic terms.

The coefficients obtained for each desired parameter are set forth in Fig. 3. For example, the full response (linear, combined and quadratic) for the compressive strength is:

$$f_{cf}^o = 1 + 0.243\,\ell_f^* - 0.00373\lambda - 13.50\phi_f + 0.00356\,\ell_f^*\lambda + 7.81\,\ell_f^*\phi_f + 0.129\lambda\phi_f - 0.1868\,\ell_f^{*2} - 0.000009\lambda^2 - 26\phi_f^2 \quad (10)$$

where only the terms corresponding to $\ell_f^*\phi_f$ and to ℓ_f^{*2} are actually significant (this is the reason that their coefficients are written in bold type in Fig. 3). Likewise, we also obtained coefficients for the linear plus the combined response, see Fig. 3. Note that this time we determine that ℓ_f^* and λ are significant. In order to derive simpler equations where only significant terms are present, we resort to the correlation again in linear mode and only with terms that had already been found to be significant. The outcome often reveals that some terms were not really significant and, in these cases, we eliminate them and resort to the correlation again. This is how we reach the simplest equation for the parameter under study, in this case, the compressive strength:

$$f_{cf}^o = 1 + 4.174\,\ell_f^*\phi_f \quad (11)$$

Note that we rounded the independent term to 1, since the methodology does not perform any type of asymptotic study but just simple correlation. The procedure to obtain the remaining responses is similar to the one previously described. Fig. 4 plots Eq. (11) superimposed over the values in the database. It is clear that there is a remarkable dispersion, since f_{cf} mostly correlates with the compressive strength of the base concrete

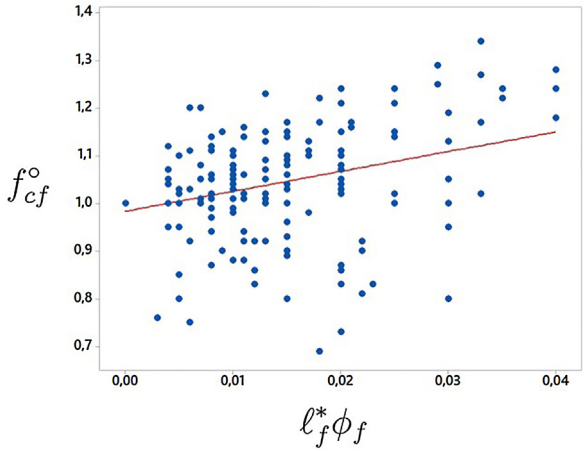

Figure 4. Non-dimensional compressive strength ${f_{cf}}^0 = (f_{cf}/f_{c0})$ as a function of parameter $\ell_f^*\phi_f \quad (= \ell_f\phi_f \ / \ \ell_0)$ compared with the experimental values in the database.

f_{c0}, which is the value chosen to get non-dimensional f_{cf}. This is the reason for which we recommend that f_{cf} and ε_{cf} are actually measured, since Eq. (11) is only a rough approximation of the average behavior of tests in the database. Similarly, Fig. 5 plots the database values for ε_{cf} and σ_R as functions of some of the influential non-dimensional parameters in Eqs. (3) and (6), namely $\lambda\phi_f$ and $\ell_f^*\phi_f$. It also plots the response surfaces that correspond to these equations. Note that the database values for ε_{cf} and σ_R show less scatter than for f_{cf}.

Despite having tried to simplify the equations by increasing the average significance of the terms, all the response levels could be used. The response is more accurate indeed when the more complex equations are considered. On the other hand, as already commented above, we did not find a good correlation for the relative elastic modulus (the significance of λ for E_f^o is very weak, see the Table in Fig. 3). The methodology reveals that fiber content in low dosages does not influence the SFRC compressive response at small strains. We did not propose a type of phase-rule, i.e. such as $E_f = E_0(1-\phi_f) + E_s\phi_f$ because the database does not find ϕ_f significant.

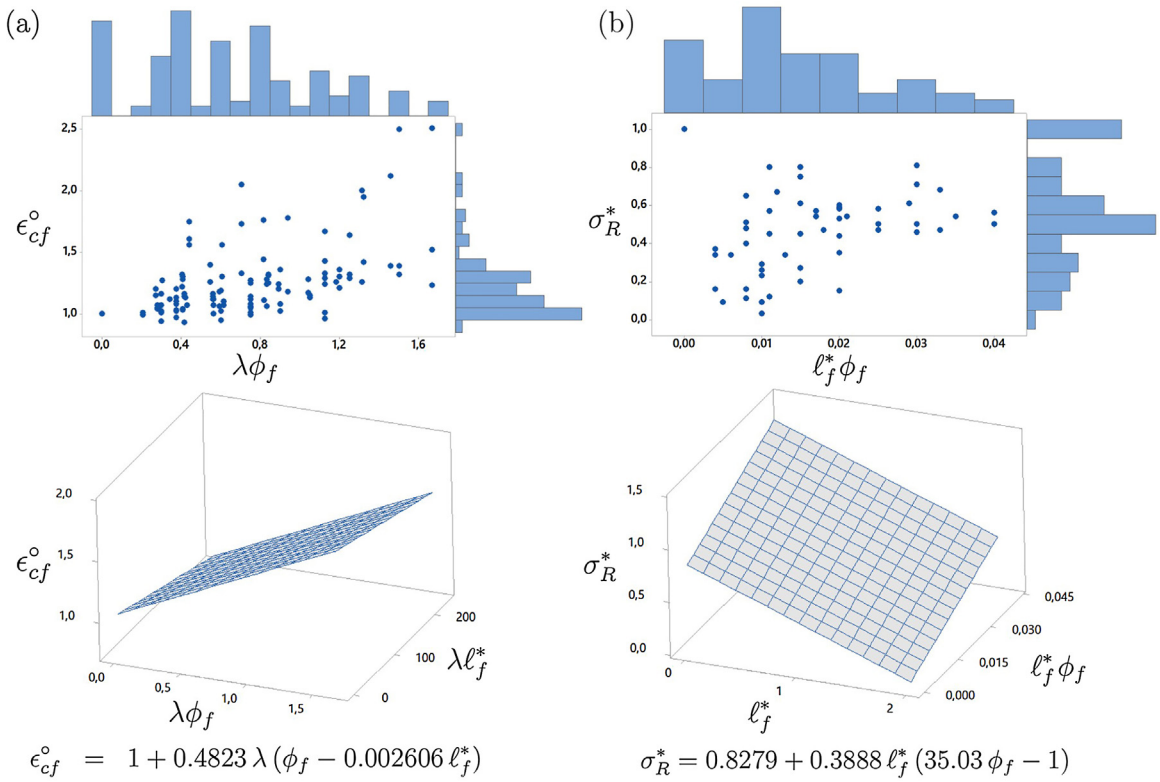

Figure 5. Database values and 3D plots of the selected functions for the non-dimensional (a) critical strain $\varepsilon^0_{cf}(= \varepsilon_{cf} \,/\, \varepsilon_{c0})$; and (b) stress corresponding to $\varepsilon = 3\,\varepsilon_{cf}$, $\sigma^*_R(= \sigma_R \,/\, f_{cf})$.

5. Conclusions

This technical note proposes a σ–ε curve for steel fiber-reinforced concrete (SFRC) in compression, intended for non-linear calculations. The model is described technologically, similarly to that used in structural codes. The model has two distinct stretches. The first describes the σ–ε behavior up to the maximum load, following the same curve proposed by Eurocode 2 [21] for plain concrete, but using non-dimensional variables referring to fiber reinforced concrete.

The second stretch is defined as a vertical parabola the vertex of which corresponds to compressive strength. It is must pass through point $\sigma_R - 3\varepsilon_{cf}$, which in turn is estimated by correlation to an extensive database of actual σ–ε curves. The correlation to get σ_R is made so that the average energy below the σ–ε curve between ε_{cf} and $3\varepsilon_{cf}$ in the database equals that of the parabola for the same stretch. Therefore, this assumption for the second part of the σ–ε curve yields the same mean energy consumption as tests in the database up to $3\varepsilon_{cf}$. Beyond this point we still use the parabola, which is relatively safe since most of the tests in the database exhibit long tails. The technical note also provides estimates for the compressive strength of the steel fiber-reinforced concrete and for the corresponding critical strain. All the formulas are derived by using the response-surface methodology and a database formed by 197 tests on SFRC (only standard cylinders of SFRC with hook-ended fibers with only one bend).

Regarding the total energy consumption of SFRC in compression, the proposed model reflects that it is approximately four times higher on average than the corresponding energy of the base plain concrete (considering only the energy up to 3 ε_{cf}). Therefore, the proposed $\sigma - \varepsilon$ curve can considerably improve the modeling of ductility in SFRC structures.

6. Dedication

This work is dedicated to Dr. Carmen Andrade both for her extensive and deep contribution to research in the field of construction technology and for her leading personal example and friendship.

Acknowledgements

Funding from the *Ministerio de Economía y Competitividad* through project BIA2015-68678-C2-1-R and International Campus of Excellence CYTEMA is gratefully acknowledged. Ángel de la Rosa expresses his gratitude for the fellowship FPI BES-2016-077458.

References

[1] S. Lee, J. Oh, J. Cho, Compressive behavior of fiber-reinforced concrete with end−hooked steel fibers, Materials 8 (4) (2015) 1442–1458.
[2] R. Neves, J. Fernandes de Almeida, Compressive behaviour of steel fibre reinforced concrete, Struct. Concr. 6 (1) (2005) 1–8.

[3] J. Barros, J. Figueiras, Flexural behavior of SFRC: testing and modeling, J. Mater. Civ. Eng. 11 (4) (1999) 331–339.
[4] F. Bencardino, L. Rizzuti, G. Spadea, R. Swamy, Stress−strain behavior of steel-fiber reinforced concrete in compression, J. Mater. Civ. Eng. 20 (2008) 255–263.
[5] F. Bencardino, L. Rizzuti, G. Spadea, Experimental tests vs. theoretical modeling for FRC in compression, FraMCoS (2007) 159–166.
[6] P. Song, S. Hwang, Mechanical properties of high-strength steel-fiber reinforced concrete, Construct. Build. Mater. 18 (9) (2004) 669–673.
[7] K. Marar, Ö. Eren, T. Çelik, Relationship between impact energy and compression toughness energy of high-strength fiber-reinforced concrete, Mater. Lett. 47 (2001) 297–304.
[8] J. Thomas, A. Ramaswamy, Mechanical properties of steel-fiber reinforced concrete, J. Mater. Civ. Eng. 19 (2007) 385–392.
[9] F. Bayramov, C. Tasdemir, M. Tasdemir, Optimisation of steel-fibre reinforced concretes by means of statistical response surface method, Cem. Concr. Comp. 26 (2004) 665–675.
[10] B. Jo, Y. Shon, Y. Kim, The evaluation of elastic modulus for steel-fiber reinforced concrete, Russian J. Nondestruct. Test. 37 (2001) 152–161.
[11] F. Aslani, S. Nejadi, Self-compacting concrete incorporating steel and polypropylene fibers: compressive and tensile strengths, moduli of elasticity and rupture, compressive stress–strain curve, and energy dissipated under compression, Comp. Part B: Eng. 53 (2013) 121–133.
[12] Y. Şahin, F. Köksal, The influences of matrix and steel-fibre tensile strengths on the fracture energy of high-strength concrete, Construct. Build. Mater. 25 (4) (2011) 1801–1806.
[13] P. Cachim, J. Figueiras, P.A. Pereira, Fatigue behavior of fiber reinforced concrete in compression, Cem. Concr. Comp. 24 (2) (2002) 211–217.
[14] B. Barragán, R. Gettu, M. Martín, R. Zerbino, Uniaxial tension test for steel-fibre reinforced concrete – a parametric study, Cem. Concr. Comp. 25 (7) (2003) 767–777.
[15] A. Medeiros, X. Zhang, G. Ruiz, R. Yu, M. de Souza Lima, Effect of the loading frequency on the compressive fatigue behavior of plain and fiber reinforced concrete, Int. J. Fat. 70 (2015) 342–350.
[16] H. Dhonde, Y. Mo, T. Thomas, C. Hsu, J. Vogel, Fresh and hardened properties of self-consolidating fiber-reinforced concrete, ACI Mater. J. 104 (5) (2007) 491–500.
[17] K. Marar, Ö. Eren, I. Yitmena, Compression specific toughness of normal strength steel-fiber reinforced concrete (NSSFRC) and high-strength steel-fiber reinforced concrete (HSSFRC), Mater. Res. 14 (2) (2011) 239–247.
[18] F. Wafa, S. Ashour, Mechanical properties high-strength fiber reinforced concrete, ACI Mater. J. 89 (5) (1992) 449–455.
[19] M. Tabatabaeian, A. Khaloo, A. Joshaghani, E. Hajibandeh, Experimental investigation on effects of hybrid fibers on rheological, mechanical, and durability properties of high-strength SCC, Construct. Build. Mater. 147 (2017) 497–509.
[20] F. Köksal, A. Ilki, M. Tasdemir, Optimum mix design of steel-fibre reinforced concrete plates, Arabian J. Sci. Eng. 38 (11) (2013) 2971–2983.
[21] Eurocode 2, Design of Concrete Structures. European Standards, European Committee for Standardization, EN 1992-2:2005/AC, 2008.
[22] Minitab 18 Statistical Software, www.minitab.com, 2018.